UNIVERSITY OF CALIFORNIA

Los Angeles

Probing the Surroundings of Supermassive Black Holes in Active Galaxies

A dissertation submitted in partial satisfaction

of the requirements for the degree

Doctor of Philosophy in Astronomy and Astrophysics

by

Lizvette Villafaña

2024

ABSTRACT OF THE DISSERTATION

Probing the Surroundings of Supermassive Black Holes in Active Galaxies

by

Lizvette Villafaña
Doctor of Philosophy in Astronomy and Astrophysics
University of California, Los Angeles, 2024
Professor Tommaso L. Treu, Chair

It is believed that supermassive black holes ($M_{BH} \sim 10^6 M_\odot - 10^9 M_\odot$) in the center of galaxies are a vital component of galaxy evolution. This idea is driven by two observations: (i) black hole (BH) masses are tightly correlated to host galaxy properties in local quiescent galaxies, and (ii) BH accretion and star formation histories track one another closely. These two observations suggest that the growth of accreting BHs is intimately connected to that of their host galaxies. However, the origin and physical mechanism remains unknown and is an active area of astrophysical research.

The goal of this dissertation is twofold: (i) characterize the structure and kinematics of the broad emission line region (BLR) to better understand the central regions of accreting BHs and (ii) improve the way BH mass measurements are calibrated across cosmic time. While both goals aim to provide insight into the role BHs play in galaxy evolution, the latter is most relevant for studies that probe the origin of the BH scaling relations via characterization across redshift.

In this dissertation, I model the Hβ BLR of nine Active Galactic Nuclei (AGN) observed

during the Lick AGN Monitoring Project (LAMP) 2016 reverberation mapping campaign and investigate whether there are any luminosity-dependent trends in the structure and kinematics of the Hβ BLR. Then, I combine the LAMP 2016 modeling results with previous LAMP reverberation mapping campaigns and search for a way to improve how BH masses are calibrated across cosmic time. Finally, I expand on the initial development and testing of CARAMEL-GAS, which aims to model the gas density field of the BLR to model multiple emission lines simultaneously, e.g., Hα and Hβ, and learn about the surroundings of active BHs. However, further testing and development of CARAMEL-GAS beyond the work presented in this thesis is required before achieving this goal. Overall, future reverberation mapping campaigns with sufficient data quality and variability are needed to confirm the results presented in this thesis.

The dissertation of Lizvette Villafaña is approved.

Matthew A. Malkan

Alice E. Shapley

Steven R. Furlanetto

Tommaso L. Treu, Committee Chair

University of California, Los Angeles

2024

To first-generation Latinas pursuing a higher education.

TABLE OF CONTENTS

LIST OF FIGURES

LIST OF TABLES

ACKNOWLEDGMENTS

First and foremost, this thesis dissertation was only possible with my advisor, Tommaso Treu. I thank him for giving me an opportunity in Astronomy and academia and setting me up for success. I often felt like Tommaso thought I was better than I was, but I guess that is the best quality I could ever ask for in a mentor — genuinely believing in me. I am forever grateful for his unwavering support throughout my graduate career at UCLA, especially in handling my career indecision gracefully.

I acknowledge the immense work done by graduate students before me, Anna Pancoast and Peter Williams, who also made this dissertation possible; I stand on the shoulders of giants. I especially thank Peter for taking the time to train me during my first year.

I thank the mentors I had before my Ph.D. program at the Space Engineering Research Center during my previous graduate program — Becca Rogers, Kyle Clarke, and Rahul Rughani. I had never had a mentor before, and their help and support truly changed the academic game for me.

I thank my parents, Olga and Juan Villafaña. *Apá, usted me motivó a ir a la universidad cuando estaba chica — este trabajo empezó con su sueño, gracias.* To my dad, who motivated me to get a university education when I was younger — my academic endeavors began with his dream. To my mother, who has been the most supportive and kind parent I could have ever asked for — I thank her for all the support she has given me while pursuing a higher education. *Los quiero mucho,* I love you both.

Thank you to my partner, Michael Herndon, for being the Yin to my Yang. Your constant reminders to not take things too seriously and to enjoy the process have been invaluable. I am incredibly grateful to have met you halfway through my Ph.D. journey and for all the unwavering support and love you have provided since day one.

Thank you to the silly, goofy friends I made during my Ph.D. program — Zoe Haggard, Leonardo Clarke, and Devon Williams. Thank you for all the laughs, camping trips, and supporting/joining my dominion obsession. And, Zo, thank you for being the Zo to my Lizzo. I am incredibly grateful to have found a roommate and best friend in you for the second half of my Ph.D. program. Living with you has made the Ph.D. program so much brighter.

To my childhood best friend, Evelyn Silvas, thank you for being by my side despite the miles apart and for the long phone calls when needed. And to my cat, Love, whom I adopted during my first year of the Ph.D. while living alone in a studio during the peak COVID-19 pandemic, I could not imagine writing papers at home without her company.

Lastly, thank you to all my family and friends who are not mentioned in this acknowledgment — it takes a village. *Lo hicimos.* We did it!

VITA

2018 **B.S., Astrophysics**, UCLA, Los Angeles, CA

2018-2020 **Graduate Student Researcher**, University of Southern California Space Engineering Research Center, Los Angeles, CA

2020 **M.S., Aerospace Engineering**, University of Southern California, Los Angeles, CA

2020-2024 **Graduate Student Researcher**, Department of Physics and Astronomy, UCLA, Los Angeles, CA

2022 **M.S., Astronomy and Astrophysics**, UCLA, Los Angeles, CA

2023-2024 **Teaching Assistant**, Department of Physics and Astronomy, UCLA, Los Angeles, CA, Astronomy 180 – Astrophysics Laboratory (Fall 2022), Astronomy 5 – Life in the Universe (Fall 2023 and Winter 2024)

2023-present **Adjunct Astronomy Professor**, Department of Earth Sciences, Santa Monica College, Santa Monica, CA, Astronomy 1 – Stellar Astronomy (Spring 2023, Fall 2023, and Spring 2024), Astronomy 2 – Planetary Astronomy (Fall 2023)

PUBLICATIONS

Empirical models of the Hβ broad emission line gas density field

Villafaña, L., Treu, T., Colleyn, L., et al. 2024, ApJ, 966, 106

What Does the Geometry of the Hβ BLR Depend On?

Villafaña, L., Williams, P.R., Treu, T. et al. 2023, ApJ, 948, 95

The Lick AGN Monitoring Project 2016: Dynamical Modeling of Velocity-Resolved Hβ Lags in Luminous Seyfert Galaxies

Villafaña, L., Williams, P.R., Treu, T. et al. 2022, ApJ, 930, 52

CHAPTER 1

Introduction

Astronomers first proposed the notion of supermassive black holes ($M_{BH} \sim 10^6 - 10^9 M_\odot$) as early as the 1960s to explain the luminous centers of quasars and other active galactic nuclei (AGN). However, the spatial resolution required to resolve the gravitational sphere of influence of the central black hole ($r \equiv GM_{BH}/\sigma^2 \sim 1 - 100$ pc) corresponds to an angular resolution of 0.1" − 1" for nearby galaxies within distances of 1 − 20 Mpc (Kormendy & Ho, 2013a). For this reason, it was not until the mid-late 1980s that dynamical evidence for supermassive black holes first became available (Kormendy & Ho, 2013a, and reference therein). Soon after the launch of the Hubble Space Telescope, its increased spectral angular resolution enabled the discovery of the empirical relations between black hole (BH) mass and host galaxy spheroid properties (often referred to as the local BH scaling relations). Studies of the empirical BH scaling relations first received considerable attention after the discovery of the M-sigma ($M_{BH}-\sigma_*$) relation by both Ferrarese & Merritt (2000a) and Gebhardt et al. (2000a). After accounting for measurement errors, both teams reported a tight correlation between BH mass and stellar velocity dispersion consistent with zero intrinsic scatter. Although the intrinsic scatter remains controversial, most studies agree the scatter is not larger than 0.3 dex (Hirschmann et al., 2010).

The discovery of the $M_{BH}-\sigma_*$ relation (see Figure 1.1 below) for local quiescent galaxies was astonishing in the field of extragalactic astronomy because of the different scales involved. While BH accretion occurs on μpc scales, the BH gravitational sphere of influence occurs on

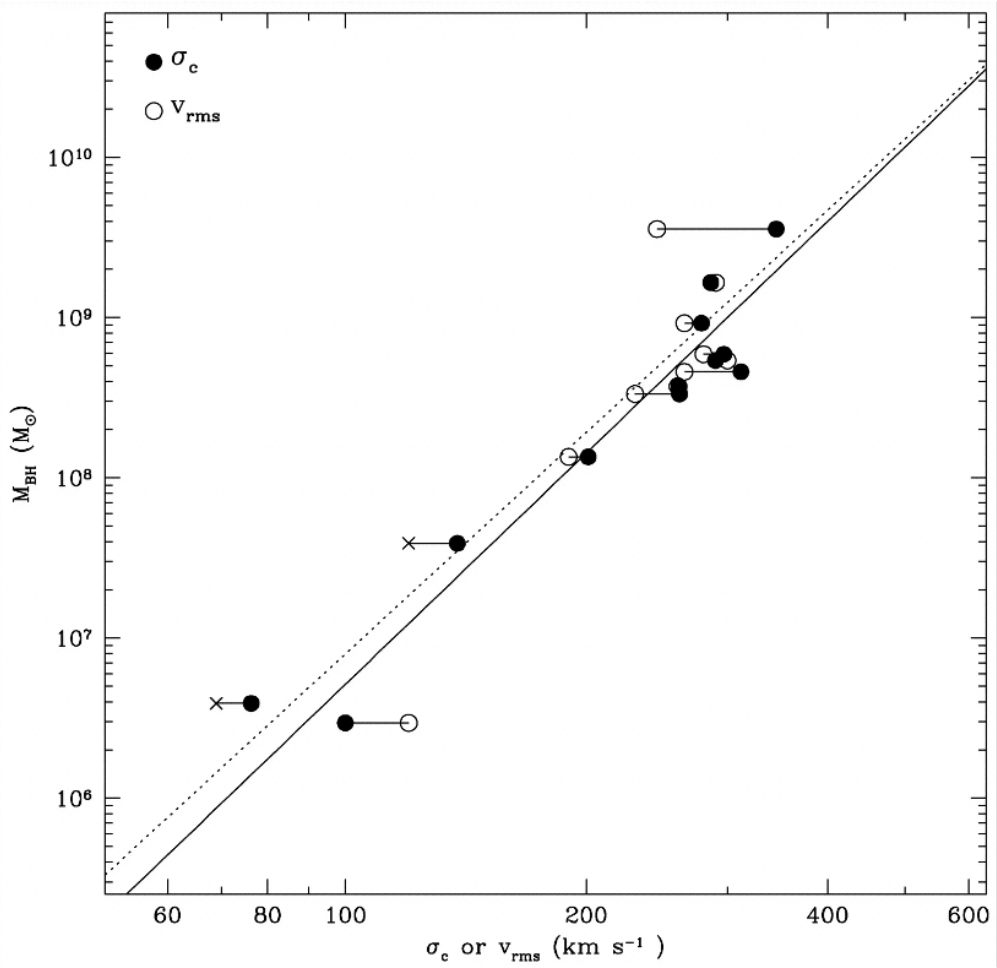

Figure 1.1 The tight correlation between black hole (BH) mass and stellar velocity dispersion reported by Ferrarese & Merritt (2000a) and Gebhardt et al. (2000a) is often interpreted to suggest a coevolution between BHs and their host galaxy. This figure corresponds to the results reported by Ferrarese & Merritt (2000a).

pc scales, and the bulge/spheroid properties occur on kpc scales (Bennert et al., 2010). Tight correlations between BH mass and other host galaxy properties, such as host galaxy stellar luminosity ($M_{BH}-L_*$) and stellar mass ($M_{BH}-M_*$), were also observed more or less at the same time as the discovery of the $M_{BH}-\sigma_*$ relation (Marconi & Hunt, 2003). Together, these relations form the BH scaling relations.

Given that the BH scaling relations were found for a random set of galaxies, the discovery implied: (i) BHs must be ubiquitous in the center of galaxies, and (ii) the evolution of the

BH must be coupled with that of the galactic bulge by some physical mechanism; the idea of the "BH-host galaxy connection/coevolution" was born (for a review, see Kormendy & Ho, 2013b, and references therein).

In addition to the local BH scaling relations, similarities between the history of BH accretion (i.e., BH mass growth) and star formation (i.e., galaxy stellar mass growth) are often cited as evidence for the BH-galaxy coevolution picture. Both star formation and BH accretion histories track each other closely (see Figure 1.2 below), peaking around $z \sim 1-2$ and then declining rapidly (e.g., Boyle & Terlevich, 1998; Madau & Dickinson, 2014; Aird et al., 2015). Combined with the BH scaling relations, these observations suggest that the growth of accreting BHs is intimately connected to that of their host galaxies. However, the origin and physical mechanism behind the apparent BH-host galaxy connection remains unknown and is an active area of astrophysical research.

One proposed mechanism, AGN feedback (Silk & Rees, 1998), has gained a considerable amount of attention for its ability to simultaneously (i) explain the local BH scaling relations and (ii) solve two significant issues in the dark-energy dominated cold dark matter (ΛCDM) paradigm of galaxy formation. [1] An analogy often given in the literature to explain AGN feedback is that the BH acts like a thermostat in a galaxy; the AGN can heat or strip away gas that would have cooled and condensed into stars, regulating the evolution of its host galaxy and in turn its growth, by "starving itself of its fuel" (Schawinski, 2012). Such feedback would lead to star formation rates (e.g., host galaxy stellar mass) that track BH accretion rates (e.g., BH mass) and thus reproduce the BH scaling relations (Figure 1.1) and growth histories (Figure 1.2) observed.

However, the physical mechanism through which AGN feedback operates remains unclear and has motivated many AGN feedback studies through semi-analytical galaxy formation

[1] The "over cooling" and "quenching" problems are beyond the scope of this thesis (for a review, please see Silk et al., 2014, and references therein).

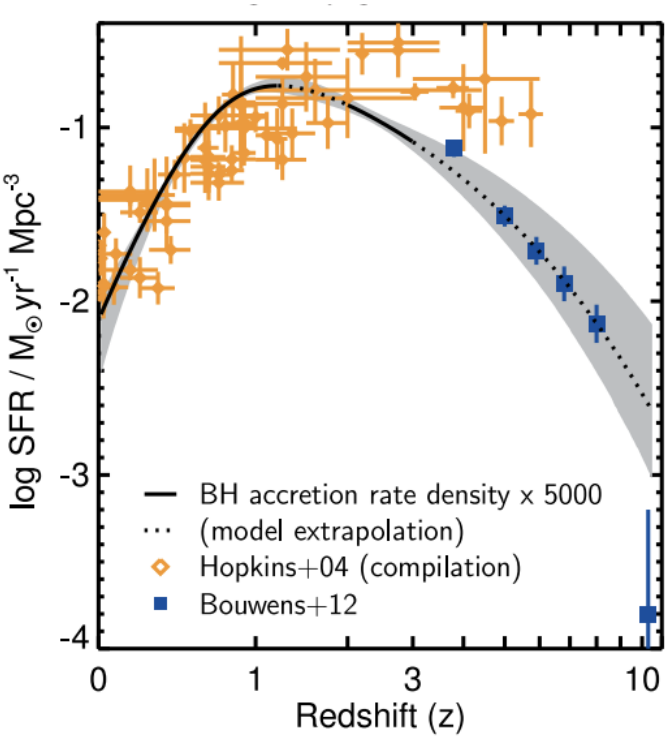

Figure 1.2 Observed star formation and black hole (BH) accretion histories track each other closely, preserving a ratio of $1,000:1$ and both peaking around $z \sim 1-2$. These similarities in growth histories have often been interpreted as additional evidence for the coevolution of BHs with their host galaxy (Kormendy & Ho, 2013a).

models and numerical simulations. In general, two different modes that could channel energy released by an AGN to surrounding gas are often considered: radiative (e.g., driven by BH accretion) and mechanical (e.g., driven by AGN winds or radio jets) (see, Mo et al., 2010, for more details regarding AGN feedback modes).

While AGN feedback is promising for the ΛCDM galaxy formation framework, others have proposed plausible explanations for the BH-host galaxy connection. One idea is that BH accretion and star formation are fed by the same gas reservoir, thus indirectly linking the two growth rates. In this scenario, BH growth and star formation do not directly influence one another, and the observed correlations are simply a result of the BH's inability to accrete material once star formation depletes their shared fuel supply (Cattaneo et al., 2009).

Additionally, the idea of a non-causal link due to the hierarchical assembly of galaxies was first proposed as a thought experiment by Peng (2007), who suggested the relations could result from statistical convergence. Peng (2007) demonstrated that the central limit theorem suggests the observed correlation may arise naturally by statistical consequence and that a large number of (dry) galaxy mergers will average out extreme values of M_{BH}/M_* toward the ensemble average. Since then, others have speculated that the BH-host galaxy connection may be regulated by the hierarchical assembly of BH mass and stellar mass through galaxy mergers (Hirschmann et al., 2010; Jahnke & Macciò, 2011) rather than AGN feedback. In this picture, the BH-host galaxy connection implied by the local BH scaling relations is merely a byproduct of galaxy evolution rather than a critical ingredient to galaxy formation.

For this reason, probing the BH scaling relations across redshift has become an active area of study (e.g., Treu et al., 2004; Peng et al., 2006a,b; Woo et al., 2006; Salviander et al., 2007; Jahnke et al., 2009; Bennert et al., 2010; Maiolino et al., 2010; Park et al., 2015; Silverman et al., 2019; Sexton et al., 2019; Ding et al., 2020a) to test the origin of the BH scaling relations. A true coevolution (i.e., regulated growth due to AGN feedback) suggests tight scaling relations across redshift. However, Croton (2006) predicts larger BH masses at earlier times if mergers are the primary drivers for bulge and BH growth. Meanwhile, a non-causal origin due to the hierarchical assembly of galaxies will result in an increased scatter at higher redshifts. Given the different behaviors predicted across redshift for each scenario, investigating the evolution of the BH scaling relations may help constrain theoretical interpretations of their origins and better understand the BH-host galaxy connection (Bennert et al., 2010).

In addition to studying the evolution of the BH scaling relations, probing the surrounding gas of accreting BHs in active galaxies may also help us understand the role BHs play in regulating star formation and galaxy growth (Booth & Schaye, 2009; Fabian, 2012; Somerville & Davé, 2015; Dubois et al., 2016). In particular, the broad emission line region (BLR) is the closest structure (of the order of $\sim$ light-days for low luminosity AGNs (Kaspi et al., 2000))

to the central BH and has been the focus of a wide range of AGN astrophysics studies. Such studies, including those outlined in this thesis, have the potential to help constrain the mechanism for gas transportation (e.g., via accretion disks or winds) required for AGN feedback.

One of the observational challenges of probing the surroundings of accreting BHs is that the nucleus outshines the rest of the host galaxy, and even the most powerful space telescopes cannot spatially resolve the BLR. Reverberation mapping (RM), however, provides a powerful tool to resolve the BH's gravitational sphere of influence in time. RM campaigns are variability studies that observe the variability of the ionizing continuum (assumed to originate from the accretion disk) and the broad emission lines (originating from the BLR). For low redshift AGN, such as those presented in this thesis, the optical Hβ broad emission line is observed to reverberate the variations observed in the ionizing continuum after a "time lag," τ. Assuming the observed time delay, τ, is due to light-travel time, the size of the BLR, or its radial distance from the central BH, r_{BLR}, is given by the simple relation: $r_{BLR} = c\tau$. Additionally, assuming that the motion of the BLR gas is virialized, the speed of the gas is given by the width of the broad emission line, v. Combining the size of the BLR with its velocity, a virial constraint of the black hole's mass (M_{BH}) is given by:

$$M_{BH} = f\frac{c\tau v^2}{G} = fM_{vir}, \tag{1.1}$$

where f, or the "virial coefficient," is a dimensionless scale factor of order unity that captures the relation between measured line-shape parameters and BLR geometry/dynamics, and $c\tau v^2/G$ is referred to as the virial product (M_{vir}).

Despite the technique's ability to resolve the BH's gravitational sphere of influence in time and provide BH mass estimates across cosmic time, much remains unknown about the broad emission line region (BLR). In principle, velocity-resolved RM (Blandford & McKee, 1982) can provide insight into the BLR structure and kinematics by mapping the BLR response as a

function of line-of-sight velocity. The transfer function describes the time-delay distribution across a broad emission line as a function of line-of-sight velocity (Horne, 1994; Skielboe et al., 2015). In other words, the transfer function can be thought of as a map from the AGN stochastic continuum variations to the emission-line response at some line-of-sight velocity, v_z, after some time delay, τ, (Peterson, 1993), and is expressed as:

$$L(v_z, t) = \int_{-\infty}^{\infty} \Psi(v_z, \tau)\ C(t - \tau)\ d\tau, \tag{1.2}$$

where $L(v_z, t)$ is the emission-line luminosity at line-of-sight velocity v_z observed at time t, $C(t)$ is the AGN continuum light curve, and $\Psi(v_z, \tau)$ is the transfer function. Because the transfer function's shape depends on the structure and kinematics of the BLR (Horne et al., 2004), one can theoretically use the transfer function to constrain the BLR geometry. In practice, however, the interpretation of a transfer function is nontrivial since different geometries can produce similar features. For this reason, it is impossible to determine the virial coefficient, f, (meant to encapsulate the geometry and kinematics of the BLR) for an individual AGN using traditional RM techniques. Instead, a constant average scale factor, found by aligning reverberation-mapped AGNs to the local M_{BH}–σ_* relation, is often used for traditional RM BH mass estimates (Onken et al., 2004; Collin et al., 2006a; Woo et al., 2010, 2013; Graham et al., 2011; Park et al., 2012a; Grier et al., 2013; Woo et al., 2015; Batiste et al., 2017).

The goal of this dissertation is twofold: (i) characterize the structure and kinematics of the broad emission line region (BLR) to better understand the central regions of AGN and (ii) improve how BH mass measurements are calibrated across cosmic time. While both goals aim to provide insight into the role AGNs play in galaxy evolution, the latter is most relevant for studies of the evolution of the BH scaling relations and galaxy evolution studies in the era of JWST (e.g., Maiolino et al., 2023; Mezcua et al., 2024; Pacucci & Loeb, 2024).

This dissertation is organized as follows. In Chapter 2, I model the Hβ BLR of nine AGNs observed during the Lick AGN Monitoring Project (LAMP) 2016 campaign and investigate whether there are any luminosity-dependent trends in the structure and kinematics of the Hβ BLR. In Chapter 3, I combine the LAMP 2016 modeling results presented in Chapter 2 with those of Pancoast et al. (2014), Grier et al. (2017), Williams et al. (2018), Williams et al. (2020), Bentz et al. (2021), and Bentz et al. (2022), and search for a way to improve how BH masses are calibrated across cosmic time. In Chapter 4, I expand on the initial development and testing of CARAMEL-GAS (Williams & Treu, 2022), which aims to model the gas density field of the BLR and model multiple emission lines simultaneously, e.g., Hα and Hβ, to learn about the surroundings of active BHs. However, further testing and development beyond the work presented in this thesis is required to achieve this goal. Finally, I provide a summary and future direction for the studies presented in this work in Chapter 5.

CHAPTER 2

The Lick AGN Monitoring Project 2016: Dynamical Modeling of Velocity-Resolved Hβ Lags in Luminous Seyfert Galaxies

This chapter was published as Villafaña, L., Williams, P.R., Treu, T. et al.; "The Lick AGN Monitoring Project 2016: Dynamical Modeling of Velocity-Resolved Hβ Lags in Luminous Seyfert Galaxies," ApJ, 930, 52 (2022), and is reproduced here with minor formatting adjustments

2.1 Introduction

Over the last few decades, reverberation mapping has enabled the black hole (BH) mass measurements of over 70 active galactic nuclei (AGNs) and facilitated the use of single-epoch BH mass measurements across cosmic time (Bentz & Katz, 2015a). Despite the technique's ability to resolve the BH's sphere of influence in time, much remains unknown about the broad emission line region (BLR). And while the promise of velocity-resolved reverberation mapping has increased significantly over the last decade, analysis requires recovery of a nontrivial transfer function.

In principle, velocity-resolved reverberation mapping (Blandford & McKee, 1982) can provide insight into the BLR structure and kinematics by mapping the BLR response as a function

of line-of-sight velocity. However, doing so requires a high signal-to-noise ratio (S/N), high cadence, and a lengthy observational campaign, and thus has only been applied to $\sim$ 30 AGNs over roughly the last decade (e.g., Bentz et al., 2009; Denney et al., 2009, 2010; Barth et al., 2011a,b; Grier et al., 2013; Du et al., 2016; Pei et al., 2017a; De Rosa et al., 2018; Du et al., 2018; Li et al., 2021; Feng et al., 2021). Nonetheless, information regarding the BLR collected from these campaigns is not straightforward, as the BLR structure and kinematics are embedded in the so-called transfer function.

The transfer function describes the time-delay distribution across a broad emission line as a function of line-of-sight velocity (Horne, 1994; Skielboe et al., 2015). In other words, the transfer function can be thought of as a map from the AGN stochastic continuum variations to the emission-line response at some line-of-sight velocity v_z, after some time delay τ, (Peterson, 1993), and is expressed as:

$$L(v_z, t) = \int_{-\infty}^{\infty} \Psi(v_z, \tau)\ C(t - \tau)\ d\tau, \tag{2.1}$$

where $L(v_z, t)$ is the emission-line luminosity at line-of-sight velocity v_z at observed time t, $C(t)$ is the AGN continuum light curve, and $\Psi(v_z, \tau)$ is the transfer function. Because the shape of the transfer function depends on the structure and kinematics of the BLR (Horne et al., 2004), one can theoretically use the transfer function to constrain the BLR geometry. In practice, however, interpretation of a transfer function is nontrivial since different geometries can produce similar features.

As an alternative analysis, one can instead use the methods introduced by Pancoast et al. (2011, hereafter P11) to explore and constrain a phenomenological description of the BLR that is consistent with the reverberation mapping dataset. In this approach, using the Code for AGN Reverberation and Modeling of Emission Lines (CARAMEL), the BLR emissivity is described in simple but flexible terms, allowing one to capture the key features expressed in

the data in a statistically rigorous way. The posterior probability distribution function of parameters describing the geometry and kinematics of the line emissivity are derived through a diffusive nested sampling process. The parameter uncertainties account for the inevitable modeling approximation as described by Pancoast et al. (2011, 2014) and briefly summarized in this paper.

This phenomenological model allows us to learn more about the BLR and has been applied to the low-ionization Hβ-emitting BLR of a total of 18 AGNs — five from the Lick AGN Monitoring Project 2008 (LAMP 2008; Pancoast et al., 2014, hereafter P14), four from a 2010 AGN monitoring campaign at MDM Observatory (AGN10; Grier et al., 2017, hereafter G17), seven from the Lick AGN Monitoring Project 2011 (LAMP 2011; Williams et al., 2018, hereafter W18), one from the Space Telescope and Optical Reverberation Mapping Project (AGNSTORM; Williams et al., 2020, hereafter W20)[1], and one from a monitoring campaign at Siding Spring Observatory (SSO; Bentz et al., 2021, hereafter B21). These analyses found that the Hβ-emitting BLR is best described by a thick disk at a low to moderate inclination to our line of sight with near-circular Keplerian orbits and a contribution of inflow (with some outflow found by W18).

In an attempt to gain further insight on the Hβ-emitting BLR structure and kinematics, we have expanded the sample of dynamically modeled AGNs from 18 to 27 by analyzing velocity-resolved reverberation mapping data for nine AGNs from the Lick AGN Monitoring Project 2016 campaign (LAMP 2016; U et al., 2022). This paper is organized as follows. We describe our photometric and spectroscopic campaigns and briefly summarize the BLR model from P11 in Section 2.2. Section 2.3 presents the CARAMEL BLR structure and kinematics of the nine LAMP 2016 sources modeled. With these results, we compare our model kinematics

[1]NGC 5548 was previously modeled using data from the LAMP 2008 campaign. Modeling data from the AGNSTORM campaign yields the same black hole mass but different geometry of the BLR. This is not surprising, as different aspects of the BLR (luminosity and average size, for example) are known to vary over timescales of a few years (see, e.g., De Rosa et al., 2015; Pancoast et al., 2018; Kara et al., 2021). It is thus interesting to include the results of both campaigns in our analysis.

to those inferred by U et al. (2022) using traditional velocity-delay maps in Section 2.4. Finally, we combine our results with previous studies to create an extended sample that covers more than two decades in luminosity, and investigate luminosity-dependent trends and line-profile shape, e.g., $\log_{10}(FWHM/\sigma)$, dependence on BLR structure and kinematics. We summarize our main conclusions in Section 2.5.

Throughout the paper, we have adopted $H_0 = 67.8\ km\ s^{-1}\ Mpc^{-1}$, $\Omega_m = 0.308$, and $\Omega_{vac} = 0.692$ (Planck Collaboration et al., 2016).

2.2 Data and Methods

2.2.1 Photometric and Spectroscopic Data

A detailed description of the photometric and spectroscopic monitoring data is provided by U et al. (2022). In summary, V-band photometric monitoring was carried out from February 2016 to May 2017 using a network of telescopes around the world, including the 0.76 m Katzman Automatic Imaging Telescope (KAIT; Filippenko et al., 2001) and the Nickel telescope at Lick Observatory on Mount Hamilton east of San Jose, California; the Las Cumbres Observatories Global Telescope (LCOGT) network (Brown et al., 2013; Boroson et al., 2014); the Liverpool Telescope at the Observatorio del Roque de Los Muchachos on the Canary island of La Palma, Spain (Steele et al., 2004); the 1 m Illinois Telescope at Mount Laguna Observatory (MLO) in the Laguna Mountains east of San Diego, California; the San Pedro Mártir Observatory (SPM) 0.84 m telescope at the Observatory Astronómico Nacional located in Baja California, México; the Fred Lawrence Whipple Observatory 1.2 m telescope on Mount Hopkins, Arizona; and the 0.9 m West Mountain Observatory (WMO) Telescope at the southern end of Utah Lake in Utah. Spectroscopic monitoring was carried out with the Kast double spectrograph on the 3 m Shane telescope at Lick Observatory from 28 April 2016 to 6 May 2017; originally allocated 100 nights, a substantial fraction ($\sim 30\%$) were unfortunately lost owing to poor weather.

Table 2.1. AGN Observation Properties

Galaxy	Alt. Name	Redshift	Monitoring Period (UT)	N_{spec}	S/N	N_{phot}
PG 2209+184	II Zw 171	0.07000	20160501−20161231	40	32	9
RBS 1917	2MASX J22563642+0525167	0.06600	20160601−20161231	32	39	9
MCG +04-22-042		0.03235	20160501−20170501	34	54	7
NPM1G+27.0587	2MASX J18530389+2750275	0.06200	20160501−20161203	38	55	7
Mrk 1392	1505 + 0342	0.03614	20160501−20170501	39	55	10
RBS 1303	CGS R14.01	0.04179	20160501−20170501	22	67	5
Mrk 1048	NGC 985, VV 285	0.04314	20160808−20170216	27	88	5
RXJ 2044.0+2833		0.05000	20160501−20161231	46	58	9
Mrk 841	J15040+1026	0.03642	20160501−20170501	45	77	11

Note. — Observing information for the AGNs modeled in this work. The redshifts are from U et al. (2022). N_{spec} represents the total number of spectroscopic observations for each source. S/N represents the median signal-to-noise ratio per pixel in the Hβ spectrum in the continuum at $(5100-5200)\,(1+z)$. N_{phot} represents the number of photometric nights for each source.

The total number of epochs for each object analyzed in this work can be found in Table 2.1. In total, 21 AGNs were observed during the campaign. Of those, nine had sufficient quality and continuum/Hβ variability for the analysis conducted in this paper. The reader is referred to U et al. (2022) for the full list of AGNs observed during this campaign.

To model the broad Hβ emission line, we must disentangle it from other features in the AGN spectrum, such as the He1, He2, Fe2, and [O3] emission lines, the AGN continuum, and starlight. Our team isolates contributions of individual emission lines and continuum components within the vicinity of the Hβ emission line by fitting a multicomponent model to each night's spectrum (see Figure 2.1). A summary of the procedure, adopted from Barth et al. (2015a) and used on the LAMP 2016 sample, is given by U et al. (2022).

2.2.2 BLR Model

We model the Hβ-emitting BLR of each source using CARAMEL, a phenomenological modeling code described in detail by P11 and P14. CARAMEL models the BLR emission by sampling it with a distribution of test point particles surrounding the black hole located at the origin. Gravity is assumed to be the dominant force (i.e., radiation pressure is neglected). When ionizing light emitted from the central black hole reaches a particle, the particle instantaneously re-emits an emission line and the CARAMEL model free parameters determine whether the re-emission is isotropic. The spatial distribution of the particles determines the associated time delay, while the line-of-sight velocity distribution determines the shape of the broad emission line profile. The spatial and velocity distributions of the point particles are constrained by a number of model parameters described by P11 and P14. Here we summarize some of the main parameters.

2.2.2.1 Geometry

The spatial distribution of particles is described by angular and radial components. The radial distribution is drawn from a gamma distribution with shape parameter β and mean

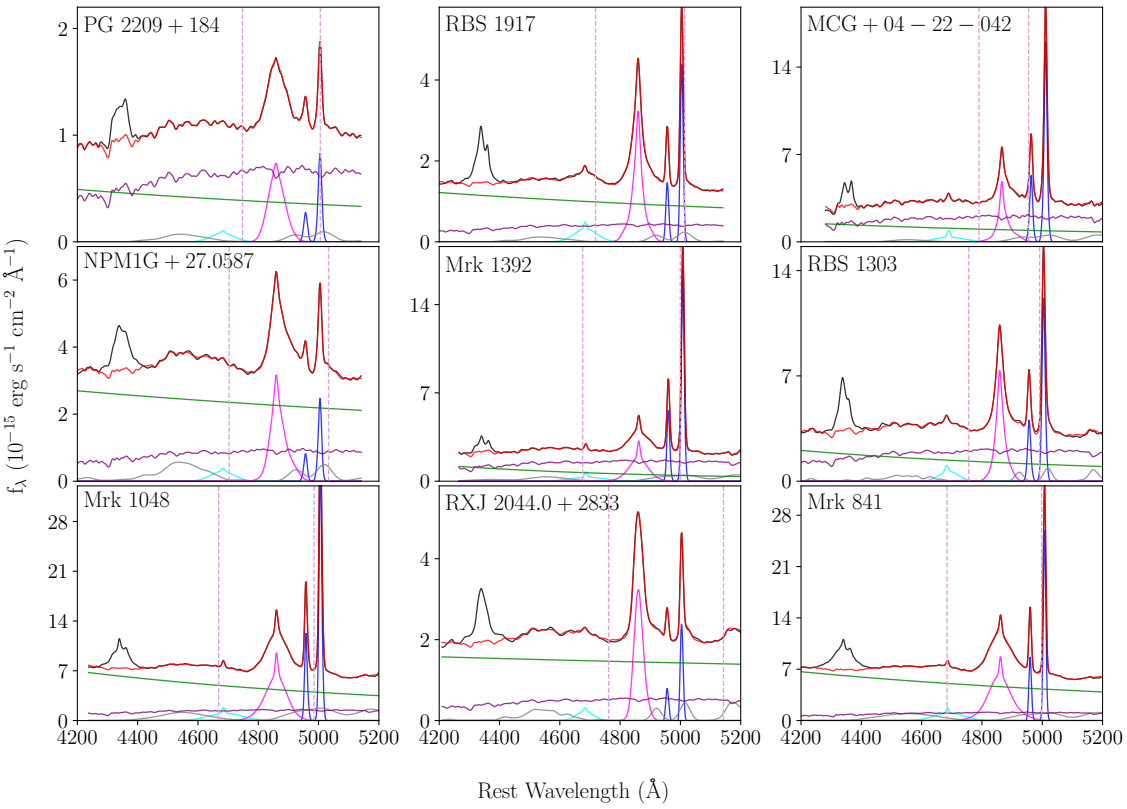

Figure 2.1 Spectral decomposition using the K10 Fe2 template. The observed mean spectrum (black) for each galaxy is plotted alongside the decomposed model components: starlight (purple), AGN power-law continuum (green), Hβ λ4861 (magenta), He2 λ4686 (cyan), He1 λ5876 (orange), Fe2 $\lambda(4500-5400)$ (grey), and [O3] λ5007 (blue). The sum of the fit of these components is shown in red and the vertical dashed lines indicate the wavelength range used for fitting the Hβ-emitting BLR model.

μ that has been shifted from the origin by a minimum radius r_{min}. Spherical symmetry is broken by introducing an opening-angle parameter, θ_o, which can be interpreted as disk thickness with $\theta_o \rightarrow 0°$ describing a razor-thin disk and $\theta_o \rightarrow 90°$ describing a sphere. Inclination to the observer's line of sight is set by an inclination angle θ_i, with $\theta_i = 0°$ representing a face-on view and $\theta_i = 90°$ representing an edge-on view. Three additional parameters (γ, ξ, and κ) allow for further asymmetry.

The extent to which the emission is concentrated near the outer edges of the BLR is then determined by γ, which ranges in values from 1 to 2. A uniform distribution throughout the disk is described by $\gamma \to 1$ and a clustered distribution at the outer edges of the BLR disk is described by $\gamma \to 2$. The parameter ξ permits obscuration along the midplane of the disk, with $\xi \to 0$ interpreted as a fully obscured (opaque) midplane and $\xi = 1$ as a fully transparent midplane (i.e., no obscuration). The parameter κ is related to the relative brightness of each particle and controls how the continuum flux is radiated toward the observer as emission-line flux. While $\kappa = 0$ represents isotropic emission, $\kappa = -0.5$ represents preferential emission toward the origin (back toward the ionizing source) and $\kappa = 0.5$ represents preferential emission away from the origin (and away from the ionizing source). An observer viewing from $+\infty$ along the x-axis would view the first as preferential emission from the far side of the BLR, and the latter as preferential emission from the near side of the BLR. Preferential emission from the far side of the BLR can be interpreted as a result of self-shielding particles or obscuration (of the near-side BLR) by the torus, causing the BLR gas to appear to only re-emit back toward the ionizing source. Preferential emission from the near side might be due to an obstructed view of the far side of the BLR.

2.2.2.2 Dynamics

Following the construction of the spatial distribution of particles, the BLR kinematics are then determined with a number of additional parameters. The fraction of particles with near-circular Keplerian orbits around the central black hole with mass M_{BH} is given by the f_{ellip} parameter. The remaining particles $(1 - f_{ellip})$ are either inflowing ($f_{flow} < 0.5$) or outflowing ($f_{flow} > 0.5$) with velocities drawn from a Gaussian distribution centered on the radial escape velocity in the $v_r - v_\phi$ plane rotated by an angle, θ_e, away from escape velocity toward circular velocity. Therefore $\theta_e \to 90^\circ$ indicates nearly circular orbits, $\theta \approx 45^\circ$ highly eccentric orbits, and $\theta_e \to 0^\circ$ a majority of particles are approaching escape velocity and are nearly unbound.

Finally, we add the line-of-sight velocity component, v_{turb}, of a randomly-orientated macroturbulent velocity vector to the particle's line-of-sight velocity. This macroturbulent contribution is drawn from a Gaussian distribution, $\mathcal{N}$, centered on 0 with standard deviation σ_{turb} and is dependent on the particle's circular velocity v_{circ}:

$$v_{turb} = \mathcal{N}(0, \sigma_{turb})|v_{circ}|, \tag{2.2}$$

where σ_{turb} is the free parameter that determines the amount of contribution from macroturbulent velocities and can range from 0.001 to 0.1.

For simplicity, we summarize the BLR dynamics by an "In.−Out." parameter as defined by W18, where values of 1 indicate pure radial outflow and −1 indicate pure radial inflow:

$$In. - Out. = sgn(f_{flow} - 0.5) \times (1 - f_{ellip}) \times \cos(\theta_e). \tag{2.3}$$

2.2.2.3 Continuum Model and Implementation

In order to use the parameterized spatial and velocity distributions described above to calculate the resulting broad emission-line profile at arbitrary times, we need an input continuum light curve that can *also* be sampled at arbitrary times. To do this, we model the AGN continuum using Gaussian processes. This allows us to both interpolate between photometric measurements and extrapolate beyond the monitoring campaign, as well as propagate the associated uncertainties into the determination of the BLR model parameters. By combining the modelled continuum light curve with the BLR model parameters, a broad emission line profile can be produced for each spectroscopic epoch observed during the monitoring campaign.

This last step requires the application of a smoothing parameter to account for minor differ-

ences in spectral resolution throughout the observational campaign, due to variable seeing conditions, for example. We assume that the narrow [O3] emission line remains intrinsically constant throughout our monitoring campaign and use it to calibrate the smoothing parameter by comparing its measured width to its width taken from Whittle (1992). We then use this smoothing parameter to blur the modeled spectrum and combine with the modeled particle dynamics to produce the Hβ emission-line profile.

Once the model emission-line profile is produced, we use a Gaussian likelihood function to compare the resulting spectra with the observed spectra, and adjust the BLR model parameters accordingly. We explore the model parameter space using DNEST4 (Brewer et al., 2011), a diffusive nested sampling code that allows one to apply a likelihood softening parameter post-analysis. This parameter is a statistical "temperature," T, which allows us to account for systematic uncertainty by increasing measurement uncertainty, as well as account for our simple model's inability to capture all the real details. We select a value for T that avoids overfitting while still achieving the highest levels of likelihood.

2.2.2.4 Model Limitations

Before proceeding onto the discussion of our results, we would like to reiterate that CARAMEL models the *BLR emission*, rather than the underlying BLR gas distribution producing the emission lines. Our model does not include photoionization processes. Doing so would require additional assumptions about the gas density, temperature, metallicity distribution, and the relation between the observed V-band continuum and the ionizing spectrum. Therefore, the interpretation of the model parameters discussed below in Section **??** is a reflection of the Hβ BLR *emission*, rather than the underlying gas producing the emission lines.

Additionally, our model is currently set up to only account for gravitational effects from the central BH and does not take into account the effects of radiation pressure. This is important to keep in mind when interpreting model results for high Eddington ratio AGNs. We note

that the sources modeled in this work have moderate luminosities, with extinction-corrected $\log[\lambda L_\lambda(5100)/L_\odot] \approx 43.5$–$43.9$ (U et al., 2022). The precise Eddington ratio is difficult to determine, however, since bolometric correction factors may depend on the true Eddington ratio and other parameters. For the purposes of this work, we remain consistent in our calculations and apply the same bolometric correction factor as our prior studies (P14; G17; W18). Within our extended sample, we find that the Eddington ratio of the LAMP 2016 sources can also be considered moderate when compared to prior studies (e.g., G17), but find this model limitation worth noting as neglecting radiation pressure can potentially lead to biased results for sources with high Eddington ratio.

For further discussion of model limitations and the model improvements that are currently underway, the reader is referred to Raimundo et al. (2020).

2.2.3 Searching for Trends with BLR Structure and Kinematics

In addition to learning more about the Hβ-emitting BLR, a primary goal of this program is to investigate the existence of any systematic trends in AGN BLR structure and kinematics. This is part our team's long-standing goal to gain insight on the nature of the BLR through our dynamic modeling approach, and ultimately improve BH mass estimators (see **?**, for the latter). In this work, we specifically search for luminosity-dependent and line-profile shape dependency on BLR structure/dynamics.

We use the IDL routine `linmix_err` (Kelly, 2007) to perform a Bayesian linear regression in order to account for correlated measurement uncertainties. Doing so allows us to analyze the actual intrinsic correlation with any two parameters without worrying about a false increase due to correlated measurement uncertainties. This is especially important for our search for correlations with scale factor since individual scale factors are determined using our model black hole mass estimate, and therefore its uncertainties are connected to uncertainties in other model parameters.

To quantify the strength of any correlation, we compare the median fit slope to the 1σ uncertainty in the slope and determine our level of confidence using the following intervals we have defined previously (W18). We classify 0–2σ as no evidence, 2–3σ as marginal evidence, 3–5σ as evidence, and $> 5\sigma$ as conclusive evidence.

2.3 Results

Of the 21 sources from our full sample, U et al. (2022) determine 16 sources to have reliable time lags. Of those 16, nine have sufficient data quality/variability to model using CARAMEL. To verify that our model fits the data, we compare our continuum light curve, the Hβ line profile shape from a randomly selected night, and the resultant modeled integrated Hβ emission line to those observed.

We exclude results for three additional sources whose models were determined to only fit the data with moderate quality. We note, however, that although we chose not to include these results in our extended sample with prior studies, including these sources does not significantly change any findings presented in this work or that of Villafaña et al. (2023). We include the CARAMEL results in Appendix 2.6 for readers who may still be interested in our model description of these three sources.

Here we present the details for the nine sources determined to have good model fits (Figures 2.3–2.11). An overview of model parameter estimates is provided in Table 2.2. Overall, the Hβ-emitting BLR is best described as a thick disk observed at low to moderate inclination angles with diverse kinematics, as depicted in Figure 2.2. We find black hole mass estimates that are consistent (within at least $\sim 3\sigma$) with velocity-resolved reverberation mapping estimates determined by U et al. (2022), using a value of $\log_{10}(f_{rms,\sigma})= 0.65$ for the virial coefficient.

Table 2.2. BLR Model Parameter Values

Parameter	**PG** 2209 +184	**RBS** 1917	**MCG** +04 − 22 −042	**NPM1G** +27.0587	**Mrk** 1392	**RBS** 1303	**Mrk** 1048	**RXJ** 2044.0 +2833	**Mrk** 841
$\log_{10}(M_{bh}/M_{\odot})$	$7.53^{+0.19}_{-0.20}$	$7.04^{+0.23}_{-0.35}$	$7.59^{+0.42}_{-0.28}$	$7.64^{+0.40}_{-0.36}$	$8.16^{+0.11}_{-0.13}$	$6.79^{+0.19}_{-0.11}$	$7.79^{+0.44}_{-0.48}$	$7.09^{+0.17}_{-0.17}$	$7.62^{+0.50}_{-0.30}$
r_{mean} (light-days)	$16.27^{+1.00}_{-0.95}$	$9.3^{+1.4}_{-1.6}$	$9.94^{+1.20}_{-0.98}$	$12.2^{+4.3}_{-3.5}$	$56.0^{+12.0}_{-7.2}$	$12.9^{+1.3}_{-1.2}$	$14.2^{+7.8}_{-7.6}$	$35.7^{+7.8}_{-6.3}$	$14.1^{+7.1}_{-4.4}$
r_{median} (light-days)	$15.2^{+1.1}_{-1.0}$	$5.0^{+1.3}_{-1.1}$	$6.24^{+1.01}_{-0.87}$	$7.2^{+2.8}_{-2.0}$	$51.6^{+12.2}_{-8.6}$	$10.1^{+1.3}_{-1.2}$	$11.3^{+7.3}_{-6.2}$	$28.3^{+7.5}_{-5.4}$	$10.6^{+5.6}_{-3.4}$
r_{min} (light-days)	$2.8^{+1.4}_{-1.6}$	$1.42^{+0.39}_{-0.40}$	$1.05^{+0.65}_{-0.58}$	$2.69^{+1.6}_{-0.95}$	41^{+11}_{-12}	$0.25^{+0.24}_{-0.18}$	$3.3^{+3.0}_{-2.1}$	$4.2^{+1.5}_{-1.1}$	$2.0^{+1.8}_{-1.1}$
σ_r (light-days)	22^{+12}_{-8}	27^{+25}_{-12}	$21.5^{+35.3}_{-9.7}$	$22.0^{+18}_{-9.2}$	31^{+54}_{-18}	$13.6^{+3.8}_{-2.3}$	$14.1^{+22}_{-8.7}$	55^{+45}_{-17}	$14.7^{+15}_{-5.8}$
τ_{mean} (days)	$15.75^{+0.74}_{-0.77}$	$9.0^{+1.9}_{-1.7}$	$9.17^{+0.95}_{-0.81}$	$10.7^{+3.1}_{-2.8}$	$38.7^{+4.6}_{-4.2}$	$13.7^{+1.3}_{-1.3}$	$11.5^{+6.6}_{-6.0}$	$30.2^{+4.8}_{-5.3}$	$13.5^{+4.6}_{-3.8}$
τ_{median} (days)	$12.95^{+0.87}_{-0.88}$	$4.6^{+1.2}_{-1.2}$	$5.58^{+0.81}_{-0.70}$	$6.0^{+2.0}_{-1.6}$	$34.8^{+4.6}_{-4.6}$	$9.8^{+1.2}_{-1.1}$	$8.2^{+6.2}_{-4.5}$	$18.8^{+3.5}_{-3.9}$	$8.9^{+3.3}_{-2.5}$
β	$0.88^{+0.14}_{-0.15}$	$1.63^{+0.13}_{-0.16}$	$1.40^{+0.20}_{-0.19}$	$1.54^{+0.13}_{-0.13}$	$1.29^{+0.51}_{-0.74}$	$0.94^{+0.07}_{-0.07}$	$1.12^{+0.28}_{-0.28}$	$1.12^{+0.08}_{-0.08}$	$1.08^{+0.18}_{-0.16}$
θ_o (degrees)	$29.1^{+11.0}_{-8.4}$	$25.1^{+9.2}_{-7.5}$	$13.6^{+6.9}_{-4.9}$	$18^{+11}_{-9.1}$	$41.2^{+5.3}_{-4.8}$	$34.0^{+8.9}_{-10}$	$31^{+14}_{-10.0}$	51^{+15}_{-12}	41^{+11}_{-11}
θ_i (degrees)	$30.2^{+8.7}_{-6.9}$	$20.2^{+9.9}_{-3.9}$	$11.3^{+5.8}_{-5.0}$	$19^{+11}_{-8.5}$	$25.5^{+3.4}_{-2.8}$	$29.1^{+7.7}_{-9.0}$	$21.5^{+9.4}_{-9.4}$	$42.5^{+9.6}_{-8.4}$	30^{+11}_{-15}
κ	$-0.09^{+0.12}_{-0.15}$	$-0.29^{+0.35}_{-0.14}$	$-0.14^{+0.44}_{-0.27}$	$-0.14^{+0.40}_{-0.25}$	$0.26^{+0.18}_{-0.25}$	$-0.48^{+0.05}_{-0.01}$	$0.10^{+0.28}_{-0.38}$	$-0.20^{+0.33}_{-0.19}$	$-0.23^{+0.43}_{-0.14}$
γ	$1.40^{+0.38}_{-0.28}$	$1.48^{+0.32}_{-0.32}$	$1.65^{+0.26}_{-0.36}$	$1.39^{+0.38}_{-0.27}$	$1.53^{+0.32}_{-0.33}$	$1.85^{+0.11}_{-0.21}$	$1.47^{+0.33}_{-0.32}$	$1.37^{+0.44}_{-0.29}$	$1.41^{+0.42}_{-0.29}$
ξ	$0.73^{+0.16}_{-0.18}$	$0.68^{+0.25}_{-0.35}$	$0.43^{+0.35}_{-0.26}$	$0.11^{+0.37}_{-0.09}$	$0.25^{+0.28}_{-0.18}$	$0.60^{+0.22}_{-0.16}$	$0.30^{+0.42}_{-0.20}$	$0.17^{+0.28}_{-0.12}$	$0.68^{+0.23}_{-0.41}$
f_{ellip}	$0.54^{+0.10}_{-0.15}$	$0.59^{+0.14}_{-0.17}$	$0.39^{+0.21}_{-0.18}$	$0.44^{+0.19}_{-0.18}$	$0.81^{+0.04}_{-0.06}$	$0.18^{+0.17}_{-0.11}$	$0.73^{+0.09}_{-0.13}$	$0.41^{+0.32}_{-0.29}$	$0.33^{+0.24}_{-0.22}$
f_{flow}	$0.24^{+0.17}_{-0.16}$	$0.59^{+0.28}_{-0.39}$	$0.27^{+0.18}_{-0.19}$	$0.26^{+0.18}_{-0.19}$	$0.74^{+0.18}_{-0.18}$	$0.75^{+0.17}_{-0.19}$	$0.74^{+0.18}_{-0.19}$	$0.22^{+0.19}_{-0.15}$	$0.45^{+0.36}_{-0.29}$
θ_e (degrees)	24^{+23}_{-16}	20^{+21}_{-15}	19^{+20}_{-13}	36^{+35}_{-24}	25^{+14}_{-15}	$8.3^{+8.8}_{-5.8}$	15^{+15}_{-10}	34^{+32}_{-21}	51^{+20}_{-27}
$In.-Out.$	$-0.40^{+0.09}_{-0.09}$	$0.24^{+0.21}_{-0.63}$	$-0.55^{+0.27}_{-0.17}$	$-0.41^{+0.25}_{-0.18}$	$0.16^{+0.05}_{-0.03}$	$0.80^{+0.11}_{-0.18}$	$0.24^{+0.11}_{-0.09}$	$-0.37^{+0.17}_{-0.23}$	$-0.33^{+0.55}_{-0.31}$
σ_{turb}	$0.01^{+0.05}_{-0.01}$	$0.01^{+0.04}_{-0.01}$	$0.01^{+0.02}_{-0.00}$	$0.01^{+0.05}_{-0.01}$	$0.01^{+0.04}_{-0.01}$	$0.01^{+0.02}_{-0.00}$	$0.01^{+0.04}_{-0.01}$	$0.01^{+0.03}_{-0.01}$	$0.01^{+0.05}_{-0.01}$

Note. — Median values and 68% confidence intervals for BLR model parameters. Note that r_{out} is a fixed parameter, so we do not include uncertainties.

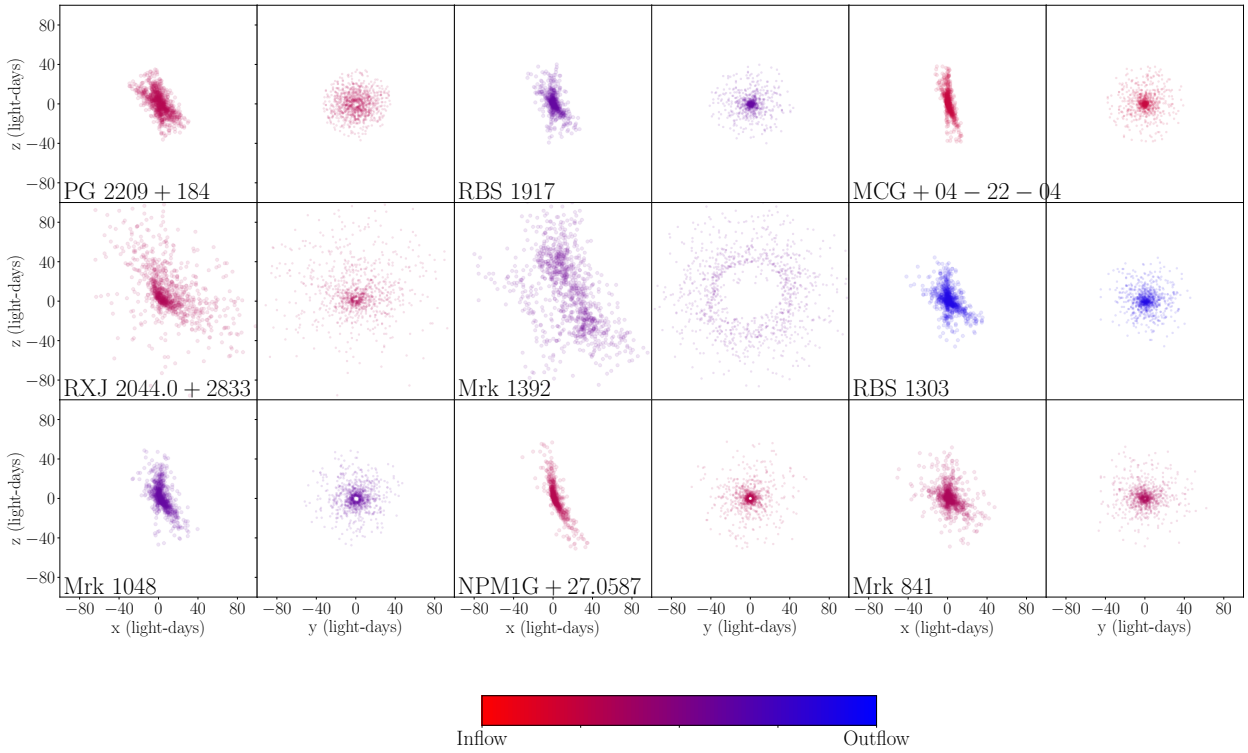

Figure 2.2 Geometric interpretation of BLR emission for the nine LAMP 2016 modeled sources using median parameter estimates. For each source, the left panel shows an edge-on view, while the right panel shows a face-on view. Each circle corresponds to one point particle in the model. The geometries are color-coded to indicate whether the BLR dynamics exhibit inflow (red) or outflow (blue).

2.3.1 PG 2209+184

Our model finds a BLR mean radius of $r_{median} = 15.2^{+1.1}_{-1.0}$ light-days and corresponding mean lag of $\tau_{median} = 12.95^{+0.87}_{-0.88}$ light-days. The opening and inclination angles are $\theta_o = 29.1^{+11.0}_{-8.4}$ degrees and $\theta_i = 30.2^{+8.7}_{-6.9}$ degrees, respectively, indicating a thick-disk structure slightly inclined toward the observer. Our model finds a strong preference for a transparent midplane ($\xi = 0.73^{+0.16}_{-0.18}$), but is unable to constrain whether Hβ emission is isotropic/concentrated at the edges ($\gamma = 1.40^{+0.38}_{-0.28}$) nor whether emission from the far/near sides of the BLR is preferred ($\kappa = -0.09^{+0.12}_{-0.15}$). Dynamically, 54% of particles have nearly circular orbits ($f_{ellip} = 0.54^{+0.10}_{-0.15}$) while the rest are on inflowing ($f_{flow} = 0.24^{+0.17}_{-0.16}$) orbits with velocities drawn

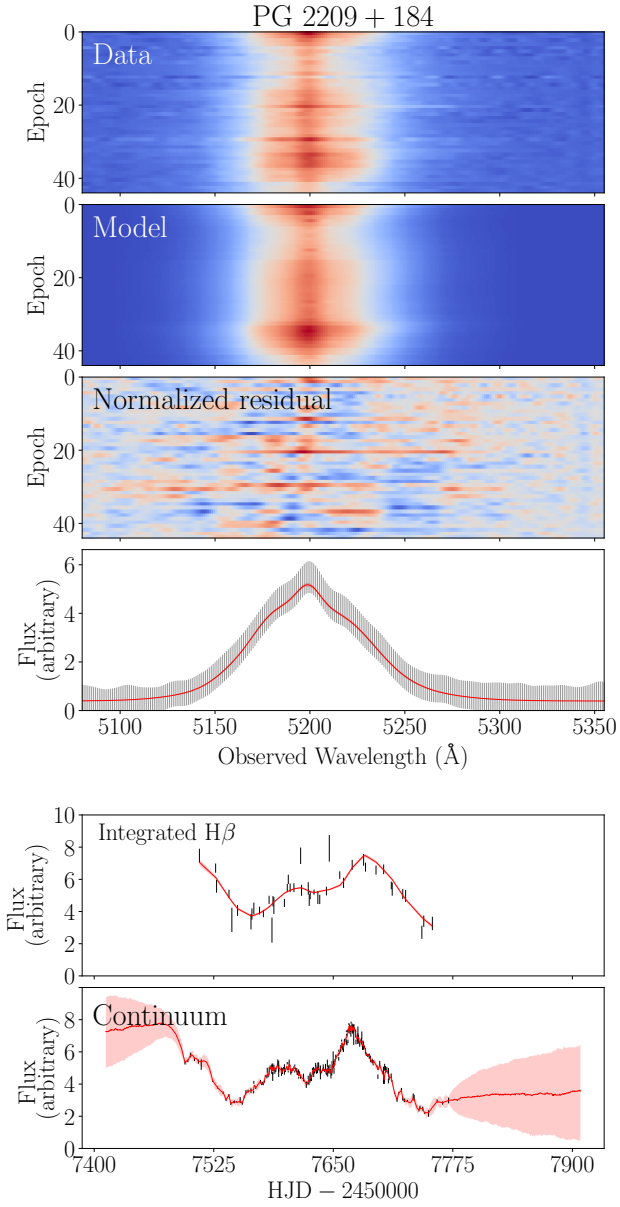

Figure 2.3 Model fits to the Hβ line profile, integrated Hβ flux, and AGN continuum flux for PG 2209+184. Labeling panels 1–6 from top to bottom, panels 1 and 2 show the observed intensity of the Hβ emission-line profile by observation epoch and the profile produced by one sample of the CARAMEL BLR and continuum model. Panel 3 displays the resulting normalized residual. Panel 4 shows the observed Hβ profile of one randomly chosen epoch in black and the corresponding profile produced by the model in panel 2, in red. The corresponding error bars of the observed epoch have been multiplied by $\sqrt{T}$, where T is the DNEST4 statistical "temperature" that is used as a likelihood softening parameter post analysis. Panels 5 and 6 illustrate the time series of the observed integrated Hβ and continuum flux in black and the corresponding model fits (of the model shown in panel 2) of the light curves in red.

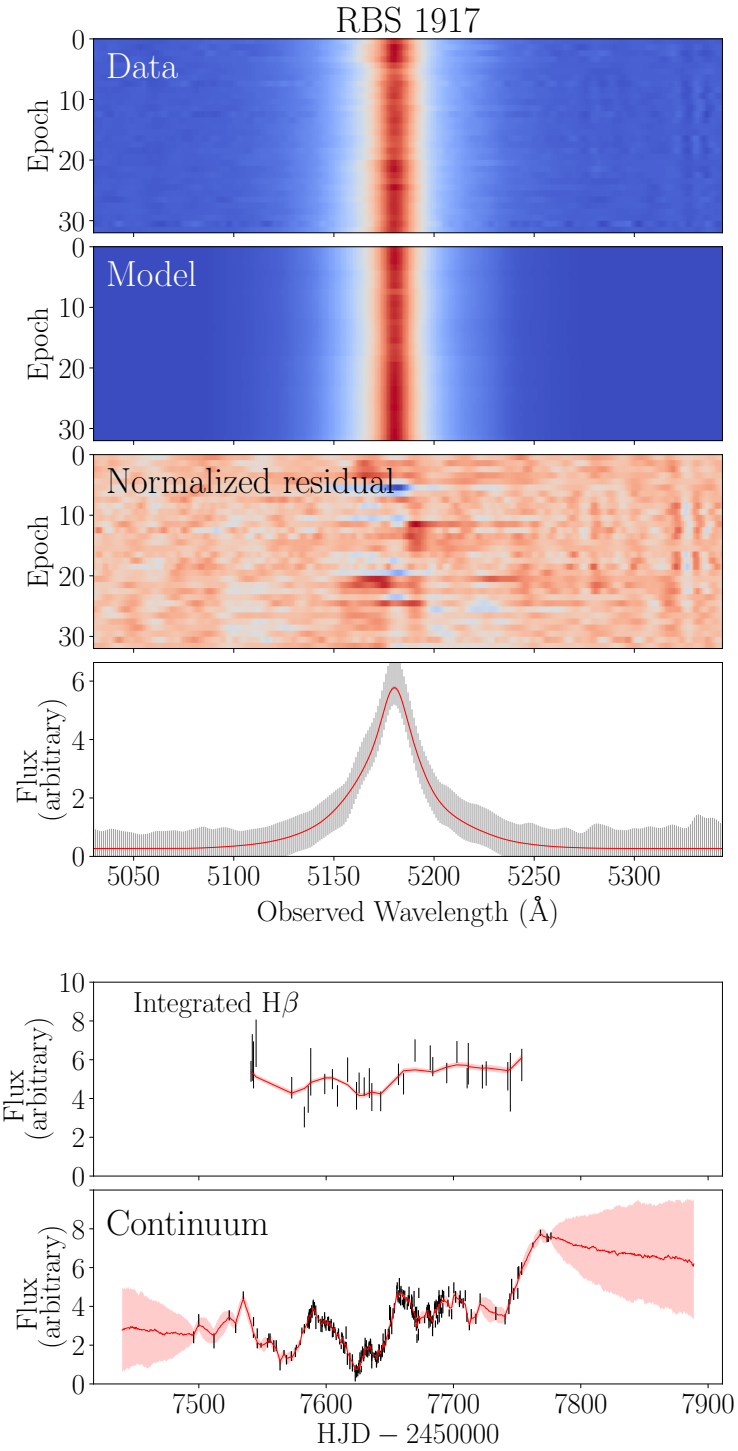

Figure 2.4 Model fits to the Hβ line profile, integrated Hβ flux, and AGN continuum flux for RBS 1917. See Figure 2.3 caption for panel descriptions.

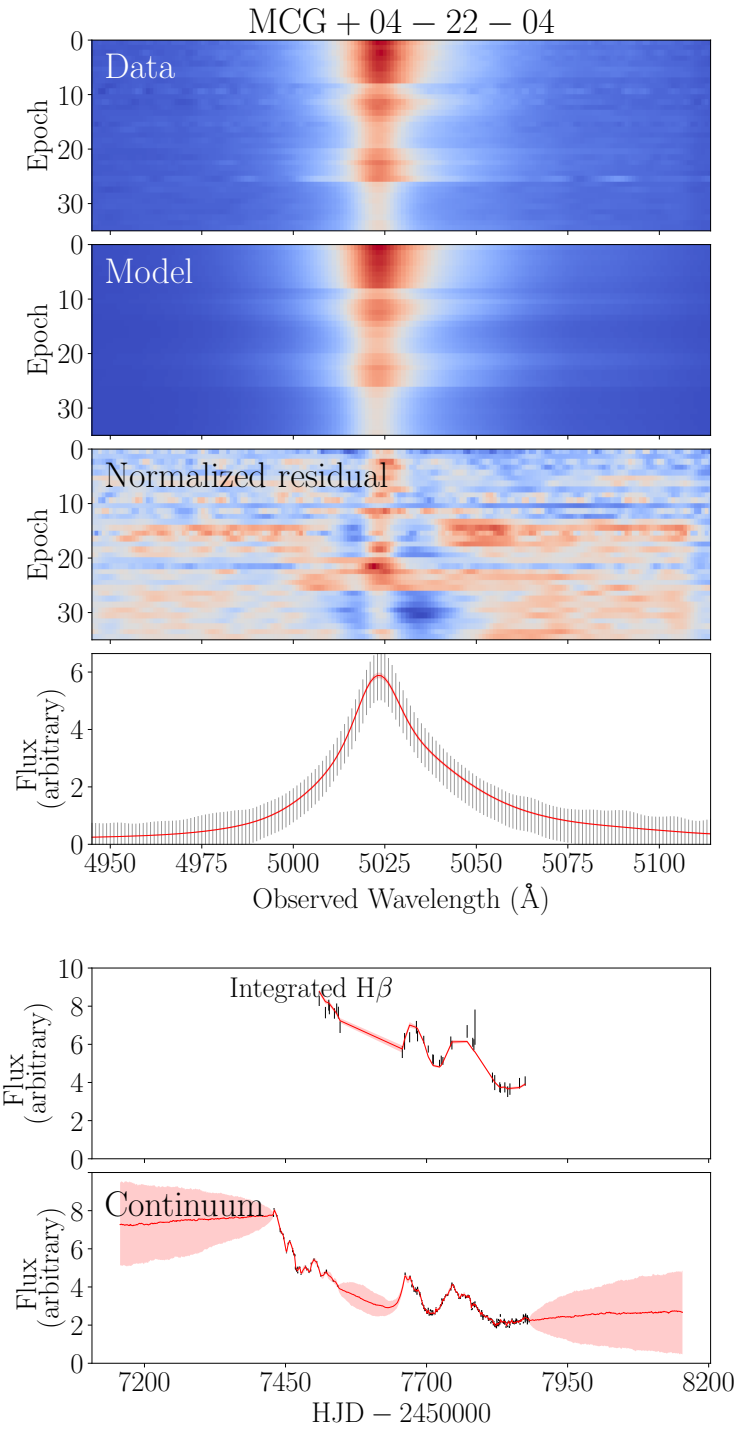

Figure 2.5 Model fits to the Hβ line profile, integrated Hβ flux, and AGN continuum flux for MCG +04-22-042. See the Figure 2.3 caption for panel descriptions.

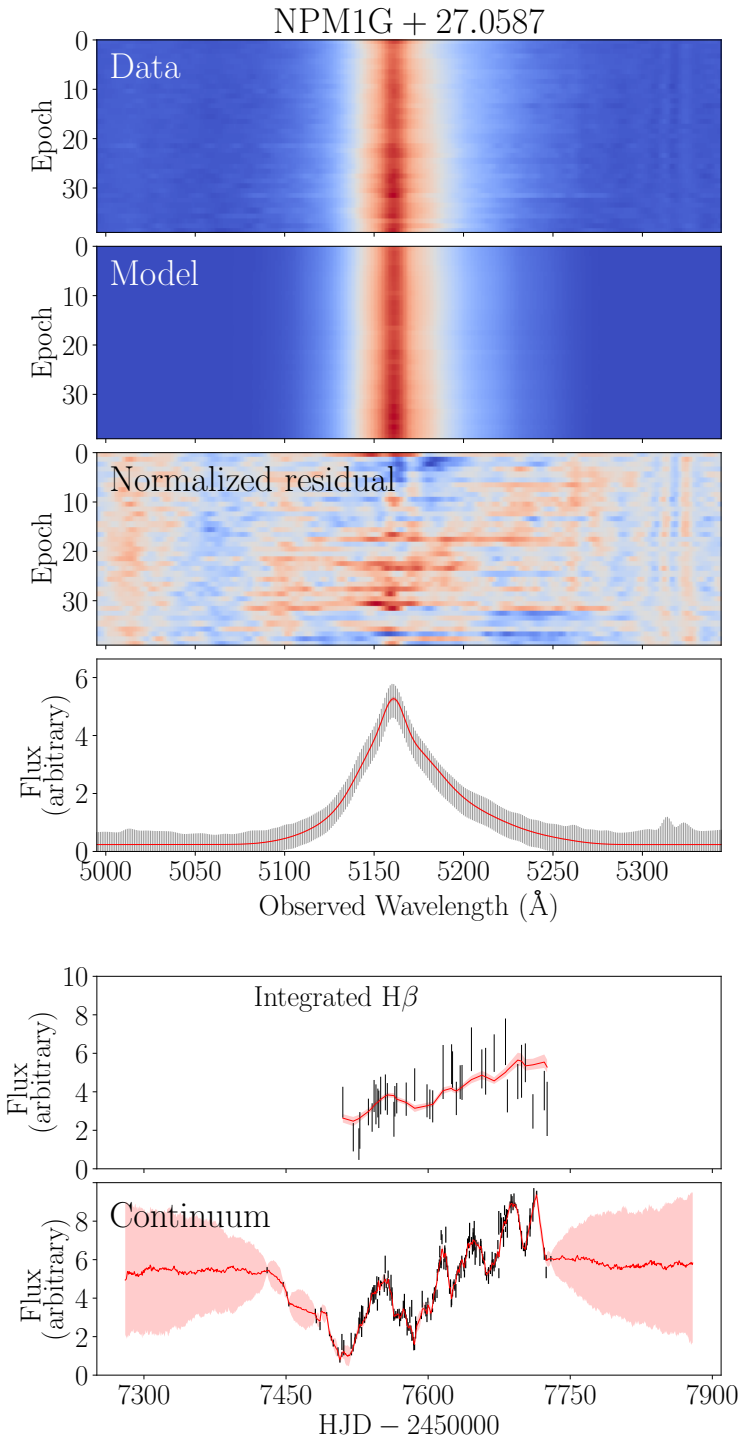

Figure 2.6 Model fits to the Hβ line profile, integrated Hβ flux, and AGN continuum flux for NPM1G+27.0597. See the Figure 2.3 caption for panel descriptions.

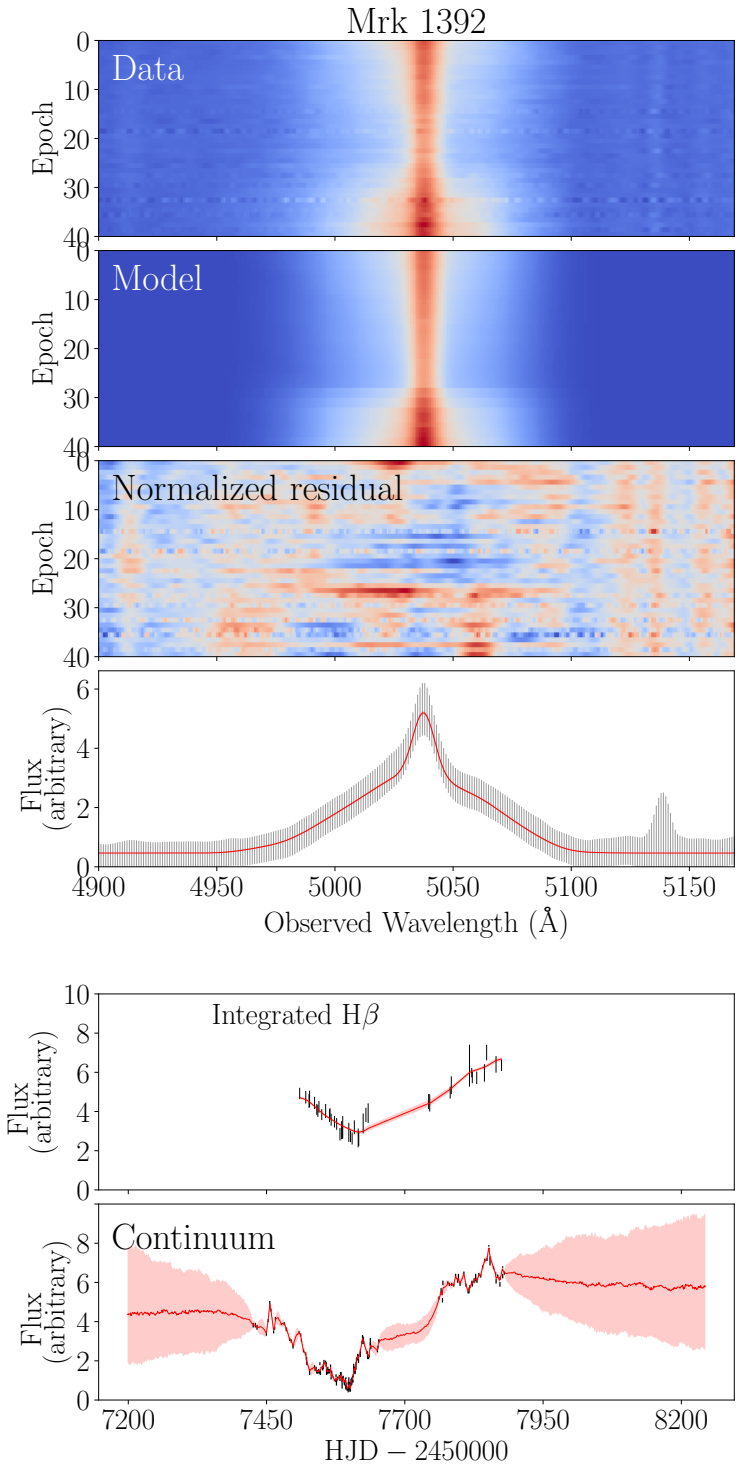

Figure 2.7 Model fits to the Hβ line profile, integrated Hβ flux, and AGN continuum flux for Mrk 1392. See the Figure 2.3 caption for panel descriptions.

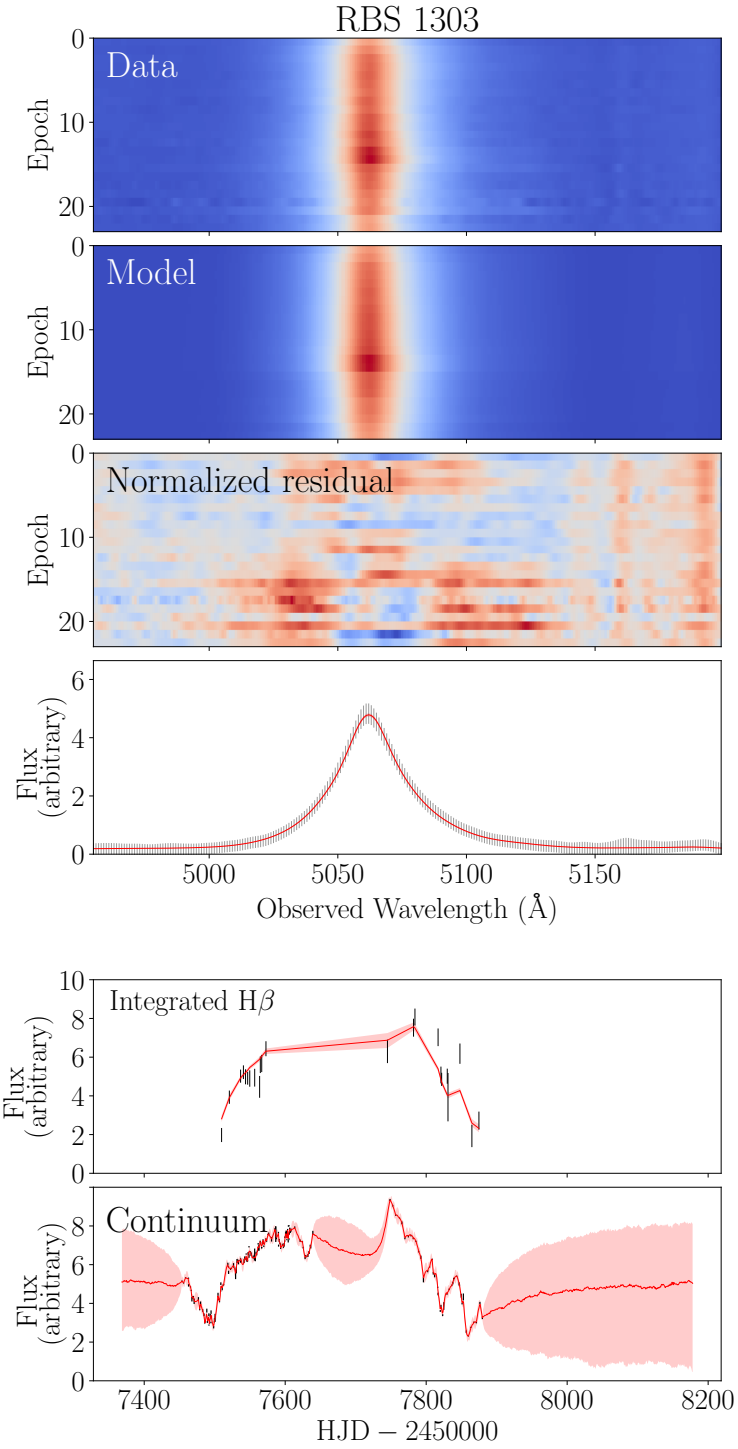

Figure 2.8 Model fits to the Hβ line profile, integrated Hβ flux, and AGN continuum flux for RBS 1303. See the Figure 2.3 caption for panel descriptions.

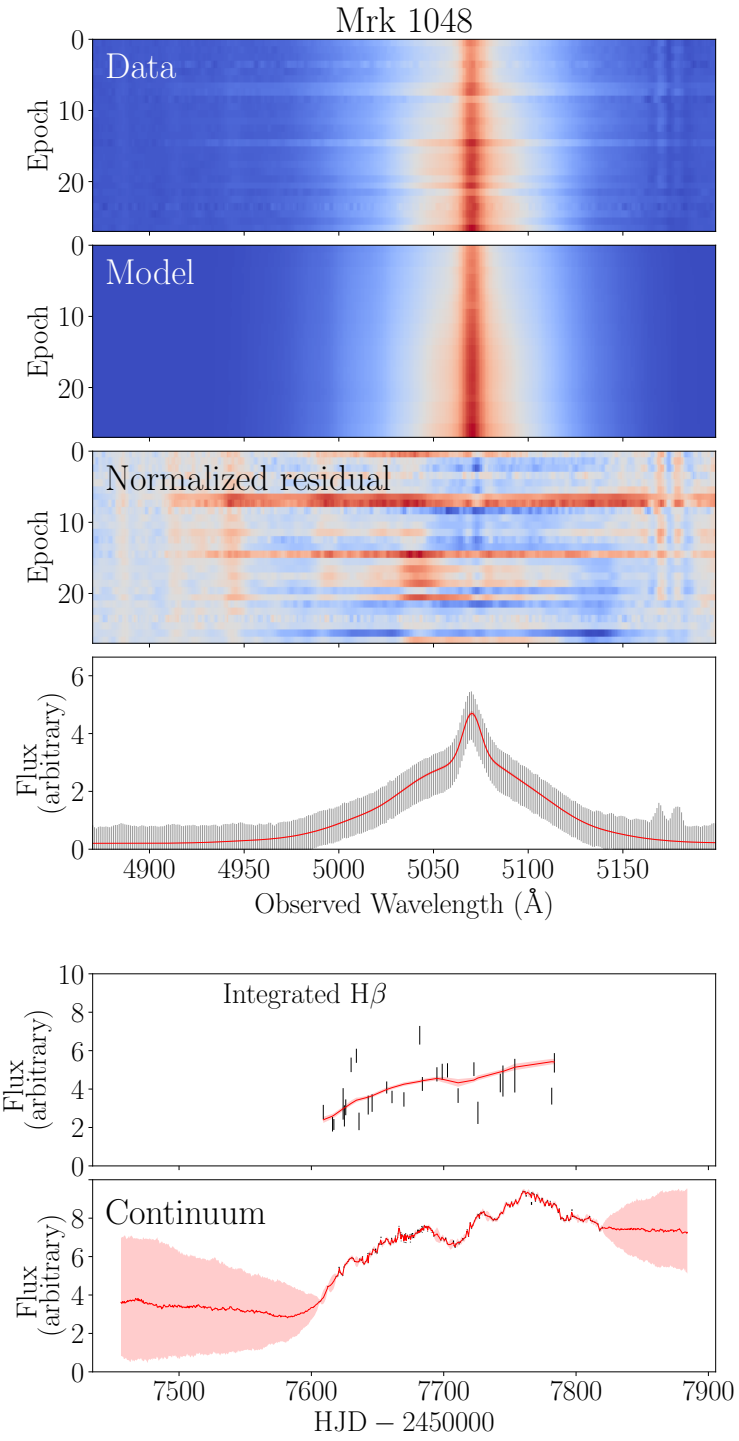

Figure 2.9 Model fits to the Hβ line profile, integrated Hβ flux, and AGN continuum flux for Mrk 1048. See the Figure 2.3 caption for panel descriptions.

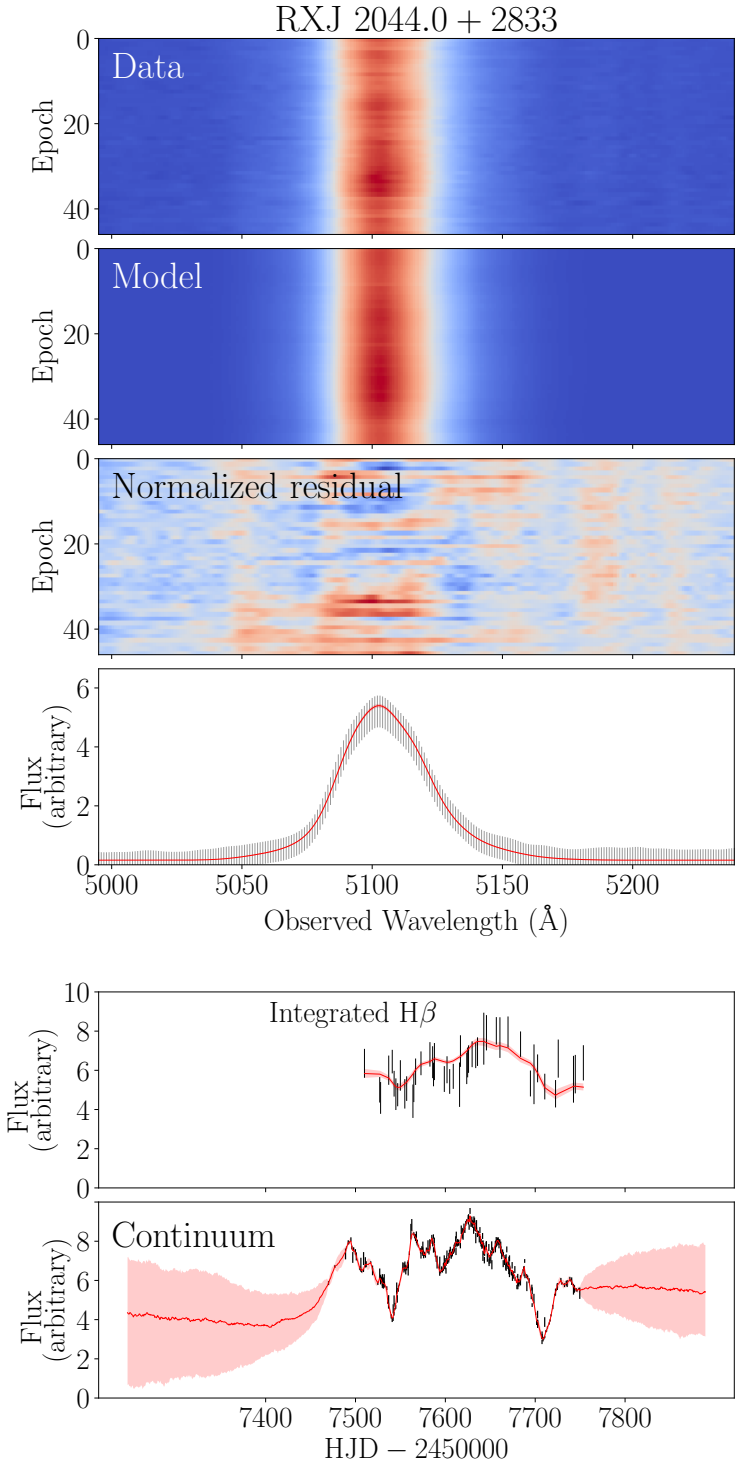

Figure 2.10 Model fits to the Hβ line profile, integrated Hβ flux, and AGN continuum flux for RXJ 2044.0+2833. See the Figure 2.3 caption for panel descriptions.

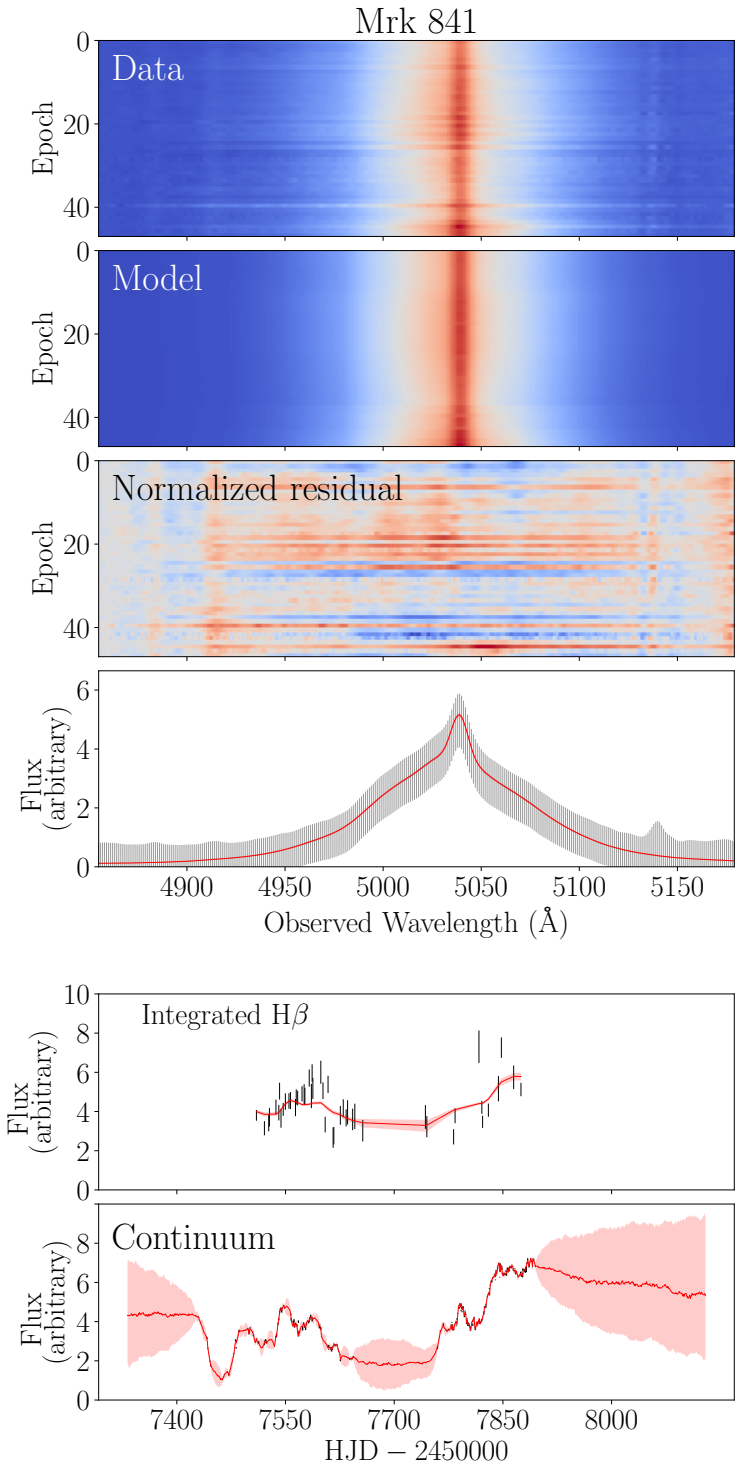

Figure 2.11 Model fits to the Hβ line profile, integrated Hβ flux, and AGN continuum flux for Mrk 841. See the Figure 2.5 caption for panel descriptions.

from a distribution with center rotated $\theta_e = 24^{+23}_{-16}$ degrees from escape velocity toward the circular velocity. Macroturbulent velocities are found to be insignificant with $\sigma_{turb} = 0.01^{+0.05}_{-0.01}$. Finally, we find a black hole mass of $\log_{10}(M_{bh}/M_\odot) = 7.53^{+0.19}_{-0.20}$, which is consistent within our uncertainties with the velocity-resolved reverberation mapping estimate of $\log_{10}(M_{bh}/M_\odot) = 7.46^{+0.1}_{-0.12}$ found by U et al. (2022).

2.3.2 RBS 1917

Geometrically, our model predicts a BLR that is a relatively thick disk ($\theta_o = 25.1^{+9.2}_{-7.5}$ degrees) inclined $\theta_i = 20.2^{+9.9}_{-3.9}$ degrees toward the observer, with a median radius of $r_{median} = 5.0^{+1.3}_{-1.1}$ light-days corresponding to an average time delay of $\tau_{median} = 4.6^{+1.2}_{-1.2}$ light-days. There is a slight preference for preferential Hβ emission from the far side of the BLR (with $\kappa = -0.29^{+0.35}_{-0.14}$) and a transparent BLR midplane ($\xi = 0.68^{+0.25}_{-0.35}$). Our model is unable to constrain, however, whether emission is uniformly emitted or concentrated at the edges ($\gamma = 1.48^{+0.32}_{-0.32}$). Dynamically, 59% of particles remain on circular bounded orbits ($f_{ellip} = 0.59^{+0.14}_{-0.17}$), and the remaining $\sim$ 40% of particles exhibit outflowing ($f_{flow} = 0.59^{+0.28}_{-0.39}$) behavior with velocities rotated $\theta_e = 20^{+21}_{-15}$ degrees from the radial outflowing escape velocity toward a circular velocity. Additionally, the contribution from macroturbulent velocities is small with $\sigma_{turb} = 0.01^{+0.04}_{-0.01}$. Finally, our model estimates a black hole mass of $\log_{10}(M_{bh}/M_\odot) = 7.04^{+0.23}_{-0.35}$, which is consistent within our uncertainties with the velocity-resolved reverberation mapping estimate of $\log_{10}(M_{bh}/M_\odot) = 7.15^{+0.15}_{-0.25}$, found by U et al. (2022).

2.3.3 MCG +04-22-042

We find the Hβ-emitting BLR of MCG +04-22-042 to be best described by a slightly thick disk ($\theta_o = 13.6^{+6.9}_{-4.9}$ degrees) inclined $\theta_i = 11.3^{+5.8}_{-5.0}$ degrees toward the observer and median BLR radius of $r_{\rm median} = 6.24^{+1.01}_{-0.87}$ light-days. Our model finds a preference for concentrated emission at the edges of the BLR ($\gamma = 1.65^{+0.26}_{-0.36}$) but is unable to constrain the transparency

of the BLR midplane ($\xi = 0.43^{+0.35}_{-0.26}$) or whether emission from the far/near side of the BLR is preferred ($\kappa = -0.14^{+0.44}_{-0.27}$). Dynamically, our model finds a preference for 40% of particles having nearly circular orbits ($f_{ellip} = 0.39^{+0.21}_{-0.18}$) with the remaining particles having velocities drawn from a distribution with center rotated $\theta_e = 19^{+20}_{-13}$ degrees from inflowing ($f_{flow} = 0.27^{+0.18}_{-0.19}$) escape velocity toward the circular velocity. The contribution from macroturbulent velocities is small, with $\sigma_{turb} = 0.01^{+0.02}_{-0.00}$. Finally, we find a black hole mass of $\log_{10}(M_{bh}/M_{\odot}) = 7.59^{+0.42}_{-0.28}$, which is consistent within our 1.5σ uncertainty with the U et al. (2022) value of $\log_{10}(M_{bh}/M_{\odot}) = 7.18^{+0.10}_{-0.10}$.

2.3.4 NPM1G+27.0587

The data best fit a moderately thick disk ($\theta_o = 18^{+11}_{-9.1}$) H$\beta$-emitting BLR, viewed at an inclination of $\theta_i = 19^{+11}_{-8.5}$ degrees with a median radius of $r_{median} = 7.2^{+2.8}_{-2.0}$ light-days. Our model finds a preference for an opaque BLR midplane with $\xi = 0.11^{+0.37}_{-0.09}$ but is unable to constrain whether the BLR prefers emission to the far/near side of the BLR ($\kappa = -0.14^{+0.40}_{-0.25}$) or is uniformly emitted/concentrated at the edges ($\gamma = 1.39^{+0.38}_{-0.27}$). Dynamically, our model finds that a little under half of the particles have circular orbits ($f_{ellip} = 0.44^{+0.19}_{-0.18}$). The remaining particles having velocities drawn from a Gaussian $v_r - v_\phi$ distribution rotated $\theta_e = 36^{+35}_{-24}$ degrees from radially inflowing ($f_{flow} = 0.26^{+0.18}_{-0.19}$) escape velocity to circular velocity. The contribution from macroturbulent velocities is small, with $\sigma_{turb} = 0.01^{+0.05}_{-0.01}$. Finally, we estimate a black hole mass of $\log_{10}(M_{bh}/M_{\odot}) = 7.64^{+0.40}_{-0.36}$ that is consistent within 2σ uncertainties of the $\log_{10}(M_{bh}/M_{\odot}) = 7.28^{+0.23}_{-0.43}$ estimate found by U et al. (2022) using a traditional reverberation mapping analysis.

2.3.5 Mrk 1392

The Hβ-emitting BLR of this source is modeled as a thick disk ($\theta_o = 41.2^{+5.3}_{-4.8}$ degrees) inclined $\theta_i = 25.5^{+3.4}_{-2.8}$ degrees toward an observer with a median BLR radius of $r_{median} = 51.6^{+12.2}_{-8.6}$ light-days. The data best fit a mostly opaque BLR midplane with $\xi = 0.25^{+0.28}_{-0.18}$

with slight preferrential emission from the near side of the BLR ($\kappa = 0.26^{+0.18}_{-0.25}$) and mostly isotropic emission ($\gamma = 1.53^{+0.32}_{-0.33}$). Dynamically, our model suggests that $\sim 80\%$ of particles have nearly circular orbits with ($f_{ellip} = 0.81^{+0.04}_{-0.06}$), with the remaining particles having velocities drawn from a Gaussian $v_r - v_\phi$ distribution rotated $\theta_e = 25^{+14}_{-15}$ degrees from radially outflowing ($f_{flow} = 0.74^{+0.18}_{-0.18}$) escape velocity to circular velocity. The contribution from macroturbulent velocities is small, with $\sigma_{turb} = 0.01^{+0.04}_{-0.01}$. Finally, we estimate a black hole mass of $\log_{10}(M_{bh}/M_\odot) = 8.16^{+0.11}_{-0.13}$ that is consistent within $< 3\sigma$ with the estimate found by U et al. (2022) ($\log_{10}(M_{bh}/M_\odot) = 7.80^{+0.06}_{-0.07}$).

2.3.6 RBS 1303

The data is in best agreement with a thick disk BLR ($\theta_o = 34.0^{+8.9}_{-10}$degrees) inclined $\theta_i = 29.1^{+7.7}_{-9.0}$ degrees toward an observer with a median radius of $r_{median} = 10.1^{+1.3}_{-1.2}$ light-days. The model finds a slight preference for a transparent BLR midplane ($\xi = 0.60^{+0.22}_{-0.16}$) and a strong preference for preferential emission from the far side of the BLR ($\kappa = -0.48^{+0.05}_{-0.01}$) and concentrated emission toward the edges of the disk ($\gamma = 1.85^{+0.11}_{-0.21}$). Dynamically, the model suggests $\sim 18\%$ of particles have nearly circular orbits ($f_{ellip} = 0.18^{+0.17}_{-0.11}$), with the remaining particles having velocities drawn from a Gaussian $v_r - v_\phi$ distribution rotated $\theta_e = 8.3^{+8.8}_{-5.8}$ degrees from radially outflowing ($f_{flow} = 0.75^{+0.17}_{-0.19}$) escape velocity to circular velocity. The contribution from macroturbulent velocities is small, with $\sigma_{turb} = 0.01^{+0.02}_{-0.00}$. Finally, we find a black hole mass of $\log_{10}(M_{bh}/M_\odot) = 6.79^{+0.19}_{-0.11}$ that is consistent within 3.2σ of the estimate given by U et al. (2022) ($\log_{10}(M_{bh}/M_\odot) = 7.40^{+0.08}_{-0.14}$).

2.3.7 Mrk 1048

The Hβ BLR emission for this source is best described by a thick disk ($\theta_o = 31^{+14}_{-10.0}$) inclined $\theta_i = 21.5^{+9.4}_{-9.4}$ degrees toward an observer with a median BLR radius of $r_{median} = 11.3^{+7.3}_{-6.2}$ light-days. We find a slight preference for an opaque midplane ($\xi = 0.30^{+0.42}_{-0.20}$) but are unable to constrain whether Hβ emission is isotropic/concentrated at the edges ($\gamma = 1.47^{+0.33}_{-0.32}$) or

whether emission from the far/near side of the BLR is preferred ($\kappa = 0.10^{+0.28}_{-0.38}$). Dynamically, our model suggests $\sim$ 73% of the particles are on circular orbits ($f_{ellip} = 0.73^{+0.09}_{-0.13}$), with the remaining particles having velocities drawn from a Gaussian $v_r - v_\phi$ distribution rotated $\theta_e = 15^{+15}_{-10}$ degrees from radially outflowing ($f_{flow} = 0.74^{+0.18}_{-0.19}$) escape velocity toward circular velocity. The contribution from macroturbulent velocities is small, with $\sigma_{turb} = 0.01^{+0.04}_{-0.01}$. Finally, we estimate a black hole mass of $\log_{10}(M_{bh}/M_\odot) = 7.79^{+0.44}_{-0.48}$that is consistent within 1σ uncertainties of the estimate $\log_{10}(M_{bh}/M_\odot) = 7.38^{+0.34}_{-0.60}$, found by U et al. (2022).

2.3.8 RXJ 2044.0+2833

Geometrically, the BLR is modeled as a thick disk ($\theta_o = 51^{+15}_{-12}$ degrees) inclined $\theta_i = 42.5^{+9.6}_{-8.4}$ degrees toward an observer with a mean BLR radius of $r_{median} = 28.3^{+7.5}_{-5.4}$ light-days. The model finds slight preferences for an opaque BLR midplane ($\xi = 0.17^{+0.28}_{-0.12}$) and preferential emission from the far side of the BLR ($\kappa = -0.20^{+0.33}_{-0.19}$) but is unable to constrain whether Hβ emission is isotropic/concentrated at the edges ($\gamma = 1.37^{+0.44}_{-0.29}$). Dynamically, the model suggests that a little under half ($f_{ellip} = 0.41^{+0.32}_{-0.29}$) of particles have nearly circular orbits, with the remaining particles having velocities drawn from a Gaussian $v_r - v_\phi$ distribution rotated $\theta_e = 34^{+32}_{-21}$ degrees from radially inflowing ($f_{flow} = 0.22^{+0.19}_{-0.15}$) escape velocity to circular velocity. The contribution from macroturbulent velocities is small, with $\sigma_{turb} = 0.01^{+0.03}_{-0.01}$. Finally, we find a black hole mass of $\log_{10}(M_{bh}/M_\odot) = 7.09^{+0.17}_{-0.17}$ that is consistent with the estimate of $\log_{10}(M_{bh}/M_\odot) = 7.08^{+0.07}_{-0.08}$, found by U et al. (2022).

2.3.9 Mrk 841

Our model indicates that the Hβ BLR emission is best described by a very thick disk ($\theta_o = 41^{+11}_{-11}$ degrees) inclined $\theta_i = 30^{+11}_{-15}$ degrees toward an observer with a median BLR radius of $r_{median} = 10.6^{+5.6}_{-3.4}$ light-days. The data prefer preferential emission from the far side of the BLR ($\kappa = -0.23^{+0.43}_{-0.14}$) and slightly prefer a mostly transparent midplane ($\xi = 0.68^{+0.23}_{-0.41}$). Our model is unable to constrain, however, whether emission isotropic/concentrated at the edges

($\gamma = 1.41^{+0.42}_{-0.29}$). Dynamically, our model suggests that $\sim 33\%$ of particles are on circular orbits ($f_{ellip} = 0.33^{+0.24}_{-0.22}$), with the remaining particles having velocities drawn from a Gaussian $v_r - v_\phi$ distribution rotated $\theta_e = 51^{+20}_{-27}$ degrees from radially inflowing ($f_{flow} = 0.45^{+0.36}_{-0.29}$) escape velocity to circular velocity. The contribution from macroturbulent velocities is small, with $\sigma_{turb} = 0.01^{+0.05}_{-0.01}$. Finally, we estimate a black hole mass of $\log_{10}(M_{bh}/M_\odot) = 7.62^{+0.50}_{-0.30}$ that is consistent with the estimate $\log_{10}(M_{bh}/M_\odot) = 7.66^{+0.20}_{-0.21}$ found by U et al. (2022).

2.4 Discussion

Here we highlight our phenomenological model's capability to directly constrain the BLR kinematics that best fit the data. We compare our model's interpretations with those found by U et al. (2022) using traditional qualitative velocity-delay map interpretations. We then combine our results with those from previous studies and search for any luminosity-dependent trends or a line profile shape dependence on BLR structure and kinematics, to try to gain a better understanding of the Hβ-emitting BLR.

2.4.1 Inferred CARAMEL Kinematics Compared to Velocity-Delay Map Results

Overall, we find that roughly half of the sources in this work have interpretations consistent with those suggested by U et al. (2022). In agreement with U et al. (2022), we find infalling behavior ($f_{flow} < 0.5$) in Mrk 841, RXJ 2044.0+2833, NPM1G+27.0587, and Mrk 1048, and outflowing ($f_{flow} > 0.5$) behavior in RBS 1303 and RBS 1917. For the two sources which were interpreted to exhibit symmetric behavior (MCG +04-22-042 and Mrk 1392), our model allows for a more detailed analysis and finds a small fraction of particles exhibit outflowing behavior in Mrk 1392 and a small fraction of particles in MCG +04-22-042 exhibiting inflowing behavior. We now focus on PG 2209+184, whose flat velocity-resolved structures were difficult to describe with simple models. This in turn made it difficult to constrain the Hβ BLR kinematics (U et al., 2022) using traditional reverberation mapping techniques. We present the recovered transfer functions for the remaining eight sources in Figures 2.13–2.20.

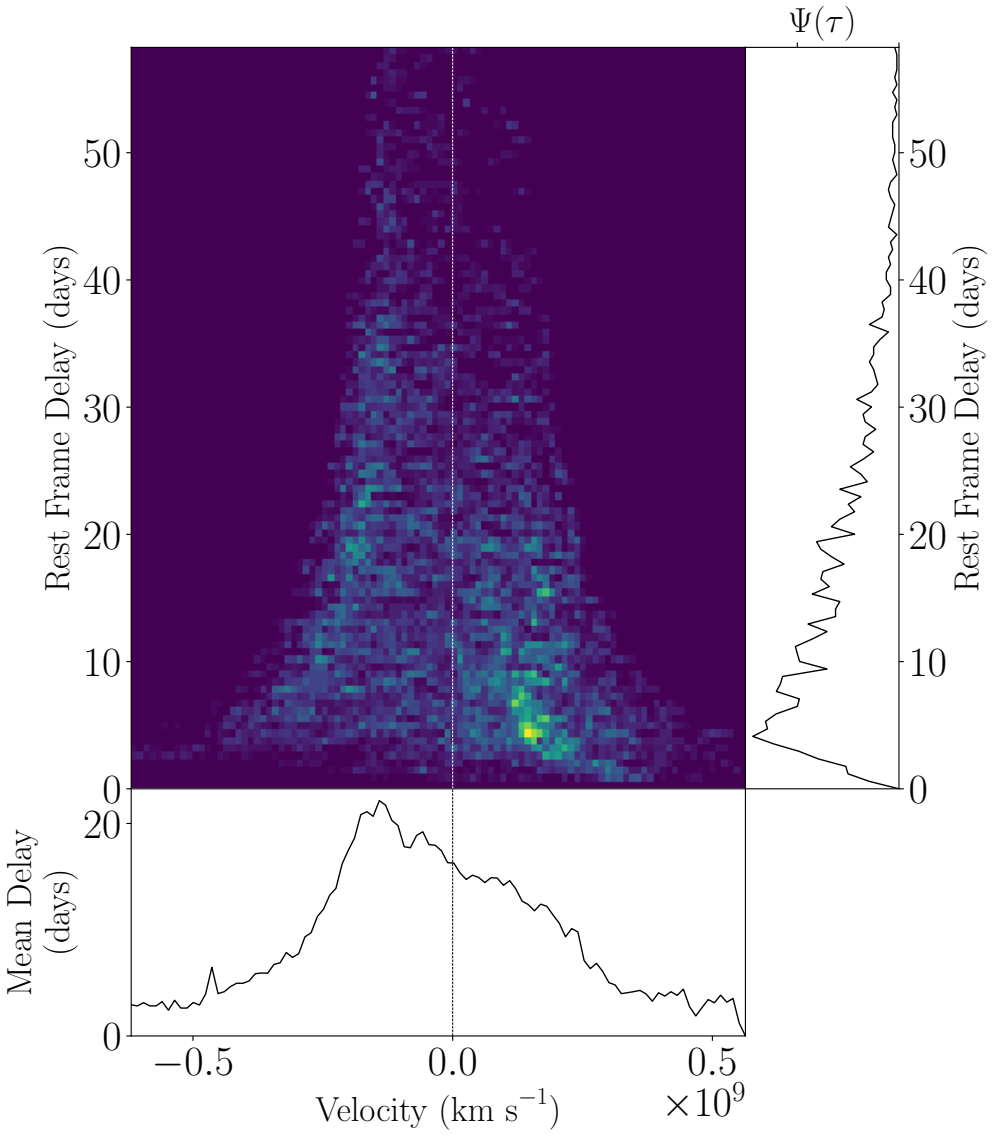

Figure 2.12 PG 2209+184 transfer function produced using median model parameter estimates. See Figure 2.13 caption for panel descriptions.

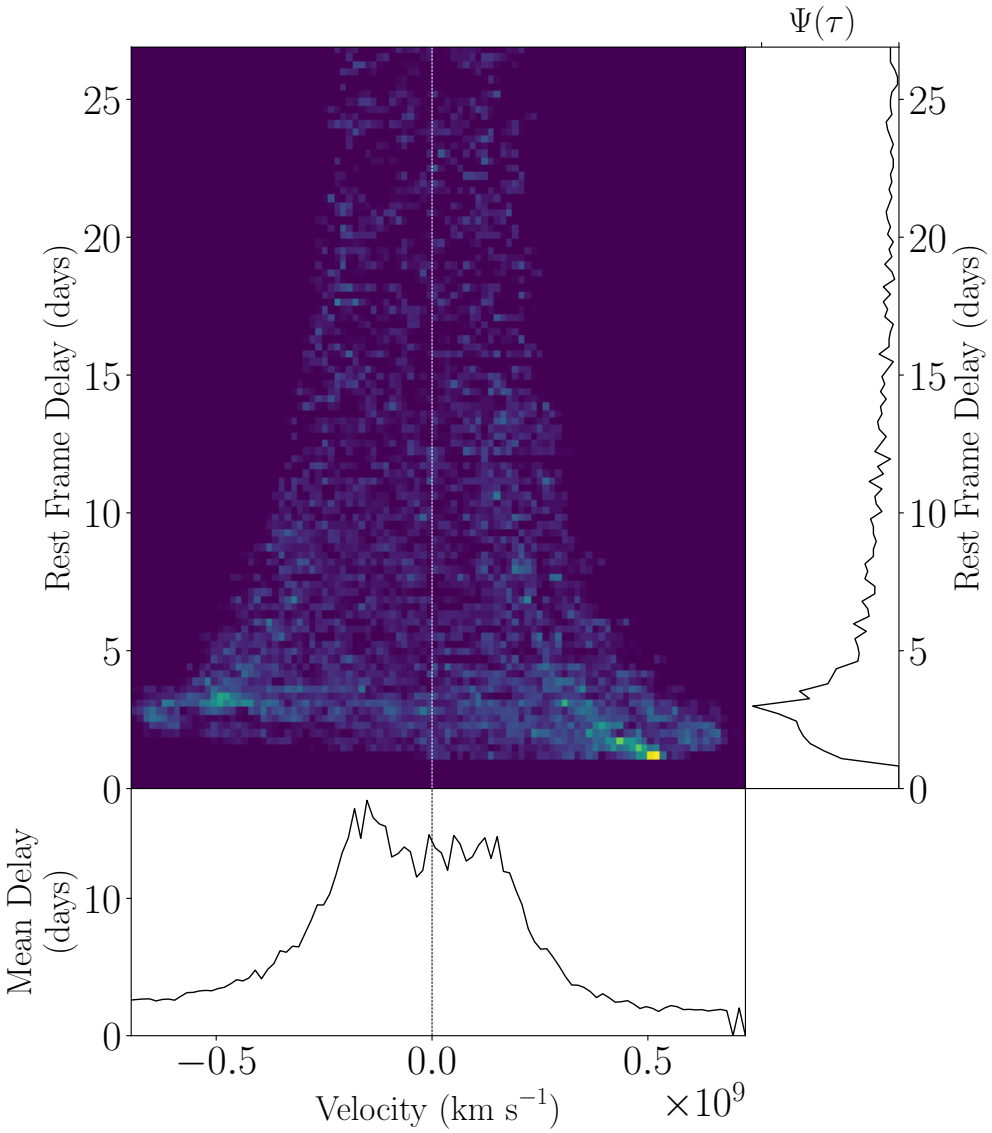

Figure 2.13 NPM1G+27.0587 transfer function produced using median model parameter estimates. The right-hand panel shows the velocity-integrated transfer function and the bottom panel shows the average time lag for each velocity pixel.

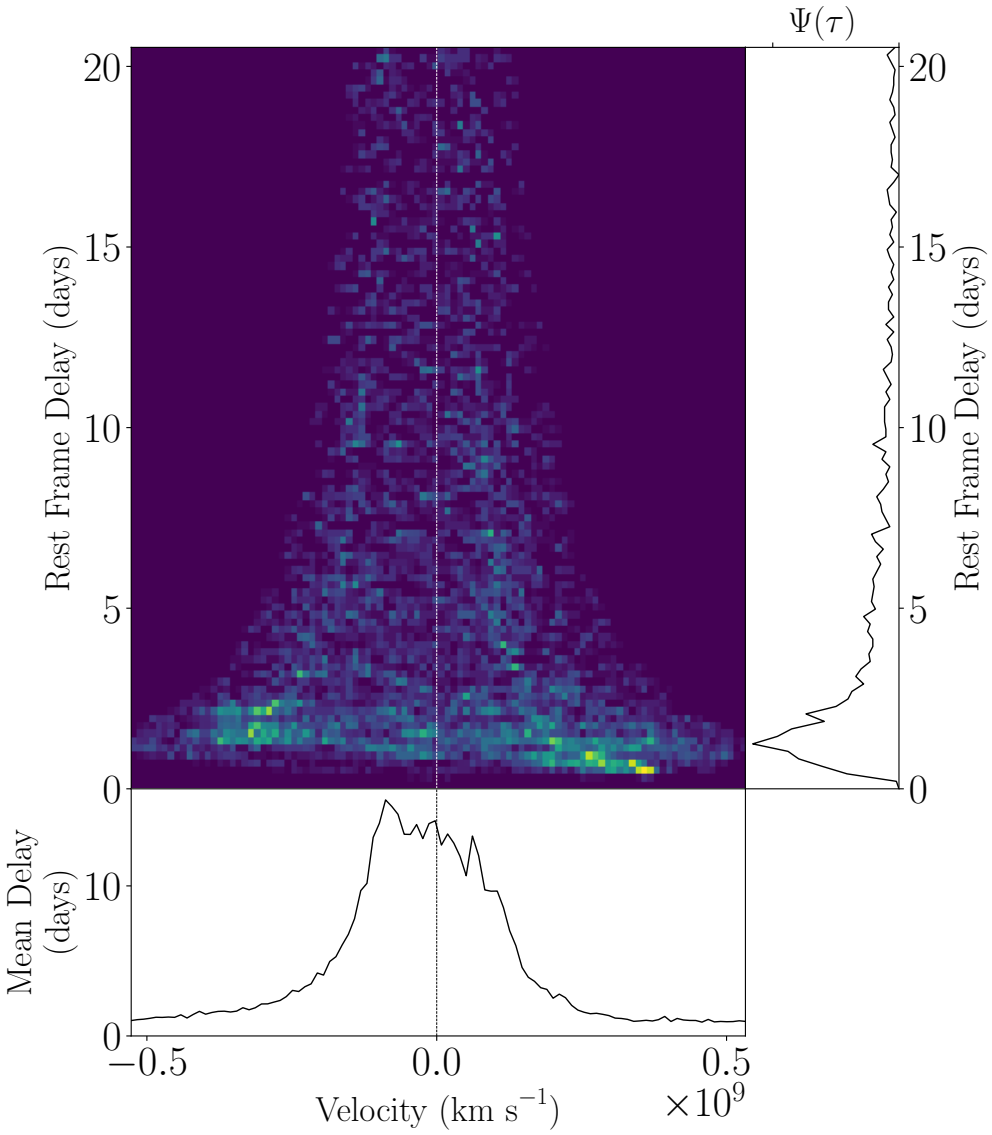

Figure 2.14 RBS 1917 transfer function produced using median model parameter estimates. See Figure 2.13 caption for panel descriptions.

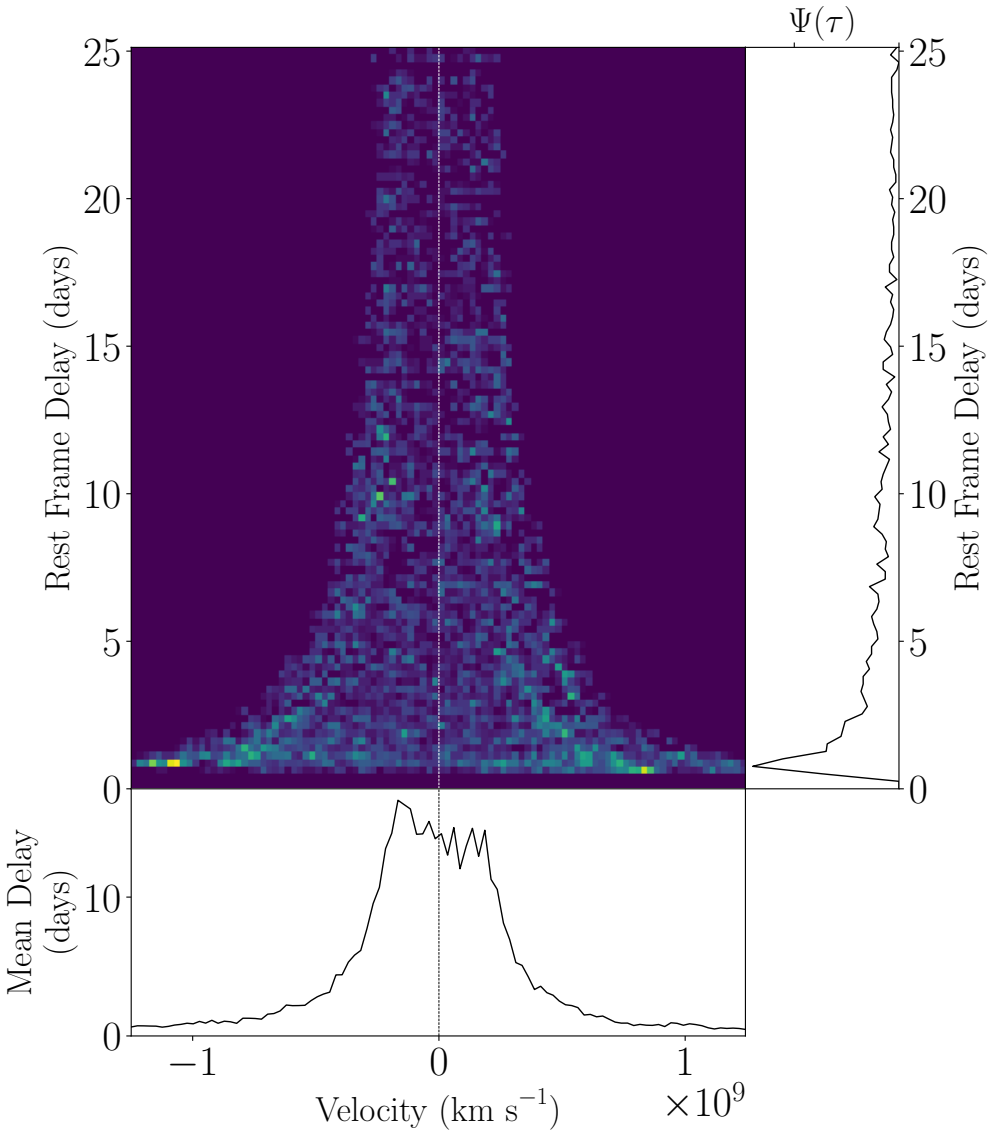

Figure 2.15 MCG +04-22-042 transfer function produced using median model parameter estimates. See Figure 2.13 caption for panel descriptions.

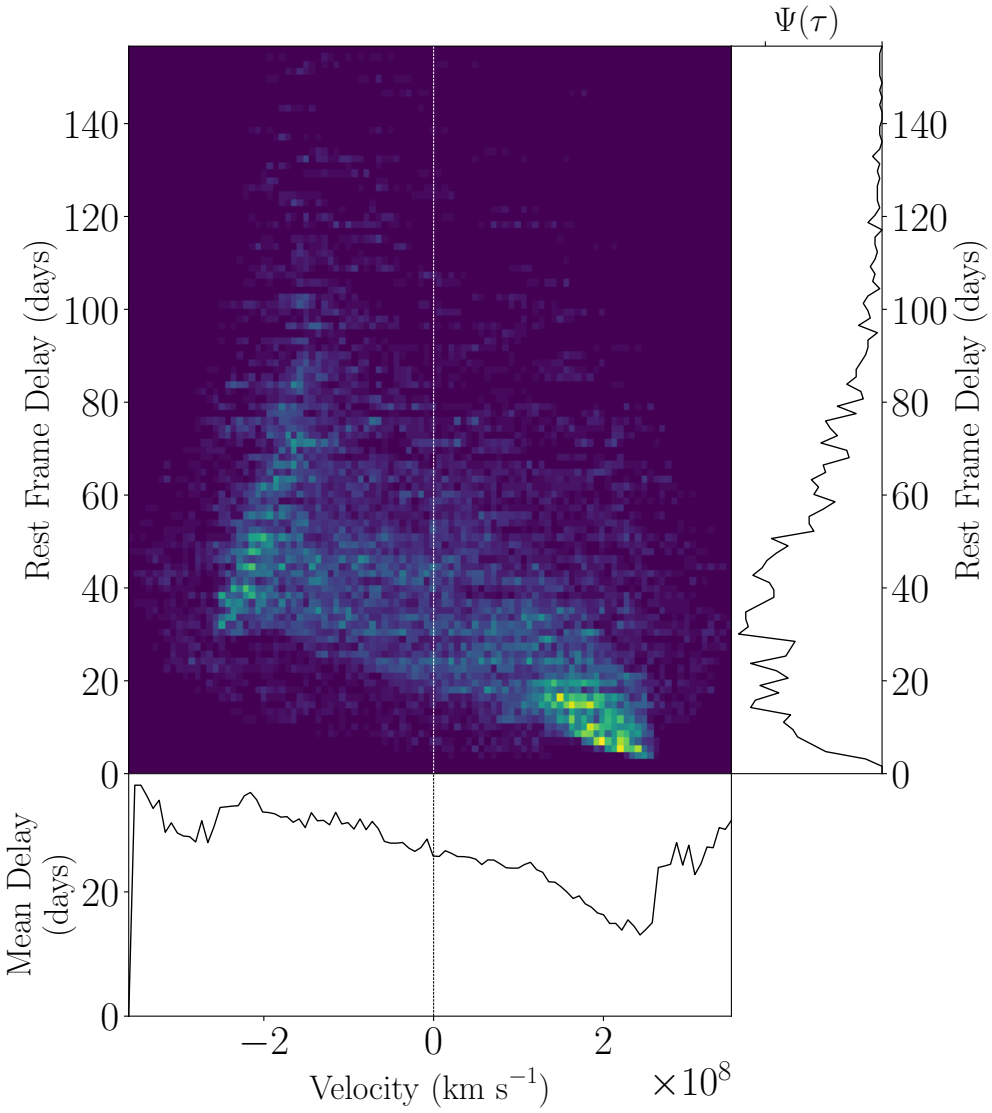

Figure 2.16 Mrk 1392 transfer function produced using median model parameter estimates. See Figure 2.13 caption for panel descriptions.

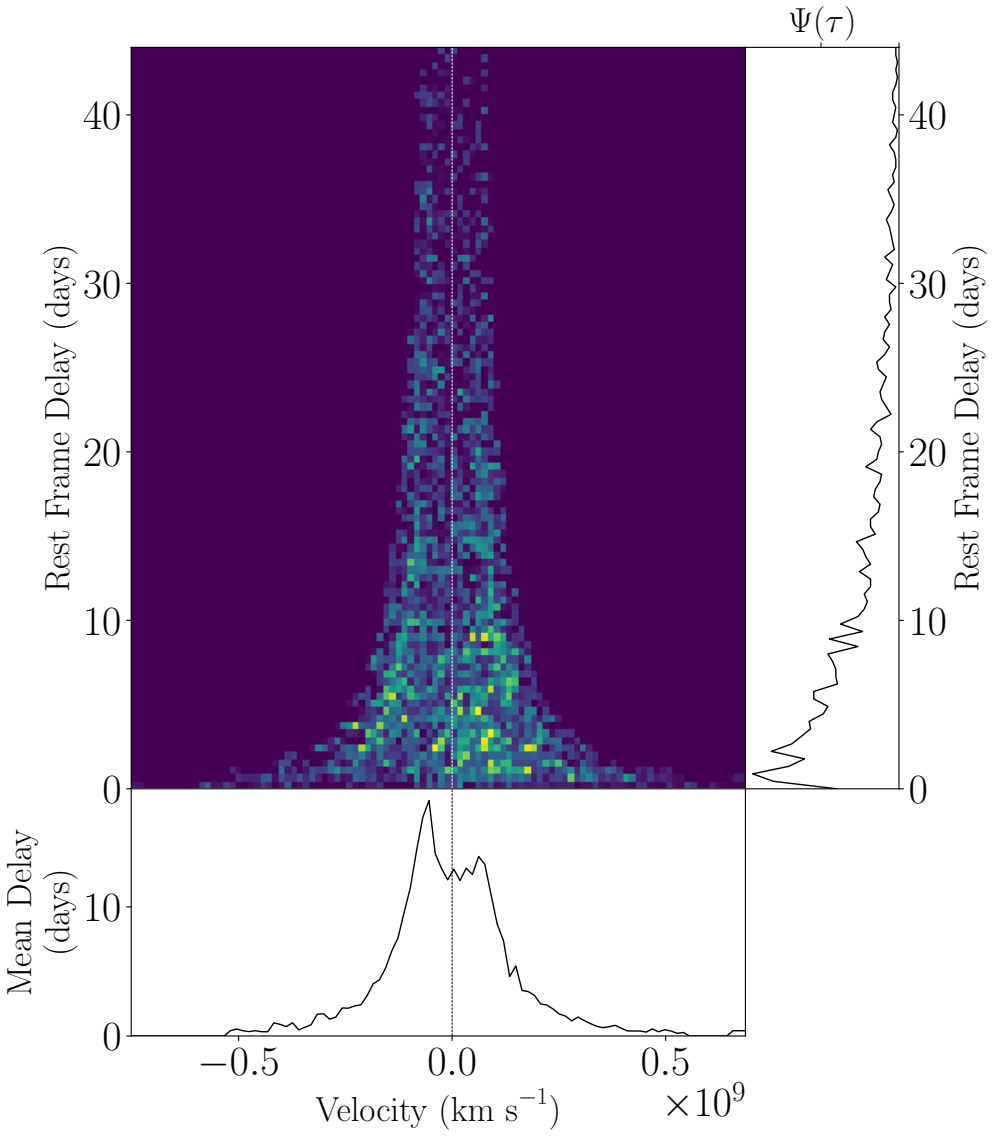

Figure 2.17 RBS 1303 transfer function produced using median model parameter estimates. See Figure 2.13 caption for panel descriptions.

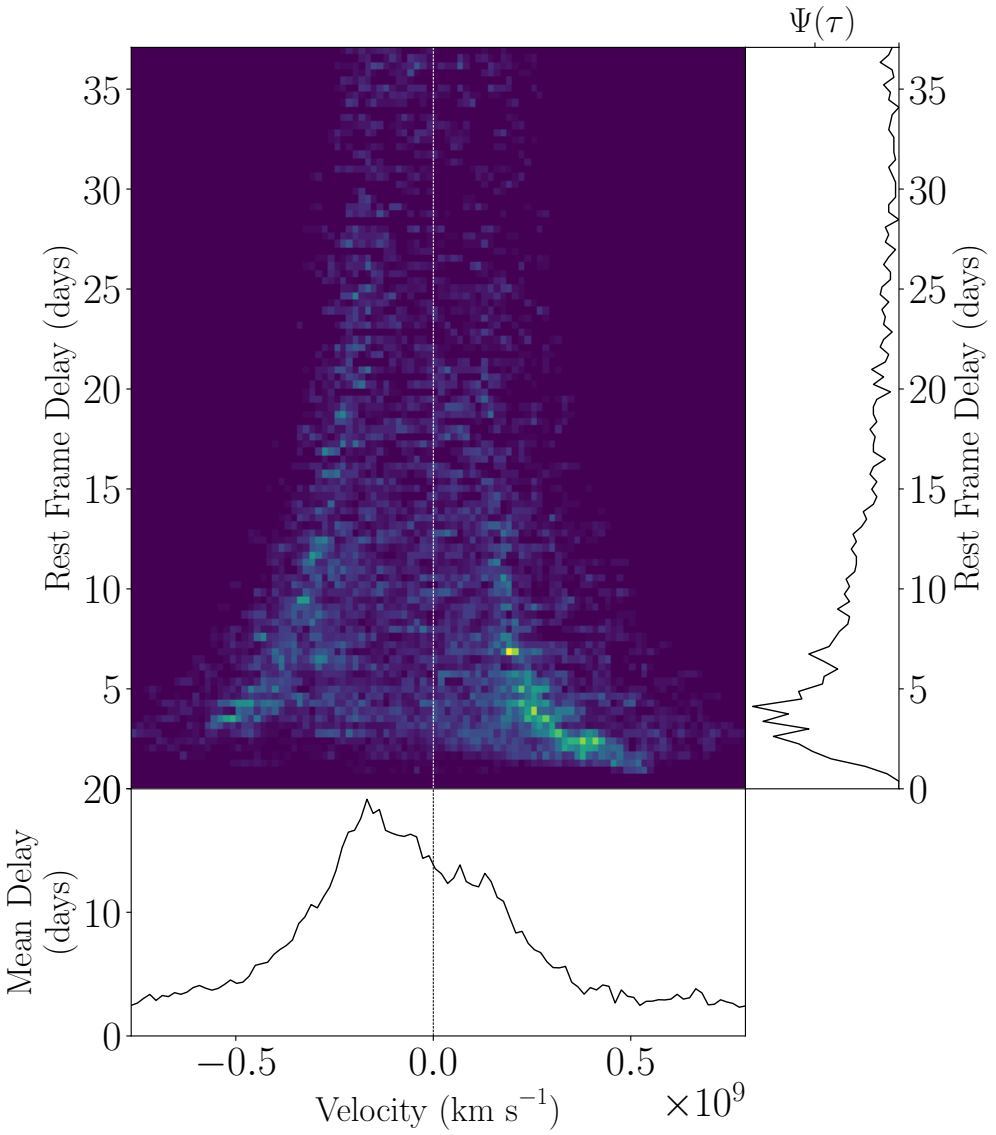

Figure 2.18 Mrk 1048 transfer function produced using median model parameter estimates. See Figure 2.13 caption for panel descriptions.

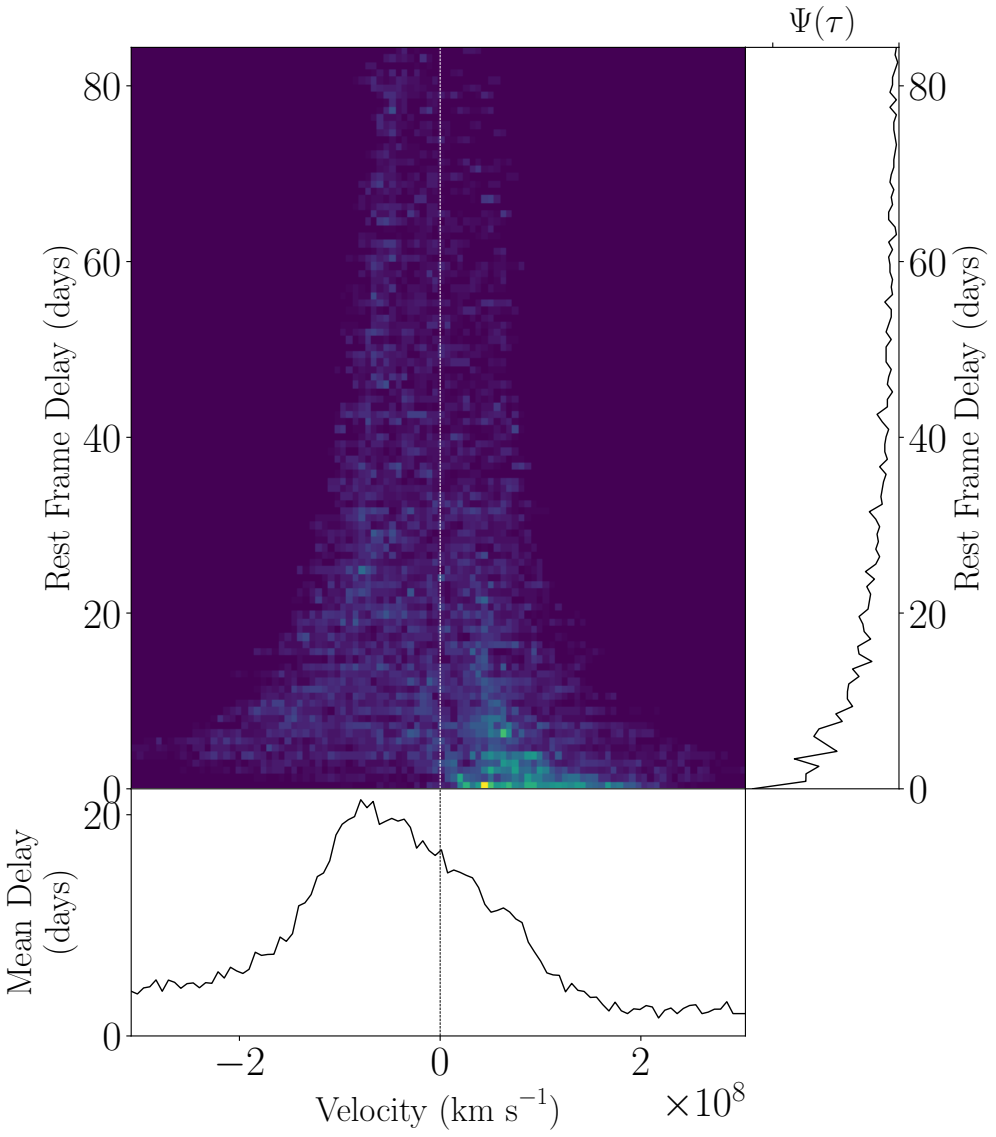

Figure 2.19 RXJ 2044.0+2833 transfer function produced using median model parameter estimates. See Figure 2.13 caption for panel descriptions.

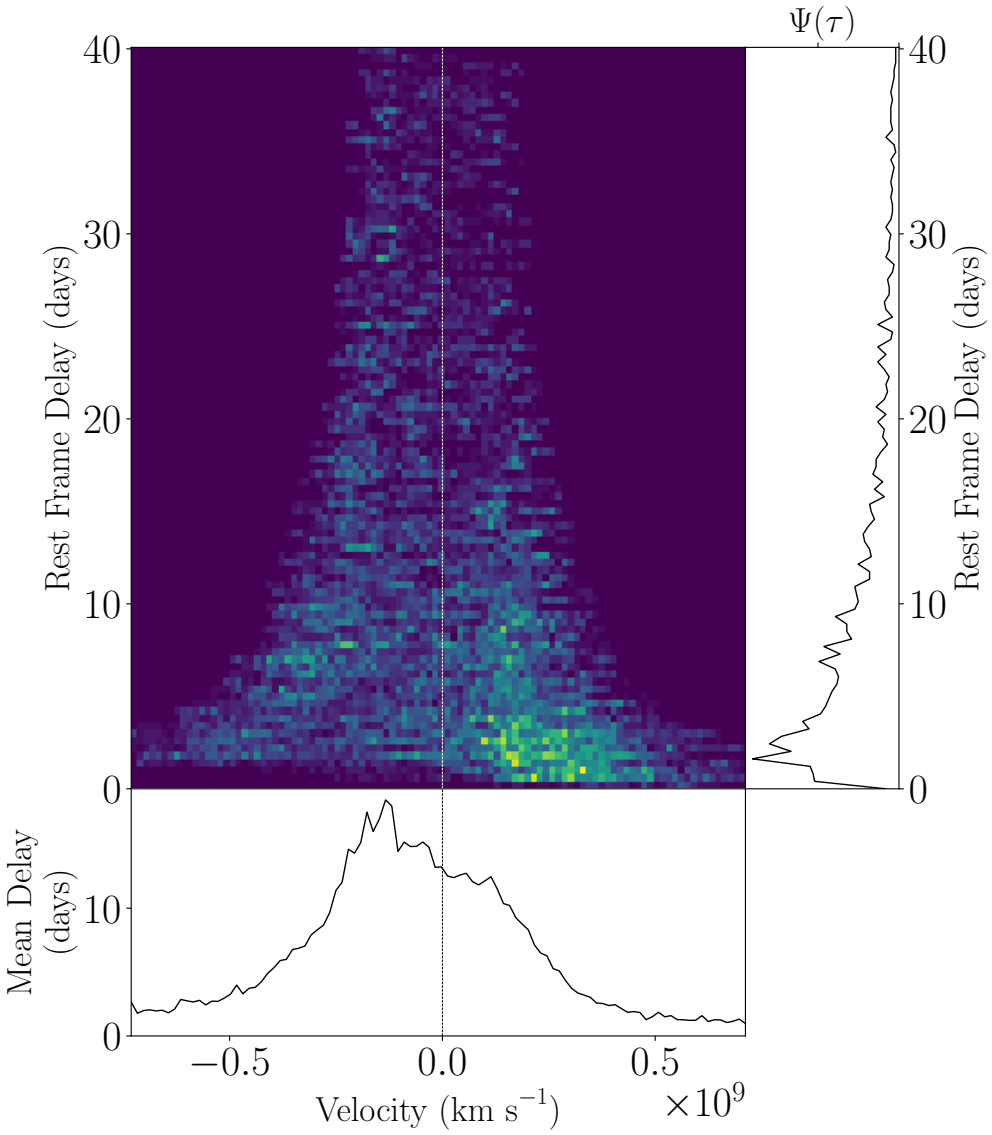

Figure 2.20 Mrk 841 transfer function produced using median model parameter estimates. See Figure 2.13 caption for panel descriptions.

The transfer function constructed for PG 2209+184 using CARAMEL median value model parameters that best fit the data is found in Figure 2.12. Our model suggests that $\sim 54\%$ of particles have nearly circular orbits ($f_{ellip} = 0.54^{+0.10}_{-0.15}$), with the remaining particles having velocities drawn from a Gaussian $v_r - v_\phi$ distribution rotated $\theta_e = 24^{+23}_{-16}$ degrees from radially inflowing (f_{flow}=$0.24^{+0.17}_{-0.16}$) escape velocity toward circular velocity. This can be summarized with the In.$-$Out. parameter defined by W18, with a value of $-0.40^{+0.09}_{-0.09}$, suggesting that a majority of the remaining $(1 - f_{ellip}) \approx 46\%$ particles exhibit radial inflow behavior.

Our result emphasizes the qualitative interpretation of transfer functions, as the transfer function depicted in Figure 2.13 could easily be interpreted as symmetric, which is consistent with Keplerian, disk-like rotation or random motion without any net radial inflow or outflow across the extended BLR. It appears that the asymmetric pattern associated with radial infalling gas is much more subtle and the slightly longer lags on the blue wing near zero velocity may not immediately be interpreted as radial infalling gas, since the asymmetry is not seen in the high-velocity component of the blue wing. (i.e., the slight top-hat profile shape is only slightly asymmetric from the center on the blue side). This example again emphasizes the difficulty in interpreting qualitatively the information embedded in velocity-resolved velocity delay maps and highlights a benefit of our quantitative forward modelling approach.

2.4.2 Luminosity-Dependent Trends

Prior reverberation mapping studies searched for potential patterns in the velocity fields of the ionized Hβ-emitting regions. Using inferred kinematics from velocity-delay maps, Du et al. (2016) investigated whether any trends existed for super-Eddington accreting AGNs, since their stronger radiation pressure could induce pressure-driven winds and BLR outflow. With a small sample size, Du et al. (2016) concluded that BLR kinematics were diverse for super-Eddington accretion rate AGNs.

Although a similar trend seemed apparent with the modeled sources of the LAMP 2016 sample (as seen in the diversity of kinematics in Figure 2.2), we increase the statistical power of our investigation by combining our sample with those from P14, G17, W18, W20, and B21. In particular, we search for correlations between BLR inclination, opening angle (disk thickness), and kinematics (outflow/inflow/symmetric behavior) with luminosity. We expect such trends to arise for example as a result of radiation pressure driven winds or by variation due to overall accretion rate.

We use both optical luminosity at 5100 Å and the Eddington ratio.[2] The linear regression results are plotted in Figure 2.21 and the regression fit values are found in Table 2.3. With our combined sample, we do not find any significant luminosity-dependent trends; we do not find higher accretion rates to correlate with BLR outflow behavior and come to the same conclusion as Du et al. (2015), that AGNs have diverse BLR geometry and kinematics. A possible interpretation of this diversity is that BLR geometry and kinematics experience "weather-like" changes and cycle through a range of states on timescales of order a year or less (see, e.g., De Rosa et al., 2015; Pancoast et al., 2018; Kara et al., 2021).

2.4.3 Line Profile Shape Dependence on BLR Structure and Kinematics

As suggested by Collin et al. (2006a), the ratio of the full width at half-maximum intensity (FWHM) of the line to the dispersion σ_{line} (i.e., the second moment of the line) may serve as a tracer for the physical parameters of the inner regions of an AGN. Since we expect BLR structure and dynamics to play a role in determining the line-profile shape, we might also expect to find correlations with AGN/BLR parameters.

For reference, $\log_{10}(FWHM/\sigma) \approx 0.37$ corresponds to a Gaussian-shaped line profile. Greater values correspond to a flat-topped shape while values less than 0.37 correspond

[2]We use a bolometric correction factor of nine, but would like to note that this only serves as a rough approximation and the actual bolometric correction factor may depend on Eddington ratio or other parameters.

Table 2.3. Linear regression results for luminosity dependent trends

Luminosity		θ_o $(deg.)$	θ_i $(deg.)$	$In. - Out.$
$\log_{10}(L_{5100}/10^{43}\ erg\ s^{-1})$	α	28.1 ± 2.9	23.9 ± 2.2	-0.02 ± 0.13
	β	3.04 ± 4.7	2.3 ± 3.5	-0.15 ± 0.2
	σ_{int}	10 ± 56	6.9 ± 34	0.59 ± 0.13
$\log_{10}(L_{bol}/L_{Edd})$	α	34.0 ± 7.8	28.7 ± 5.9	-0.33 ± 0.34
	β	4.0 ± 5.4	3.2 ± 4.1	-0.2 ± 0.24
	σ_{int}	10 ± 53	7 ± 30	0.57 ± 0.12

Note. — Linear regression results for optical L_{5100} luminosity and Eddington ratio vs. BLR parameters using both the mean and rms spectrum. The parameter α represents the constant in the regression and β represents the slope of the regression, while σ_{int} represents the standard deviation of the intrinsic scatter. The corresponding relationship is therefore given by $parameter = \alpha + \beta \times \log_{10}(luminosity) + \mathcal{N}(0, \sigma_{int})$.

to a narrower line profile shape with extended wings similar to a Lorentzian profile. We search for correlations between the line-profile shape with the following parameters: black hole mass $\log_{10}(M_{bh}/M_{\odot})$, BLR inclination angle θ_i, BLR opening angle, i.e. disk thickness, θ_o, and Eddington ratio L_{bol}/L_{Edd}, using both the mean and root-mean-square (rms) spectrum. The linear regression results are shown in Figure 2.22 with corresponding values found in Table 2.4.

Although there appears to be an apparent correlation with black hole mass, using the levels of confidence we have defined in Section 2.2.3, we do not find it to be significant. A correlation with black hole mass would be expected if the size of the black hole somehow plays a role in the BLR structure and kinematics. Given the apparent correlation (see left most panels in Figure 2.22), a larger sample size with future studies may help further investigate the existence of such a correlation.

A correlation betweeen line-profile shape given by $\log(FWHM/\sigma)$ and BLR inclination has been suggested in the past by Collin et al. (2006a) and Goad et al. (2012), but has been difficult to confirm since BLR inclination is generally not a direct observable. It is worth

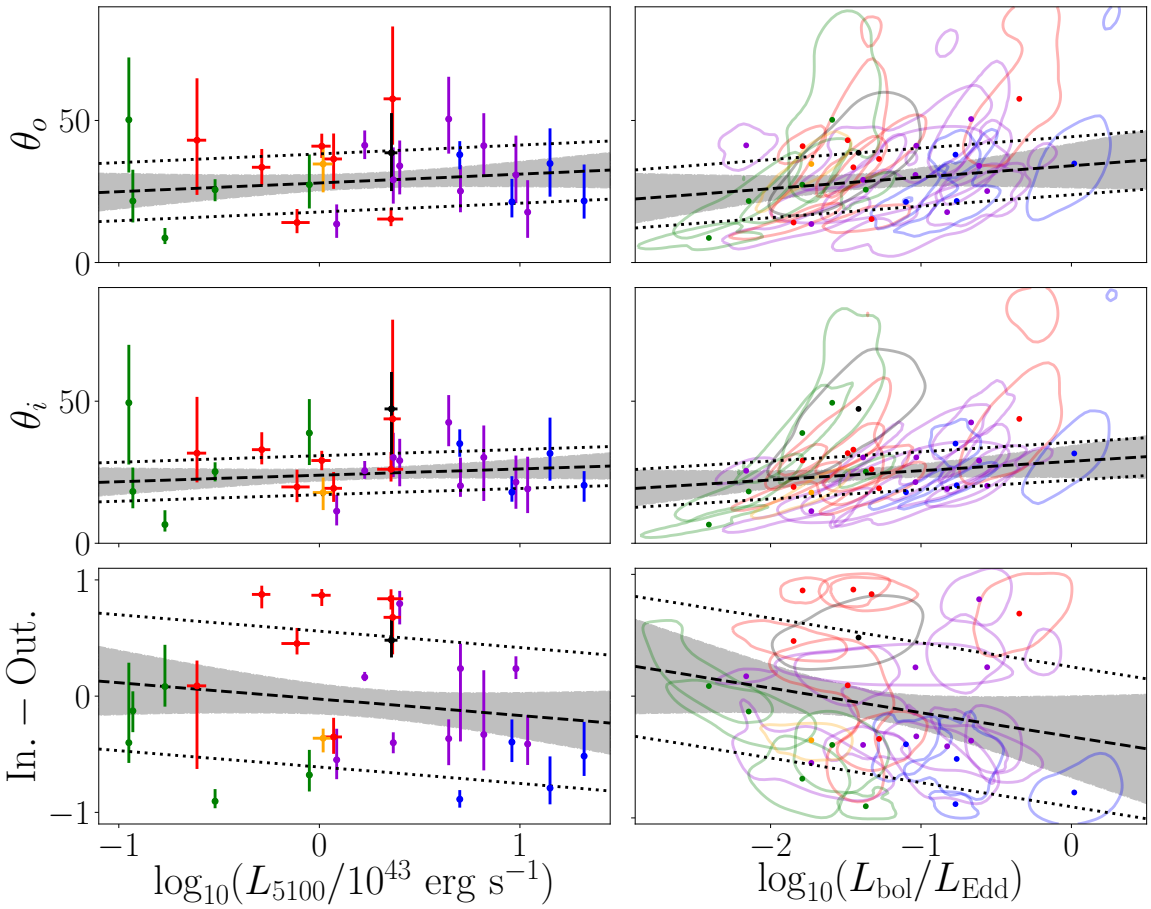

Figure 2.21 Left panels: Correlations between L_{5100} luminosity and select BLR model parameters. Right panels: Correlations between Eddington ratio and select BLR model parameters. The colored dots and contours show the median and 68% confidence regions of the two-dimensional posterior probability distribution functions for each AGN. When the abscissa uncertainty is unavailable, the one-dimensional 68% confidence interval is shown. The dashed black lines and gray shaded regions give the median and 68% confidence intervals of the linear regression. Dotted lines are offset above and below the dashed line by the median value of the intrinsic scatter. Purple points are for the AGNs in this paper, red points are from W18, green points are from P14, blue points are from G17, the black point is from W20, and the orange point is from B21.

noting prior BLR-radio jet inclination studies in which orientation of the radio jet has been shown to be linked to the BLR (e.g., Jorstad et al., 2005; Agudo et al., 2012), however, these measurements are limited and do not exist for the entire sample of reverberation mapped

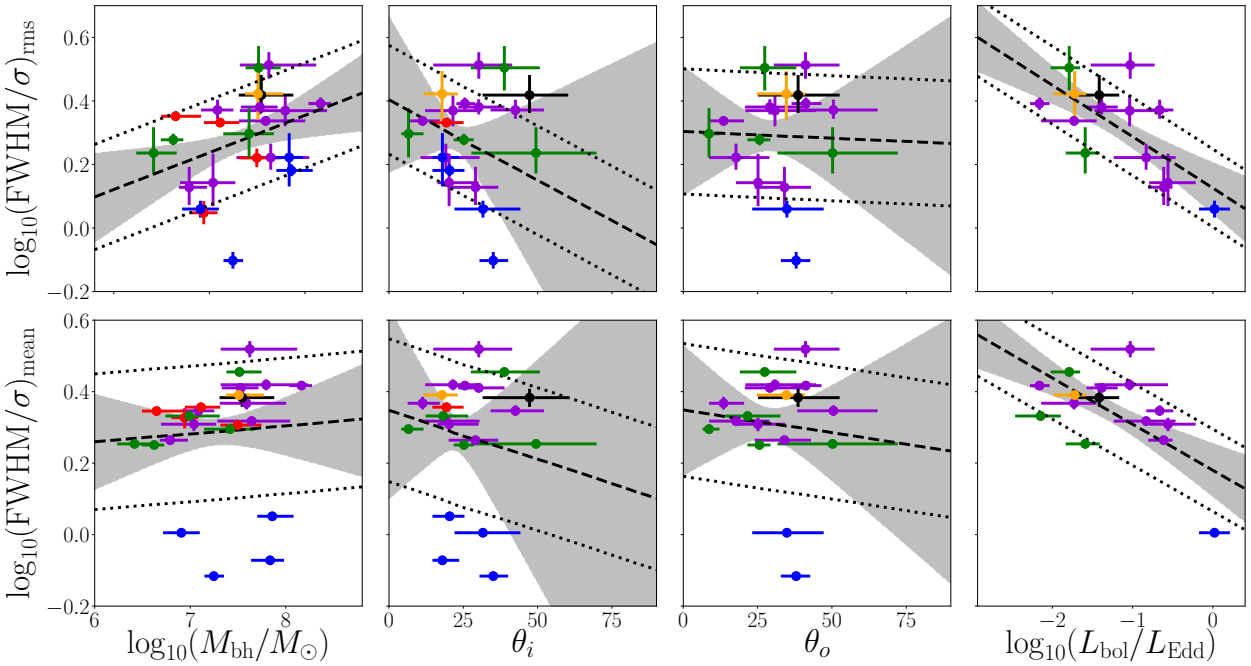

Figure 2.22 Correlations between line-profile shape and black hole mass, BLR inclination angle, opening angle (disk thickness), and Eddington ratio. Top and bottom panels show line-profile shape determined using the mean and rms spectrum, respectively. The dashed black lines and gray shaded regions give the median and 68% confidence intervals of the linear regression. Dotted lines are offset above and below the dashed line by the median value of the intrinsic scatter. Purple points are for the AGNs in this paper, red points are from W18, green points are from P14, blue points are from G17, the black point is from W20, and the orange point is from B21.

sources. We take advantage of the inclination estimates provided by our method to revisit the issue and do not find significant evidence of a correlation.[3] We also do not find any correlation with disk thickness, θ_o.

We do, however, find marginal (2.7σ) evidence for an anticorrelation between line-profile shape and Eddington ratio (when using the rms spectrum), which has also previously been suggested. Collin et al. (2006a) found a similar correlation but cautioned that the Eddington

[3]For readers who may recall that W18 found marginal evidence for a correlation between scale factor and BLR inclination, we would like to reiterate that the lack of correlation found here is between BLR inclination and line-profile shape. For followup work regarding correlations between scale factor and AGN/BLR parameters using our newly extended sample, the reader is referred to **?**.

rates were overestimated since the optical luminosity had not been corrected for host-galaxy starlight. Using host-galaxy starlight corrected optical luminosities from U et al. (2022), we find the observed anticorrelation to be stronger (2.7σ) when using the rms spectrum than when using the mean spectrum (2σ). This anti-correlation may suggest that the accretion rate plays a role in the BLR structure and kinematics, which in turn determines the line-profile shape. This is plausible if BLR geometry and kinematics depend on accretion rate.

Alternatively, it is also possible that the anti-correlation with Eddington ratio is merely a by-product of the apparent but not statistically significant (1.3σ as defined by our confidence intervals) correlation between line profile shape and black hole mass, since $L_{Bol}/L_{Edd} \propto 1/M_{BH}$. Followup work (Villafaña et al., 2023) will extend the analysis in this work and examine correlations between scale factor and M_{BH}, L_{Bol}/L_{Edd}, as well as FWHM/σ. The additional investigation of correlations with scale factor will allow us to further explore the relationship between the Hβ-emitting BLR and black hole mass/Eddington ratio, and their possible interpretations.

2.5 Conclusions

We have applied forward modeling techniques to a sample of nine AGNs from the LAMP 2016 reverberation mapping campaign, increasing the number of dynamically modeled sources by nearly 50%. We constrained the geometry and dynamics of the Hβ-emitting BLR and combined our results with previous studies (P14, G17, W18, W20, and B21) to investigate the existence of any trends in BLR structure and kinematics. Our main results are as follows.

1. Overall, we find the Hβ-emitting BLR of the LAMP 2016 sources to be best described by a thick disk observed at low to moderate inclination angles.

2. We find no luminosity-dependent trends in the Hβ-emitting BLR geometry and kinematics, and conclude that AGNs have diverse BLR structures and kinematics.

3. We find marginal evidence for an anti-correlation between the line-profile shape of the broad Hβ emission line and Eddington ratio. This may suggest that the accretion rate plays a role in BLR structure and kinematics. Alternatively, the anti-correlation could merely be a by-product of an correlation with black hole mass that we cannot detect given our uncertainties. Followup work will further examine these two possible interpretations.

With our simple phenomenological model we are able to gain insight on the BLR structure and kinematics in a more quantitative manner than the traditional interpretation of velocity-delay plots used in many reverberation mapping studies. Although much still remains unknown about the BLR, our findings suggest diversity that is consistent with transient AGN/BLR conditions over timescales of order months to years, rather than systematic trends. We note, however, that our combined sample is still small and may not be representative of the AGN population as a whole. Future reverberation mapping campaigns with sufficient data quality and variability will allow us to increase our sample size and thus improve the statistical significance of our findings.

Table 2.4. Linear regression results for line profile shape

Line Profile Shape		$\log_{10}(M_{bh}/M_{\odot})$	θ_i $(deg.)$	θ_o $(deg.)$	$\log_{10}(L_{bol}/L_{Edd})$
$\log_{10}\left(\frac{FWHM}{\sigma}\right)_{mean}$	α	0.08 ± 0.65	0.31 ± 17.0	0.24 ± 0.21	0.14 ± 0.10
	β	0.03 ± 0.09	-0.001 ± 0.78	0.002 ± 0.01	-0.13 ± 0.07
	σ_{int}	0.16 ± 0.01	$0.17\ ^{+0.02}_{-0.01}$	0.19 ± 0.02	0.15 ± 0.01
$\log_{10}\left(\frac{FWHM}{\sigma}\right)_{rms}$	α	-0.57 ± 0.69	0.40 ± 0.57	0.30 ± 0.21	0.13 ± 0.09
	β	0.12 ± 0.10	-0.005 ± 0.02	-0.0004 ± 0.01	-0.16 ± 0.07
	σ_{int}	0.15 ± 0.01	0.15 ± 0.01	0.18 ± 0.02	0.11 ± 0.01

Note. — Linear regression results for line profile shape vs. BLR/AGN parameters using both the mean and rms spectrum. The parameter α represents the constant in the regression and β represents the slope of the regression, while σ_{int} represents the standard deviation of the intrinsic scatter. The corresponding relationship is therefore given by $\log_{10}(FWHM/\sigma) = \alpha + \beta \times parameter + \mathcal{N}(0, \sigma_{int})$.

Acknowledgements

We are grateful to the following individuals for their time and effort contributed to the Lick observing campaign: (Shane) Zachary Parsons, Estefania Padilla Gonzalez, Noah Rivera, Cristilyn Gardner, Jake Haslemann, Sean Lewis, and Ellen Glad; (Nickel) Nick Choksi, Sameen Yunus, Jeffrey Molloy, Andrew Rikhter, and Haynes Stephens.

Photometric data collection at MLO was supported by National Science Foundation (NSF) grant AST-1210311; we thank Robert Quimby, Emma Lee, Joseph Tinglof, Eric McLaughlin, Amy Igarashi, and Tariq Johnson for assistance with these observations. We are deeply grateful to the UCO/Lick staff for help with scheduling and supporting the observations. Research at Lick Observatory is partially supported by a generous gift from Google.

The Kast red CCD detector upgrade, led by B. Holden, was made possible by the Heising-Simons Foundation, William and Marina Kast, and the University of California Observatories. KAIT and its ongoing operation were made possible by donations from Sun Microsystems, Inc., the Hewlett-Packard Company, AutoScope Corporation, Lick Observatory, the NSF, the University of California, the Sylvia & Jim Katzman Foundation, and the TABASGO Foundation.

L.V., P.R.W, and T.T. acknowledge support from the NSF through grant AST-1907208 "Collaborative Research: Establishing the Foundations of Black Hole Mass Measurements of AGN across Cosmic Time." Data presented herein were obtained using the UCI Remote Observing Facility, made possible by a generous gift from John and Ruth Ann Evans. Research at UC Irvine has been supported by NSF grants AST-1412693 and AST-1907208. V.U acknowledges funding support from the University of California Riverside's Chancellor's Postdoctoral Fellowship and National Aeronautics and Space Administration (NASA) Astrophysics Data Analysis Program Grant #80NSSC20K0450. Her work was conducted in part at the Aspen Center for Physics, which is supported by NSF grant PHY-1607611; she thanks

the Center for its hospitality during the “Astrophysics of Massive Black Holes Merger" workshop in June and July 2018. T.T. acknowledges support by the Packard Foundation through a Packard research fellowship. V.N.B. and I.S. gratefully acknowledge assistance from NSF Research at Undergraduate Institutions (RUI) grants AST-1312296 and AST-1909297. Note that findings and conclusions do not necessarily represent views of the NSF.

M.C.B. gratefully acknowledges support from the NSF through grant AST-2009230. G.C. acknowledges NSF support under grant AST-1817233. J.H.W. acknowledges funding from the Basic Science Research Program through the National Research Foundation of the Korean Government (NRF-2021R1A2C3008486). A.V.F.'s group at U.C. Berkeley is grateful for support from the TABASGO Foundation, the Christopher R. Redlich Fund, the Miller Institute for Basic Research in Science (in which he is a Miller Senior Fellow), and many individual donors. K.H. acknowledges support from STFC grant ST/R000824/1. We thank Marc J. Staley for a fellowship that partly funded B.E.S. whilst contributing to the work presented herein as a graduate student. I.S. acknowledges support from the Deutsche Forschungsgemeinschaft (DFG, German Research Foundation) under Germany's Excellence Strategy — EXC 2121 “Quantum Universe" — 390833306. Research by S.V. is supported by NSF grants AST–1813176 and AST-2008108.

This work makes use of observations from the LCOGT network. The Liverpool Telescope is operated on the island of La Palma by Liverpool John Moores University in the Spanish Observatorio del Roque de los Muchachos of the Instituto de Astrofisica de Canarias with financial support from the UK Science and Technology Facilities Council. Based on observations acquired at the Observatorio Astronómico Nacional in the Sierra San Pedro Mártir (OAN-SPM), Baja California, México, we thank the daytime and night support staff at the OAN-SPM for facilitating and helping obtain our observations. Some of the data used in this paper were acquired with the RATIR instrument, funded by the University of California and NASA Goddard Space Flight Center, and the 1.5 m Harold L. Johnson telescope at

the Observatorio Astronómico Nacional on the Sierra de San Pedro Mártir, operated and maintained by the Observatorio Astronómico Nacional and the Instituto de Astronomía of the Universidad Nacional Autónoma de México. Operations are partially funded by the Universidad Nacional Autónoma de México (DGAPA/PAPIIT IG100414, IT102715, AG100317, IN109418, IG100820, and IN105921). We acknowledge the contribution of Leonid Georgiev and Neil Gehrels to the development of RATIR.

This research was made possible through the use of the AAVSO Photometric All-Sky Survey (APASS), funded by the Robert Martin Ayers Sciences Fund and NSF grant AST-1412587 and contributed by observers worldwide. We acknowledge the use of The AGN Black Hole Mass Database as a compilation of some of the reverberation mapped black hole masses prior to 2015 (Bentz & Katz, 2015b). This research has made use of the NASA/IPAC Extragalactic Database (NED), which is operated by the Jet Propulsion Laboratory, California Institute of Technology, under contract with NASA.

2.6 Appendix

We include a summary of our model parameter estimates for the three sources excluded from this work (owing to moderate quality model fits) in Table **??** and their corresponding geometric interpretations in Figure 2.23. The model fits and a full detailed description of the BLR structure and kinematics for each source are found in the sections below. Transfer functions produced using the median model parameter estimates for each source are shown in Figures 2.25, 2.27, and 2.29.

2.6.1 Ark 120

Our model was able to fit the large-scale variations in the integrated Hβ emission line and shape of the line profile relatively well, only missing some of the finer fluctuations of the integrated emission line toward later epochs and some finer variations in intensity toward the

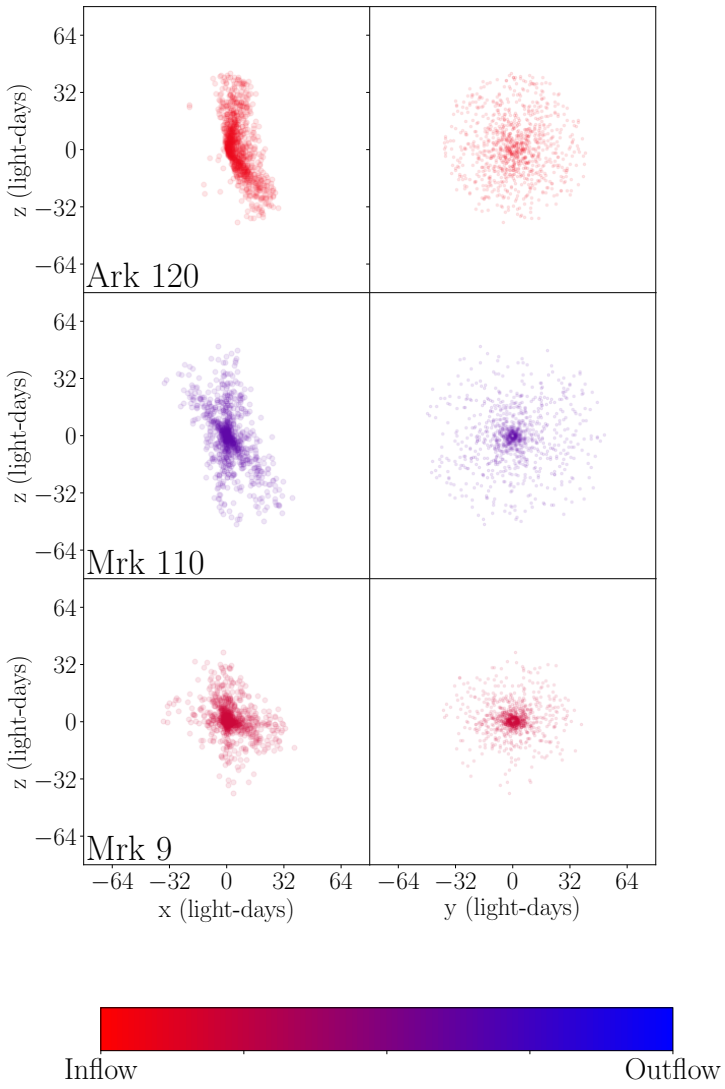

Figure 2.23 Geometric interpretation of BLR emission for the three LAMP 2016 sources excluded from our analysis (owing to moderate quality model fits) using median parameter estimates. For each source, the left panel shows an edge-on view while the right panel shows a face-on view. Each circle corresponds to one point particle in the model. The geometries are color-coded to indicate whether the BLR dynamics exhibit inflow (red) or outflow (blue).

start of the campaign (see panels 5 and 2, respectively, in Figure 2.24). Ultimately, we decided to exclude this source from our analysis due to our model's inability to fit the continuum light curve (see panel 6) toward the end of the observational campaign. Considering that the model Hβ emission line long-scale variations fit the data pretty well, the structure and

kinematics of Ark 120 can be described by the our model description below.

Geometrically, the BLR is modeled as a thick disk ($\theta_o = 32.0^{+7.1}_{-8.1}$ degrees) inclined $\theta_i = 13.6^{+3.5}_{-3.2}$ degrees toward an observer with a median BLR radius of $r_{median} = 17.9^{+2.1}_{-2.4}$ light-days. The data best fit a mostly opaque BLR midplane with $\xi = 0.02^{+0.04}_{-0.01}$, slight preferrential emission from the near side of the BLR ($\kappa = 0.26^{+0.18}_{-0.22}$), and slightly concentrated emission at the edges ($\gamma = 1.73^{+0.20}_{-0.55}$). Dynamically, our model suggests that $\sim 14\%$ of particles have nearly circular orbits with (f_{ellip}) $= 0.14^{+0.02}_{-0.03}$, with the remaining particles having velocities drawn from a Gaussian $v_r - v_\phi$ distribution rotated $\theta_e = 7.2^{+6.5}_{-4.8}$ degrees from radially inflowing ($f_{flow} = 0.25^{+0.17}_{-0.17}$) escape velocity to circular velocity. The contribution from macroturbulent velocities is small, with $\sigma_{turb} = 0.01^{+0.02}_{-0.00}$. Finally, we estimate a black hole mass of $\log_{10}(M_{bh}/M_\odot) = 8.26^{+0.12}_{-0.17}$ that is consistent within $\sim 1.3\sigma$ with the estimate $\log_{10}(M_{bh}/M_\odot) = 7.86^{+0.14}_{-0.14}$ found by U et al. (2022), with their standard assumption of virial coefficient $\log_{10}(f_{rms,\sigma})$= 0.65.

2.6.2 Mrk 110

Our model was able to fit the large-scale variations in the integrated Hβ emission line and shape of the line profile very well, missing only some of the finer features of the Hβ emission line core toward later epochs (see panel 2 in Figure 2.26). We now draw attention to panel 4, which depicts the implementation of a large statistical temperature in order to avoid overfitting, but results in very low S/N of the Hβ emission-line profile. Given the large uncertainty in the data (see panel 4) and thus increased (systematic) uncertainty in our model estimates, we decided to exclude the source from our analysis. This increased uncertainty, however, is taken into account in our model estimates which we describe below.

Our model finds that the BLR is best described by a thick disk ($\theta_o = 27^{+16}_{-13}$ degrees) inclined $\theta_i = 19.9^{+9.6}_{-11}$degrees toward the observer with a median radius of $r_{median} = 13.9^{+2.0}_{-1.8}$ light-days. The data favor a transparent BLR midplane ($\xi = 0.88^{+0.09}_{-0.19}$) and preferential emission from the

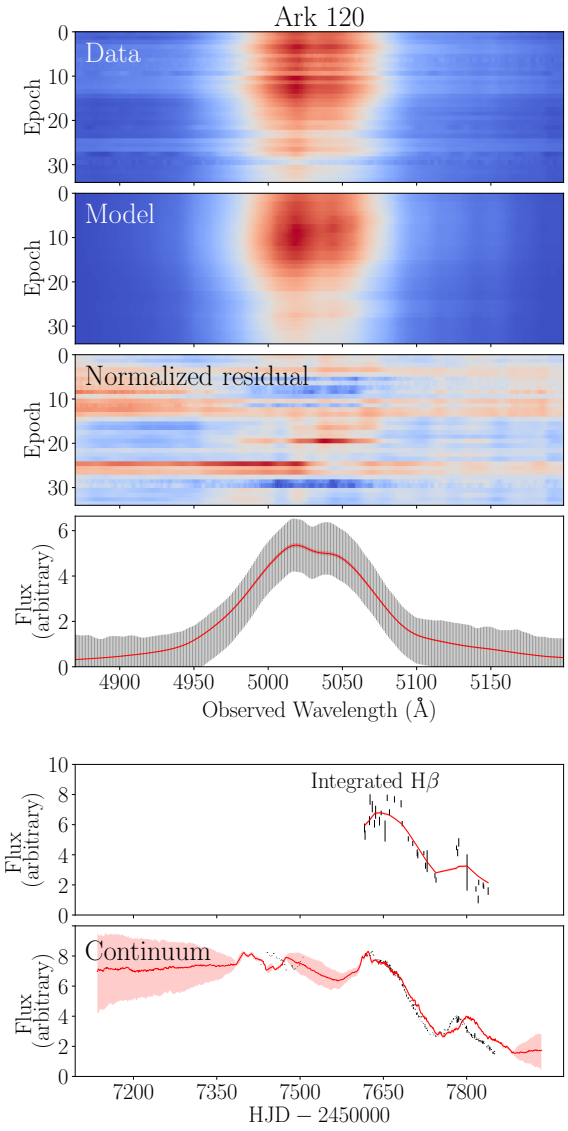

Figure 2.24 Model fits to the Hβ line profile, integrated Hβ flux, and AGN continuum flux for Ark 120. Labeling panels 1-6 from top to bottom, panels 1 and 2 show the observed intensity of the Hβ emission-line profile by observation epoch and the profile produced by one sample of the CARAMEL BLR and continuum model. Panel 3 shows the resulting normalized residual. Panel 4 shows the observed Hβ profile of one randomly chosen epoch in black and the corresponding profile produced by the model in panel 2, in red. The corresponding error bars of the observed epoch have been multiplied by $\sqrt{T}$, where T is the DNEST4 statistical "temperature" that is used as a likelihood softening parameter post analysis. Panels 5 & 6 show the time series of the observed integrated Hβ and continuum flux in black and the corresponding model fits (of the model shown in panel 2) of the light curves in red.

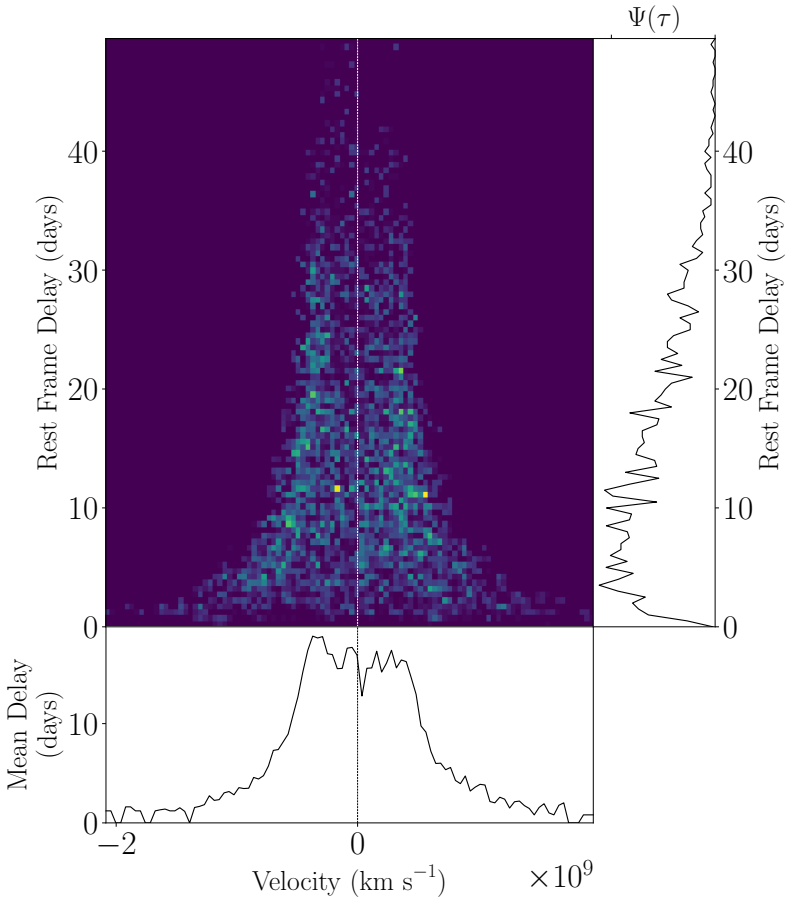

Figure 2.25 Ark 120 transfer function produced using median model parameter estimates. The right- hand panel shows the velocity-integrated transfer function and the bottom panel shows the average time lag for each velocity pixel.

far side of the BLR ($\kappa = -0.41^{+0.42}_{-0.06}$). Our model is unable to constrain, however, whether emission is isotropic/concentrated at the edges ($\gamma = 1.59^{+0.29}_{-0.36}$). Dynamically, our model suggests that over half of the particles have nearly circular orbits ($f_{ellip} = 0.60^{+0.15}_{-0.20}$), with the remaining particles having velocities drawn from a Gaussian distribution in the $v_r - v_\phi$ distribution rotated $\theta_e = 13.7^{+15.5}_{-9.9}$ degrees from the radially outflowing ($f_{flow} = 0.66^{+0.22}_{-0.39}$) escape velocity toward circular velocity. The contribution from macroturbulent velocities is small, with $\sigma_{turb} = 0.01^{+0.04}_{-0.01}$. Finally, we find a black hole mass of $\log_{10}(M_{bh}/M_\odot) = 7.17^{+0.67}_{-0.26}$, which is consistent with the estimate of $\log_{10}(M_{bh}/M_\odot) = 7.54^{+0.08}_{-0.13}$, found by U et al. (2022).

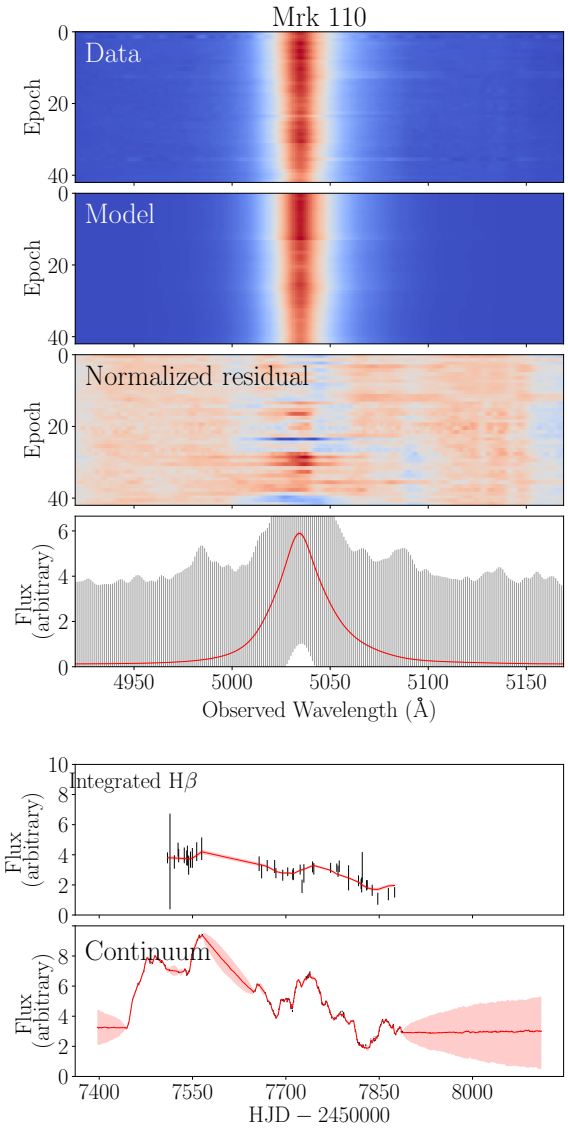

Figure 2.26 Model fits to the Hβ line profile, integrated Hβ flux, and AGN continuum flux for Mrk 110. See Figure 2.24 caption for panel descriptions.

2.6.3 Mrk 9

Similar to the case of Mrk 110, our model was able to fit the large-scale variations in the integrated Hβ emission line and shape of the line profile very well for Mrk 9. As seen in Figure 2.28, panel 2, our model only misses some of the finer features of the Hβ emission line core toward earlier epochs. Our model is also able to capture the long-scale variations in the

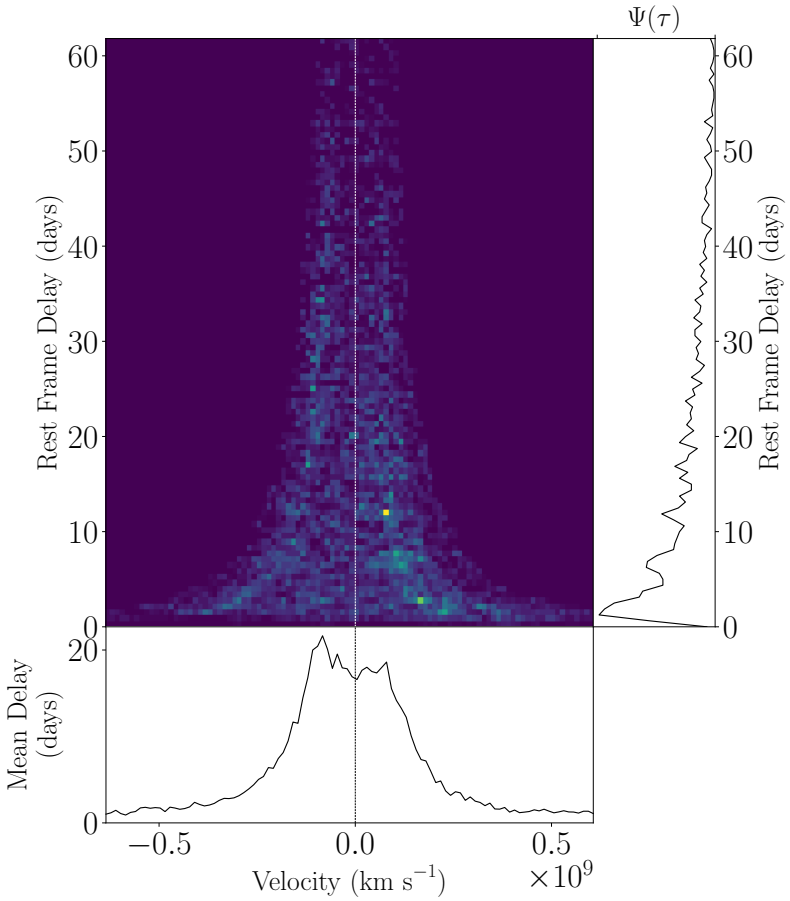

Figure 2.27 Mrk 110 transfer function produced using median model parameter estimates. See Figure 2.25 caption for panel descriptions.

integrated Hβ emission line (panel 5) and AGN continuum (panel 6). However, as seen in panel 4, the model for this source required implementing a large statistical temperature in order to avoid overfitting, which resulted in low S/N of the Hβ emission-line profile. Given the large uncertainty in the data (see panel 4) and thus increased uncertainty in our model estimates, we excluded the source from our analysis. This increased uncertainty, however, is taken into account in our model estimates which we describe below.

The data best fit a thick disk ($\theta_o = 45^{+17}_{-17}$) Hβ-emitting BLR, viewed at an inclination of $\theta_i = 42^{+12}_{-15}$ degrees with a median radius of $r_{median} = 8.0^{+2.8}_{-1.9}$ light-days. Our model finds a slight preference for an opaque BLR midplane with $\xi = 0.52^{+0.21}_{-0.20}$ and a mostly isotropic

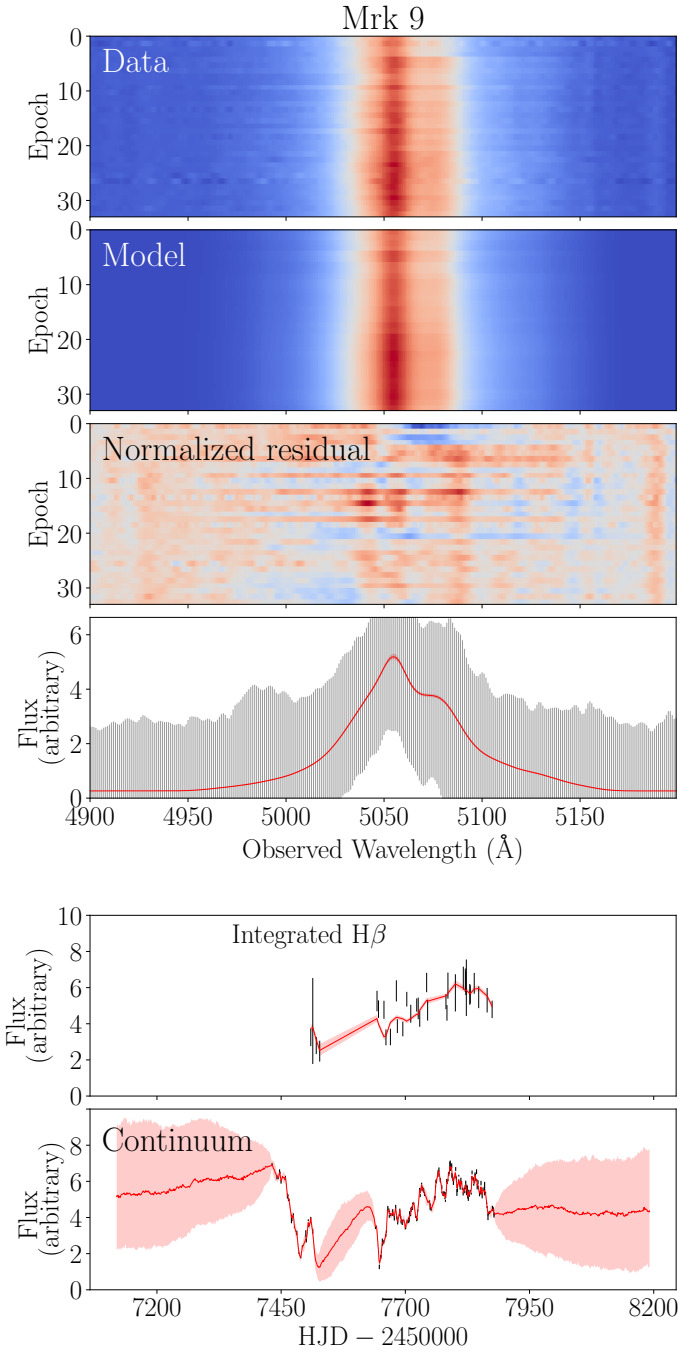

Figure 2.28 Model fits to the Hβ line profile, integrated Hβ flux, and AGN continuum flux for Mrk 9. See Figure 2.24 caption for panel descriptions.

BLR with $\kappa = 0.02^{+0.11}_{-0.11}$. The model is unable to constrain whether emission is uniformly emitted or concentrated at the edges ($\gamma = 1.56^{+0.29}_{-0.33}$), however. Dynamically, our model

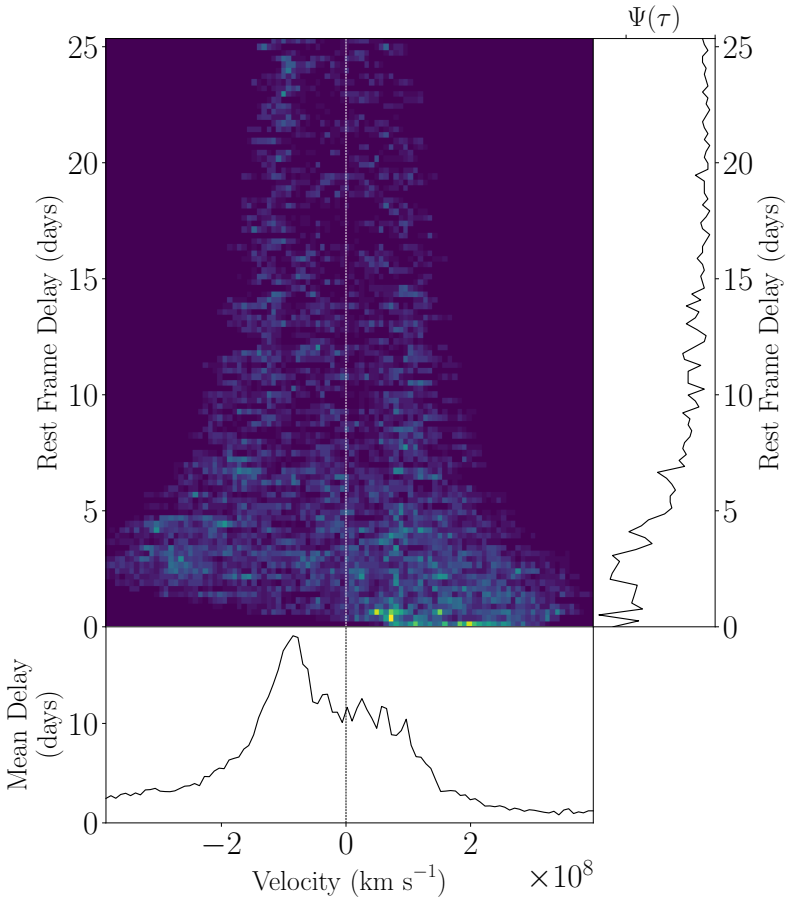

Figure 2.29 Mrk 9 transfer function produced using median model parameter estimates. See Figure 2.25 caption for panel descriptions.

finds $\sim 12\%$ of the particles have circular orbits ($f_{ellip} = 0.12^{+0.17}_{-0.08}$). The remaining particles having velocities drawn from a Gaussian $v_r - v_\phi$ distribution rotated $\theta_e = 45^{+15}_{-28}$ degrees from radially inflowing ($f_{flow} = 0.27^{+0.20}_{-0.18}$) escape velocity to circular velocity. The contribution from macroturbulent velocities is small, with $\sigma_{turb} = 0.01^{+0.04}_{-0.01}$. Finally, we estimate a black hole mass of $\log_{10}(M_{bh}/M_\odot) = 7.09^{+0.22}_{-0.23}$, which is consistent within 1σ uncertainties of the estimate $\log_{10}(M_{bh}/M_\odot) = 7.61^{+0.12}_{-0.31}$ found by U et al. (2022).

CHAPTER 3

What Does the Geometry of the Hβ BLR Depend On?

This chapter was published as Villafaña, L., Williams, P.R., Treu, T. et al.; "What Does the Geometry of the Hβ BLR Depend On?," ApJ, 948, 95 (2023), and is reproduced here with minor formatting adjustments

3.1 Introduction

It is widely accepted that most galaxies host a supermassive black hole in their center. When the black hole accretes material, it gives rise to a bright central source, known as an active galactic nucleus (AGN). Tight correlations between black hole mass and host-galaxy properties (e.g., Magorrian et al., 1998; Ferrarese & Merritt, 2000b; Gebhardt et al., 2000b; Kormendy & Ho, 2013b) suggest that AGNs play an important role in galaxy evolution. To understand such a link, both a better understanding of the central regions of AGNs *and* improved black hole mass estimates are needed (Ding et al., 2020b). Black hole mass estimators applicable to cosmologically significant lookback times are particularly desirable as they allow for the determination of the cosmic evolution of the galaxy black hole mass correlations (e.g., Treu et al., 2004; Woo et al., 2006; Salviander et al., 2007; Woo et al., 2008; Shields & Salviander, 2009; Bennert et al., 2010; Schulze & Wisotzki, 2011; Targett et al., 2012; Ding et al., 2020b).

Beyond our local universe, the black hole's gravitational sphere of influence cannot be spa-

tially resolved with current technology, and thus dynamical black hole mass measurements (e.g., modeling stellar/gas kinematics) cannot be constrained (Kormendy & Richstone, 1995; Ferrarese & Ford, 2005), with rare exceptions (e.g., 3C 273, IRAS 09149–6206; Gravity Collaboration et al., 2018, 2020). Instead, reverberation mapping is the primary tool used to estimate black hole masses in the distant universe, with a limited application to broad-line (Type 1) AGNs.

The technique resolves the gravitational sphere of influence of the central black hole in time by utilizing variations in the continuum that are later reverberated by the broad emission lines (Blandford & McKee 1982; Peterson 1993; for a review, see Cackett et al. 2021). Assuming the delay in variations is due solely to light-travel time, the radius of the broad-line region (BLR) is measured by combining the observed time lag, τ, with the speed of light. A second key assumption — BLR kinematics are dominated by the black hole's gravity — provides the velocity of the emitting gas, v, as determined by the width of the broad line. Combining the size of the BLR with its velocity, a virial constraint of the black hole's mass (M_{BH}) is given by

$$M_{BH} = f\frac{c\tau v^2}{G} = fM_{vir}, \tag{3.1}$$

where f, or the "virial coefficient," is a dimensionless scale factor of order unity that captures the relation between measured line-shape parameters and BLR geometry/dynamics, and $c\tau v^2/G$ is referred to as the virial product (M_{vir}).

In principle, construction of a velocity-delay map, which maps continuum variations to the broad-line flux variations as both a function of line-of-sight velocity and time delay, allows one to constrain the BLR geometry (Blandford & McKee, 1982). In practice, however, interpretation is nontrivial, and much about the structure and kinematics of the BLR still remains unknown. For this reason, it is currently impossible to determine the scale factor for

an individual AGN using traditional reverberation mapping techniques. Instead, a constant average scale factor, found by aligning reverberation mapped AGNs to the local M_{BH}–σ_* relation, is often used for traditional reverberation mapping black hole mass estimates (Onken et al., 2004; Collin et al., 2006a; Woo et al., 2010, 2013; Graham et al., 2011; Park et al., 2012a; Grier et al., 2013; Woo et al., 2015; Batiste et al., 2017).

Over the last several years, our team has set out to provide a more reliable way to calibrate the virial coefficient and uncover any regularity in BLR behavior. The discovery of any trends would thus provide *both* insight into the inner regions of AGNs and improve the way black hole masses are calibrated across cosmic time.

Using the methods introduced by Pancoast et al. (2011), such as the Code for AGN Reverberation and Modeling of Emission Lines (CARAMEL), we explore a phenomenological description of the BLR and constrain a black hole mass that is consistent with the reverberation mapping dataset, without the need of assuming a scale factor. In this paper, we combine our CARAMEL M_{BH} estimates for the nine sources modeled from the Lick AGN Monitoring Project 2016 (LAMP 2016; Villafaña et al., 2022, hereafter V22) with those from prior CARAMEL studies, and determine AGN-specific virial coefficients in order to search for a more reliable way to calibrate f.

This paper is organized as follows. We summarize the geometry and kinematics of the CARAMEL model in Section 3.2 and outline our methodology in calculating AGN-specific virial coefficients in Section 3.3. A systematic investigation of correlations between f and observables is carried out in Section 3.4. Specifically, we consider correlations with AGN/BLR model parameters in Section 3.4.1 and line-profile shape in Section 3.4.2. We then investigate the effects of BLR geometry and kinematics on BLR line-profile shape in Section 3.5 and summarize our main conclusions in Section 3.6.

3.2 Summary of Relevant CARAMEL Model Parameters

Our work builds on the CARAMEL modeling results of V22, Bentz et al. (2022, hereafter B22), Bentz et al. (2021, hereafter B21), Williams et al. (2020, hereafter W20), Williams et al. (2018, hereafter W18), Grier et al. (2017, hereafter G17), and Pancoast et al. (2014, hereafter P14). In this section we provide a brief summary of the CARAMEL model detailed by P14.

Briefly, CARAMEL is a phenomenological model that uses velocity-resolved reverberation mapping datasets to model the BLR emissivity distribution. The BLR is modeled by point particles, surrounding the black hole located at the origin, which instantaneously reemit light received from the ionizing source, toward an observer.

3.2.1 BLR Geometry

The radial distribution of the BLR point particles is drawn from a Gamma distribution with shape parameter α and scale parameter θ,

$$p(x|\alpha,\theta) \propto x^{\alpha-1} \exp\left(-\frac{x}{\theta}\right). \tag{3.2}$$

The distribution is then shifted from the origin by the Schwarzchild radius plus a free parameter $r_{\rm min}$, which sets the minimum BLR radius. This is then followed by a change of variables from $(\alpha, \theta, r_{\rm min})$ to (μ, β, F), such that:

$$\mu = r_{\rm min} + \alpha\theta\,, \tag{3.3}$$

$$\beta = \frac{1}{\sqrt{\alpha}}\,,\ \textit{and} \tag{3.4}$$

$$F = \frac{r_{\rm min}}{r_{\rm min} + \alpha\theta}\,. \tag{3.5}$$

With this change of variables, the two CARAMEL model parameters closely associated with BLR size are μ and F; the parameter μ describes the mean radius, while the parameter F describes the minimum radius in units of μ.

After the change of variables, the BLR disk thickness is then determined by the model parameter θ_o. The opening angle, θ_o, corresponds to half the angular thickness of the BLR in the angular spherical polar coordinate, such that $\theta_o = 90°$ corresponds to a spherical BLR. The BLR inclination angle, θ_i, is then determined by the angle between a face-on disk and the observer's line of sight. In this way, a face-on BLR geometry would correspond to $\theta_i \to 0$ and an edge-on BLR geometry $\theta_i \to 90°$.

Once the BLR geometry is determined from the parameters described above and a few additional parameters (for a full description of the geometric model, please see P14), the kinematics are set by a number of parameters that allow for elliptical, inflowing/outflowing orbits, and macroturbulent contributions.

3.2.2 BLR Kinematics

Particle velocities are modeled using both radial and tangential velocity distributions, with a fraction of particles, $f_{\rm ellip}$, on near-circular orbits around the central black hole. The remaining $1 - f_{\rm ellip}$ particles can have either inflowing/outflowing orbits, and the direction of motion is determined by the parameter $f_{\rm flow}$. Inflow motion is defined by values of $f_{\rm flow} < 0.5$ and outflow motion is defined by values of $f_{\rm flow} > 0.5$.

Whether these orbits are bound or unbound is then determined by the parameter θ_e, which describes the angle between escape velocity and circular velocity. In this way, $\theta_e \to 0°$ represents nearly unbound orbits, $\theta_e \to 90°$ represents nearly-circular orbits, and values of $\theta_e \approx 45°$ represent highly elliptical (bound) orbits. Using the kinematic parameters described above, inflow/outflow motion can be summarized by the $In. - Out.$ parameter created by W18,

$$In. - Out. = sgn(f_{\rm flow} - 0.5) \times (1 - f_{\rm ellip}) \times \cos(\theta_e)\,, \tag{3.6}$$

where sgn is the sign function. Values of -1 indicate pure radial inflow and values of 1 indicate pure radial outflow.

Lastly, in addition to inflow/outflow motion, the model also allows for macroturbulent contributions by including the following $v_{\rm turb}$ velocity to the line-of-sight velocity:

$$v_{\rm turb} = \mathcal{N}(0, \sigma_{\rm turb})|v_{\rm circ}|\,, \tag{3.7}$$

where $|v_{\rm circ}|$ represents circular velocity as determined by the central black hole's mass, and $\mathcal{N}(0, \sigma_{\rm turb})$ is a Gaussian distribution with standard deviation $\sigma_{\rm turb}$. The free parameter $\sigma_{\rm turb}$ is allowed to range from 0.001 to 0.1 and thus represents the contribution of macroturbulent velocities. For each particle, we find the elliptical, inflowing, or outflowing velocity first, and then add the magnitude of the macroturbulent velocity, $v_{\rm turb}$, determined.

3.2.3 Model Results

In addition to the geometric and dynamical model parameters described above, we also include a black hole mass parameter, M_{BH}, with a log uniform prior between $2.78 \times 10^4 - 1.67 \times 10^9 M_\odot$. Including black hole mass as a model parameter allows us to constrain M_{BH}, without the use of the scale factor, f (Eqn. 3.1). To interpret the results, we use the posterior distribution functions CARAMEL produces for the model parameters, and report the median value and 68% confidence interval for 1σ uncertainties.

In this paper, we use the CARAMEL results found by V22 for the LAMP 2016 sample, and results from our extended sample's respective papers (P14; G17; W18; B21, and B22). We note that as outlined in the Appendix of Williams & Treu (2022), the CARAMEL code has undergone some minor modifications since its original publication. These changes were im-

plemented for the work of V22, but not for the modeling results of the rest of the subsamples included in our extended sample – W18, G17, P14, W20, B21, and B22. However, using a subsample of AGNs modeled with the original code, we have found that the updated code used by V22 does not significantly change the results produced by the original code (e.g., W18, G17, P14, W20, B21, and B22) (Colleyn, in prep.). For further details regarding modifications made to the code, please refer to Appendix 3.7.1.

3.3 The Virial Coefficient

A key CARAMEL result is black hole mass, which allows us to determine an AGN-specific virial coefficient for each AGN modeled (see Eqn. 3.1). In this section, we summarize the different ways line widths are measured for reverberation mapping black hole mass estimates and our methodology for determining individual AGN virial coefficients.

3.3.1 Line-Width Measurements

The line width of the broad emission line, which is used to determine the speed of the BLR gas (Eq. 3.1), can either be measured from the root-mean-square (rms) spectrum, or from the mean spectrum. Measurements taken from the rms spectrum are computed with the intent that only the variable part of the line will contribute to the line-width calculation (Shen, 2013). However, whenever the rms profile cannot be measured, owing to insufficient epochs or low signal-to-noise ratio, the line width is often calculated using the mean spectra instead (e.g., Denney et al., 2010).

In either case, the line width measured from the spectra selected (i.e., rms or mean) is then characterized by either the full width at half-maximum intensity (FWHM) or the line dispersion, σ_{line} (i.e., the second moment of the line). The FWHM simply corresponds to the difference between wavelengths from both sides of the peak, $P(\lambda)_{max}$, at half of the height. We determine σ_{line} using the definition of Peterson et al. (2004):

$$\sigma^2_{line}(\lambda) = \langle\lambda^2\rangle - \lambda_0^2, \tag{3.8}$$

where

$$\langle\lambda^2\rangle = \frac{\int \lambda^2 P(\lambda) d\lambda}{\int P(\lambda) d\lambda} \tag{3.9}$$

and

$$\lambda_0 = \frac{\int \lambda P(\lambda) d\lambda}{\int P(\lambda) d\lambda}. \tag{3.10}$$

Both the width type (i.e., FWHM or σ_{line}) and spectra (i.e., rms or mean) used to measure the line width then determine which calibrated scale factor is needed to calculate the virial M_{BH} (Eq. 3.1). For example, Woo et al. (2015) derived a constant f factor based on the M–σ_* relation calibration, for both FWHM-based and σ_{line}-based M_{BH} estimates.

3.3.2 AGN-Specific Virial Coefficient Calculations

For completeness, we determine all four versions of the scale factor ($\log_{10} f_{FWHM,rms}$, $\log_{10} f_{\sigma,rms}$, $\log_{10} f_{FWHM,mean}$, and $\log_{10} f_{\sigma,mean}$), although measurements using the line dispersion from the rms spectra have been suggested to produce less biased M_{BH} estimates (e.g., Peterson et al., 2004; Collin et al., 2006b).

3.3.2.1 LAMP 2016 Sample

To calculate the scale factor for each LAMP 2016 source modeled by V22, we follow the same approach taken by all other previous CARAMEL works – we combine the cross-correlation time-lag (τ_{cen}) and line-width (v) values measured by the campaign's respective reverberation mapping analysis (U et al., 2022) with the M_{BH} measurements determined from our forward-

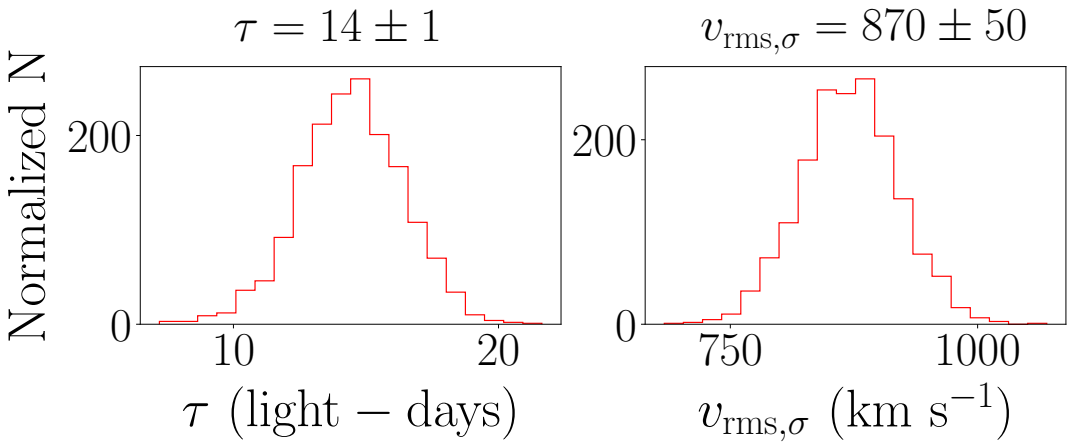

Figure 3.1 To propagate uncertainties, we assume Gaussian errors on the cross-correlation time lag (left) and line-width (right) measurements given by U et al. (2022). This allows us to create distribution functions that we can utilize with our CARAMEL M_{BH} posterior distribution function to determine the distribution of the scale factor of an individual source, from which we use the 68% confidence interval for 1σ uncertainties.

modelling approach (M_{BH} measurements for the LAMP 2016 sample can be found in V22).

To propagate uncertainties, we first assume Gaussian errors on the τ_{cen} and v measurements using the standard deviations listed by U et al. (2022) (see Figure 3.1 below). For measurements with asymmetrical error bars, the average of the lower and upper errors is used for the standard deviation of the Gaussian distribution.

Then, we take random draws from the Gaussian distributions of the τ_{cen} and v measurements, and calculate the virial product, $M_{vir} = c\tau v^2/G$, until the number of draws is equal to the size of the M_{BH} posterior sample produced by CARAMEL. Finally, we find a posterior distribution for the scale factor by dividing the M_{BH} distribution produced by CARAMEL by the virial product distribution created above (see Figure 3.2 below). From the posterior distribution produced, we report the median value and use a 68% confidence interval for 1σ uncertainties. Results for the individual scale factors of the LAMP 2016 sample are listed in Table 3.1.

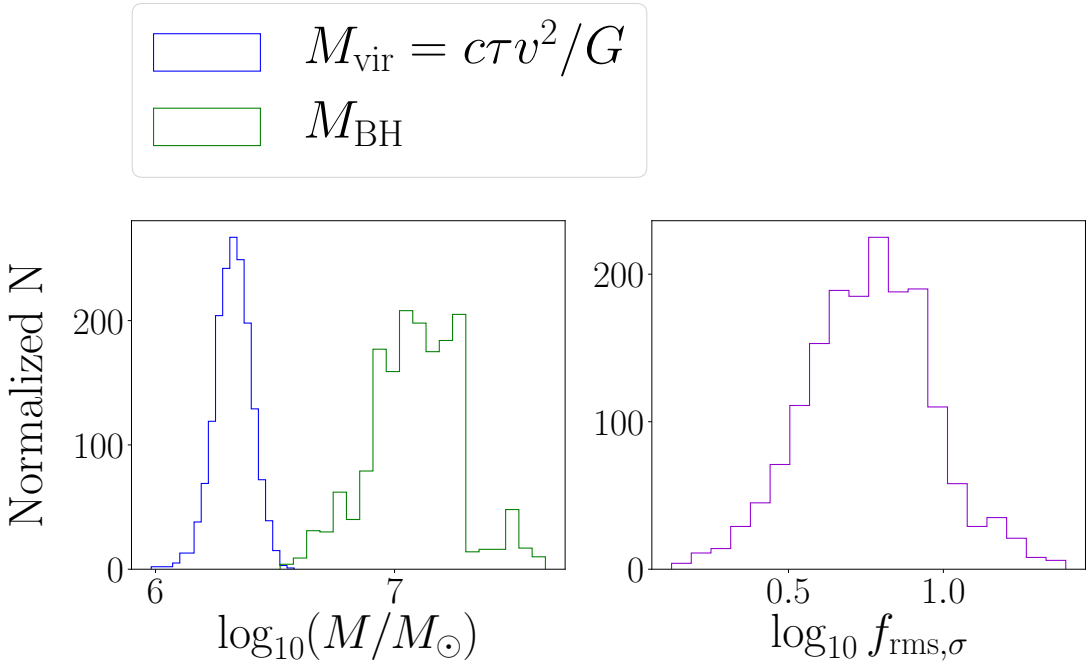

Figure 3.2 Taking random draws from the Gaussian distributions of the cross-correlation time lag and line widths (Figure 3.1), we calculate the virial product (shown in blue in the left panel) until the size of the virial product distribution is the same as that of the CARAMEL M_{BH} posterior distribution function (shown in green in the left panel). The logarithmic virial coefficient of any given source in our sample is found by subtracting the logarithmic virial product distribution from the logarithmic CARAMEL M_{BH} posterior distribution (i.e., dividing the original, nonlogarithmic distributions). The resulting distribution of logarithmic scale factor ($\log_{10}(f_{rms,\sigma})$) is shown on the right panel, which allows us to report errors on our measurement by quoting the 68% confidence interval as define by the distribution.

3.3.2.2 Extended Sample

We extend our sample (see Table 4.1) by combining our results with prior CARAMEL studies — namely seven from LAMP 2011 (W18), four from AGN10 (G17), five from LAMP 2008 (P14), one from AGNSTORM (W20), one from B21, and one from B22.

The line widths used to compute the virial coefficient using the approach described above can be found in Table 3.5. All line widths correspond to those used in our previous CARAMEL studies, with the exception of the four from the AGN 10 (G17) campaign. The line widths previously used did not have the narrow-line component removed. In order to remain con-

Table 3.1. Inferred Scale Factors

Galaxy	$\log_{10}(f_{rms,\sigma})$	$\log_{10}(f_{rms,FWHM})$	$\log_{10}(f_{mean,\sigma})$	$\log_{10}(f_{mean,FWHM})$
PG 2209+184	$0.84^{+0.21}_{-0.20}$	$0.08^{+0.21}_{-0.20}$	$0.71^{+0.21}_{-0.19}$	$-0.11^{+0.21}_{-0.20}$
MCG +04-22-042	$1.21^{+0.41}_{-0.31}$	$0.54^{+0.41}_{-0.31}$	$1.08^{+0.41}_{-0.31}$	$0.34^{+0.41}_{-0.31}$
Mrk 1392	$1.10^{+0.12}_{-0.14}$	$0.32^{+0.13}_{-0.14}$	$1.02^{+0.12}_{-0.14}$	$0.19^{+0.12}_{-0.14}$
RBS 1303	$0.05^{+0.27}_{-0.20}$	$-0.23^{+0.25}_{-0.17}$	$0.07^{+0.24}_{-0.16}$	$-0.46^{+0.23}_{-0.16}$
RBS 1917	$0.82^{+0.32}_{-0.34}$	$0.54^{+0.26}_{-0.32}$	$0.54^{+0.27}_{-0.32}$	$-0.08^{+0.50}_{0.32}$
Mrk 841	$0.62^{+0.50}_{-0.34}$	$-0.40^{+0.47}_{-0.38}$	$0.67^{+0.50}_{-0.36}$	$-0.38^{+0.50}_{-0.36}$
RXJ 2044.0+2833	$0.76^{+0.19}_{-0.19}$	$0.02^{+0.18}_{-0.20}$	$0.66^{+0.18}_{-0.20}$	$-0.04^{+0.18}_{-0.20}$
NPM1G+27.0587	$0.98^{+0.51}_{-0.47}$	$0.53^{+0.52}_{-0.46}$	$1.01^{+0.50}_{-0.47}$	$0.37^{+0.52}_{-0.46}$
Mrk 1048	$1.05^{+0.65}_{-0.57}$	$0.33^{+0.64}_{-0.61}$	$1.00^{+0.66}_{-0.57}$	$0.16^{+0.66}_{-0.58}$

Note. — Individual scale factors for the nine LAMP 2016 sources modeled by V22. Values were determined using our model M_{BH} estimates and corresponding line widths and cross correlation time lags found by U et al. (2022). Individual scale factors of our extended sample can be found in their respective CARAMEL papers: P14; G17; W18; W20; B21; and B22.

sistent within our extended sample when searching for correlations with line-profile shape, we remeasured the line widths of these four points using the data from G17, in which the narrow-line contribution had been removed. To remeasure these line widths, we used the methods of U et al. (2022) and computed a Monte Carlo bootstrapping procedure for error analysis.

The values of the individual AGN-specific virial coefficients are also found in their respective CARAMEL papers and were determined in the same fashion as the LAMP 2016 sample described above.

3.4 Results

Using the individual AGN-specific virial coefficients determined for our extended sample, and enabled by our CARAMEL forward modeling approach, we carry out a systematic investigation of correlations between f and observables.

We use the IDL routine `linmix_err` (Kelly, 2007) to perform a Bayesian linear regression in order to account for correlated measurement uncertainties. Doing so allows us to analyze the

Table 3.2. Extended Sample

Campaign	Galaxy	Redshift	$\log_{10}(M_{BH}/M_{\odot})$
Lick AGN Monitoring Project 2008 (Pancoast et al., 2014)	Arp 151	0.02109	$6.62^{+0.10}_{-0.13}$
	Mrk 1310	0.01941	$7.42^{+0.26}_{-0.27}$
	NGC 5548	0.01718	$7.51^{+0.23}_{-0.14}$
	NGC 6814	0.00521	$6.42^{+0.24}_{-0.18}$
	SBS 1116+583A	0.02787	$6.99^{+0.32}_{-0.25}$
2010 AGN monitoring campaign at MDM Observatory (Grier et al., 2017)	Mrk 335	0.0258	$7.25^{+0.10}_{-0.10}$
	Mrk 1501	0.0893	$7.86^{+0.20}_{-0.17}$
	3C 120	0.0330	$7.84^{+0.14}_{-0.19}$
	PG 2130+099	0.0630	$6.92^{+0.24}_{-0.23}$
Lick AGN Monitoring Project 2011 (Williams et al., 2018)	Mrk 50	0.0234	$7.50^{+0.25}_{-0.18}$
	Mrk 141	0.0417	$7.46^{+0.15}_{-0.21}$
	Mrk 279	0.0305	$7.58^{+0.08}_{-0.08}$
	Mrk 1511	0.0339	$7.11^{+0.20}_{-0.17}$
	NGC 4593	0.0090	$6.65^{+0.27}_{-0.15}$
	Zw 229-015	0.0279	$6.94^{+0.14}_{-0.14}$
	PG 1310-108	0.0343	$6.48^{+0.21}_{-0.18}$
Space Telescope and Optical Reverberation Mapping Project (Williams et al., 2020)	NGC 5548	0.017175	$7.64^{+0.21}_{-0.18}$
AGN monitoring campaign at Las Cumbres Observatory (Bentz et al., 2021)	NGC 3783	0.097	$7.51^{+0.26}_{-0.13}$
Lick AGN Monitoring Project 2016 (Villafaña et al., 2022)	PG 2209+184	0.07000	$7.53^{+0.19}_{-0.20}$
	RBS 1917	0.06600	$7.04^{+0.23}_{-0.35}$
	MCG +04-22-042	0.03235	$7.59^{+0.42}_{-0.28}$
	NPM1G+27.0587	0.06200	$7.64^{+0.40}_{-0.36}$
	Mrk 1392	0.03614	$8.16^{+0.11}_{-0.13}$
	RBS 1303	0.04179	$6.79^{+0.19}_{-0.11}$
	Mrk 1048	0.04314	$7.79^{+0.44}_{-0.48}$
	RXJ 2044.0+2833	0.05000	$7.09^{+0.17}_{-0.17}$
	Mrk 841	0.03642	$7.62^{+0.50}_{-0.30}$
AGN monitoring campaign at MDM Observatory (Bentz et al., 2022)	NGC 4151	0.0033	$7.22^{+0.11}_{-0.10}$

Note. — Extended sample includes sources modeled by P14, G17, W18, W20, B21, and B22, in addition to the most recent sampled modeled by V22. Column 1 specifies the campaign from which data were collected and galaxy name is found in column 2. Columns 3 and 4 list the galaxy's redshift and CARAMEL M_{BH} estimate, as defined by the 68% confidence interval of the resultant posterior distribution function, respectively.

actual intrinsic correlation of any two parameters without worrying about a false increase due to correlated measurement uncertainties. This is especially important for our search for correlations with scale factor since individual scale factors are determined using our model M_{BH} measurements, and therefore uncertainties in the scale factor are connected to uncertainties in other model parameters.

To quantify the strength of any correlation, we compare the median fit slope to the 1σ uncertainty in the slope and determine our level of confidence using the following intervals we have defined in our previous study W18: we classify 0–2σ as no evidence, 2–3σ as marginal evidence, 3–5σ as evidence, and $> 5\sigma$ as conclusive evidence.

Overall, we find the following correlations with at least marginal evidence as defined by our confidence intervals:

1. **Black Hole Mass:**

$$\log_{10}(f_{mean,\sigma}) \text{ vs. } \log_{10}(M_{BH}/M_{\odot});$$
$$\beta = 0.51 \pm 0.15,\ \sigma_{int} = 0.22 \pm 0.05,$$
$$3.4\sigma \text{ evidence}$$

$$\log_{10}(f_{rms,\sigma}) \text{ vs. } \log_{10}(M_{BH}/M_{\odot})$$
$$\beta = 0.47 \pm 0.17,\ \sigma_{int} = 0.25^{+0.06}_{-0.05},$$
$$2.8\sigma \text{ marginal evidence}$$

2. **Opening Angle (BLR disk thickness):**

$$\log_{10}(f_{mean,FWHM}) \text{ vs. } \theta_o;$$
$$\beta = -0.96^{+0.47}_{-0.43},\ \sigma_{int} = 0.22^{+0.06}_{-0.05}$$
$$2.1\sigma \text{ marginal evidence}$$

$$\log_{10}(f_{rms,FWHM}) \text{ vs. } \theta_o;$$

$$\beta = -1.15^{+0.48}_{-0.46},\ \sigma_{int} = 0.21^{+0.06}_{-0.05}$$

2.4σ marginal evidence

3. **Inclination Angle:**

$$\log_{10}(f_{mean,FWHM}) \text{ vs. } \theta_i;$$

$$\beta = -1.45^{+0.53}_{-0.56},\ \sigma_{int} = 0.17^{+0.05}_{-0.04}$$

2.6σ marginal evidence

$$\log_{10}(f_{rms,\sigma}) \text{ vs. } \theta_i;$$

$$\beta = -1.61^{+0.66}_{-0.68},\ \sigma_{int} = 0.22^{+0.06}_{-0.05}$$

2.4σ marginal evidence

$$\log_{10}(f_{mean,\sigma}) \text{ vs. } \theta_i;$$

$$\beta = -1.37^{+0.66}_{-0.68},\ \sigma_{int} = 0.23 \pm 0.05$$

2.0σ marginal evidence

4. **Line-Profile Shape:**

$$(\text{FWHM}/\sigma)_{rms} \text{ vs. } \log_{10}(f_{rms,\sigma});$$

$$\beta = 1.50^{+0.67}_{-0.71},\ \sigma_{int} = 0.24^{+0.09}_{-0.08}$$

2.2σ marginal evidence

3.4.1 Correlations between f & AGN/BLR Parameters

In an effort to uncover any regularities in the behavior of the BLR and gain a better understanding of the inner regions of AGNs, we investigate correlations between scale factor and AGN/BLR parameters determined by our forward-modelling approach. Overall, we find similar trends for both the rms and mean spectrum — see Figures 3.3 and 3.4 (respectively), and Tables 3.3 and 3.4, for their corresponding regression values.

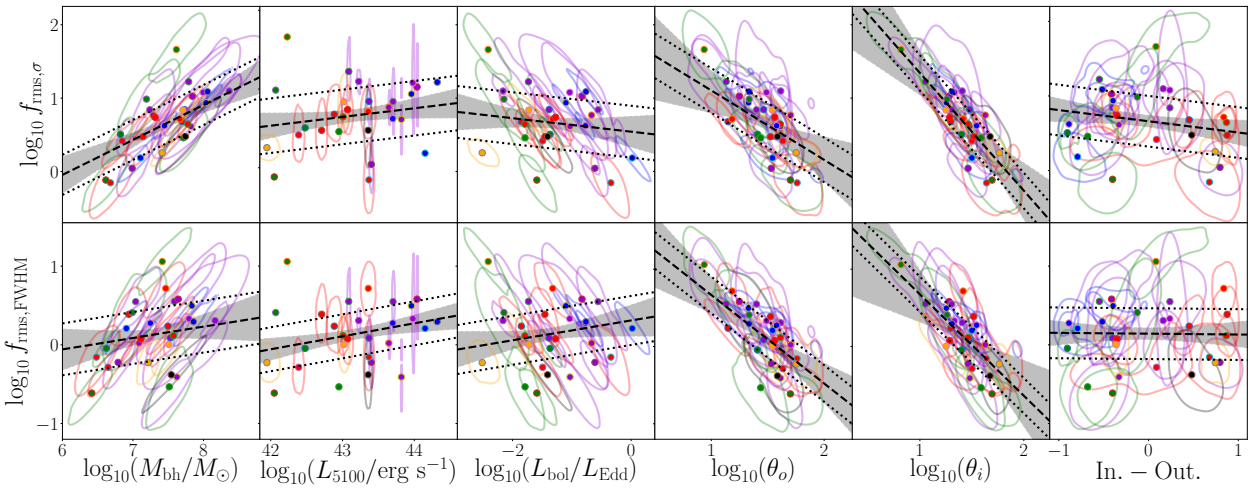

Figure 3.3 Correlations between the scale factor $\log_{10} f_{rms,\sigma}$ (top) and $\log_{10} f_{rms,FWHM}$ (bottom) with select AGNs and model parameters. From left to right: M_{BH}, optical luminosity, Eddington ratio, Hβ -emitting BLR opening angle (disk thickness), Hβ -emitting BLR inclination angle, and our "inflow-outflow" parameter. The colored dots and contours show the median and 68% confidence regions of the 2D posterior PDFs for each AGN. The dashed black lines and gray shaded regions give the median and 68% confidence intervals of the linear regression. Dotted lines are offset above and below the dashed line by the median value of the intrinsic scatter. Purple points are for the AGNs from V22, red points are from W18, green points are from P14, blue points are from G17, the black point is from W20, and the orange points are from B21 and B22.

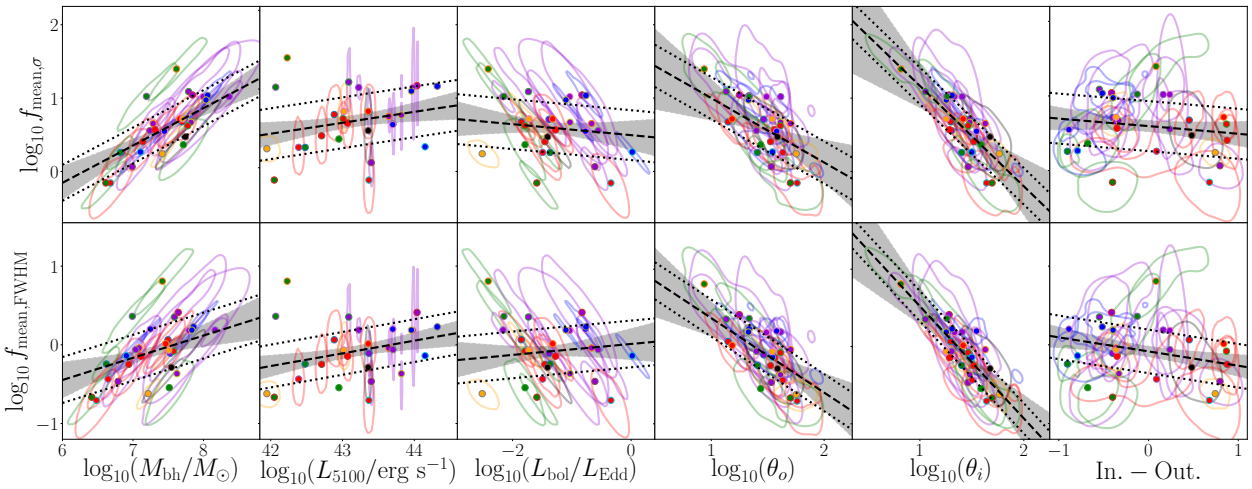

Figure 3.4 Correlations between the scale factor $\log_{10} f_{mean,\sigma}$ (top) and $\log_{10} f_{mean,FWHM}$ (bottom) with select AGNs and model parameters. From left to right: M_{BH}, optical luminosity, Eddington ratio, Hβ -emitting BLR opening angle (disk thickness), Hβ -emitting BLR inclination angle, and our "inflow-outflow" parameter. The colored dots and contours show the median and 68% confidence regions of the 2D posterior PDFs for each AGN. The dashed black lines and gray shaded regions give the median and 68% confidence intervals of the linear regression. Dotted lines are offset above and below the dashed line by the median value of the intrinsic scatter. Purple points are for the AGNs from V22, red points are from W18, green points are from P14, blue points are from G17, the black point is from W20, and the orange points are from B21 and B22.

Table 3.3. Linear regression results for rms spectrum scale factors

f-type		$\log_{10}(M_{BH}/M_\odot)$	$\log_{10}(L_{5100}/erg\ s^{-1})$	$\log_{10}(L_{bol}/L_{Edd})$	$\theta_o\ (deg.)$	$\theta_i\ (deg.)$	$In.-Out.\ param.$
rms, σ	α	$-2.74^{+1.22}_{-1.24}$	$-4.03^{+5.19}_{-5.03}$	0.55 ± 0.21	$2.05^{+0.81}_{-0.90}$	$2.95^{+0.97}_{-0.96}$	0.67 ± 0.08
	β	0.47 ± 0.17	0.11 ± 0.12	$-0.09^{+0.14}_{-0.15}$	$-0.95^{+0.60}_{-0.54}$	$-1.61^{+0.66}_{-0.68}$	-0.16 ± 0.14
	σ_{int}	$0.25^{+0.06}_{-0.05}$	$0.31^{+0.09}_{-0.08}$	$0.32^{+0.08}_{-0.07}$	$0.28^{+0.07}_{-0.05}$	$0.22^{+0.06}_{-0.05}$	$0.31^{+0.08}_{-0.07}$
rms, FWHM	α	$-0.91^{+1.41}_{-1.43}$	$-7.18^{+4.70}_{-4.33}$	$0.32^{+0.19}_{-0.20}$	$1.82^{+0.68}_{-0.71}$	$1.99^{+0.99}_{-1.16}$	0.15 ± 0.07
	β	$0.14^{+0.20}_{-0.19}$	$0.17^{+0.10}_{-0.11}$	$0.13^{+0.13}_{-0.14}$	$-1.15^{+0.48}_{-0.46}$	$-1.31^{+0.80}_{-0.69}$	-0.01 ± 0.14
	σ_{int}	$0.29^{+0.08}_{-0.07}$	0.24 ± 0.09	$0.27^{+0.09}_{-0.08}$	$0.21^{+0.06}_{-0.05}$	$0.20^{+0.06}_{-0.05}$	$0.29^{+0.09}_{-0.08}$

Note. — Linear regression results used to determine correlations between the scale factor f and select AGNs and model parameters shown in Figure 3.3. The parameters α and β represent the constant and slope of the linear regression, respectively. While σ_{int} represents the standard deviation of the intrinsic scatter. The corresponding relationship is therefore given by $\log_{10} f = \alpha + \beta \times parameter + \mathcal{N}(0, \sigma_{int})$.

Table 3.4. Linear regression results for mean spectrum scale factors

f-type		$\log_{10}(M_{BH}/M_\odot)$	$\log_{10}(L_{5100}/erg\ s^{-1})$	$\log_{10}(L_{bol}/L_{Edd})$	θ_o $(deg.)$	θ_i $(deg.)$	$In.-Out.\ param.$
mean, σ	α	$-3.11^{+1.06}_{-1.10}$	$-5.47^{+4.87}_{-4.61}$	$0.51^{+0.19}_{-0.20}$	$1.88^{+0.75}_{-0.88}$	$2.53^{+0.98}_{-0.94}$	0.60 ± 0.08
	β	0.51 ± 0.15	0.14 ± 0.11	$-0.07^{+0.13}_{-0.14}$	$-0.88^{+0.59}_{-0.50}$	$-1.37^{+0.66}_{-0.68}$	-0.10 ± 0.14
	σ_{int}	0.22 ± 0.05	$0.29^{+0.08}_{-0.07}$	$0.30^{+0.08}_{-0.06}$	$0.26^{+0.06}_{-0.05}$	0.23 ± 0.05	$0.30^{+0.08}_{-0.07}$
mean, FWHM	α	$-1.99^{+1.26}_{-1.28}$	$-7.13^{+4.37}_{-4.04}$	0.01 ± 0.20	$1.33^{+0.63}_{-0.70}$	$1.97^{+0.81}_{-0.75}$	-0.08 ± 0.07
	β	$0.26^{+0.18}_{-0.17}$	$0.16^{+0.09}_{-0.10}$	$0.07^{+0.13}_{-0.14}$	$-0.96^{+0.47}_{-0.43}$	$-1.45^{+0.53}_{-0.56}$	-0.18 ± 0.12
	σ_{int}	0.26 ± 0.06	$0.23^{+0.08}_{-0.07}$	$0.26^{+0.08}_{-0.07}$	$0.22^{+0.06}_{-0.05}$	$0.17^{+0.05}_{-0.04}$	$0.24^{+0.07}_{-0.06}$

Note. — Linear regression results used to determine correlations between the scale factor f and select AGNs and model parameters shown in Figure 3.4. The parameters α and β represent the constant and slope of the linear regression, respectively. While σ_{int} represents the standard deviation of the intrinsic scatter. The corresponding relationship is therefore given by $\log_{10} f = \alpha + \beta \times parameter + \mathcal{N}(0, \sigma_{int})$.

We reiterate that covariance between variables is taken into account in our analysis, in order to avoid spurious correlations. We find evidence (3.4σ) for a correlation between scale factor and M_{BH} when using the mean spectrum and line dispersion line width, i.e. $\log_{10}(f_{mean,\sigma})$ ($\beta = 0.51 \pm 0.15$), which had not been previously found by P14, G17, or W18. Similarly, we find marginal evidence (2.8σ) for a correlation between $\log_{10}(f_{rms,\sigma})$ and M_{BH} ($\beta = 0.47 \pm 0.17$). This correlation suggests that the BLR geometry and dynamics may be correlated with M_{BH}.

We also find marginal evidence for an anti-correlation with BLR opening angle, θ_o, which is the CARAMEL model parameter that represents the BLR disk thickness. When using FWHM line-width measurements with both the mean ($\beta = -0.96^{+0.47}_{-0.43}$) and rms ($\beta = -1.15^{+0.48}_{-0.46}$) spectrum. Such a correlation with BLR disk thickness had also not been previously found in any previous CARAMEL studies.

Finally, in agreement with previous results (P14; G17; W18), we find marginal evidence for an anti-correlation with BLR inclination angle and the virial coefficient, as measured when using the σ line width with both the rms ($\beta = -1.61^{+0.66}_{-0.68}$) and mean ($\beta = -1.37^{+0.67}_{-0.71}$) spectra. Additionally, we also find marginal evidence for an anti-correlation when using the FWHM line width and the mean spectrum ($\beta = -1.45^{+0.53}_{-0.56}$). This correlation was predicted by both Collin et al. (2006a) and Goad et al. (2012), and is expected for a disk-like BLR because an increase in BLR inclination angle would result in an increased observed line-of-sight velocity and therefore increased line-width measurement. Hence, in order to recover the same M_{BH}, a smaller scale factor would be required, producing an anti-correlation like the one that is apparent in our work.

Before proceeding, it is important to note that although the correlations we have discovered with opening angle (BLR disk thickness) and inclination angle fall under our definition of marginally significant, they lack any real utility as BLR disk thickness is not an observable or a measurable quantity, and inclination-angle measurements using radio jets (e.g., Jorstad

et al., 2005; Agudo et al., 2012) are not possible for all cases. For these reasons, we now explore the existence of correlations between scale factor and a direct observable, line-profile shape — that is, the ratio of the FWHM to the dispersion σ_{line}, as such a correlation would provide an observational proxy for the virial coefficient, and thus a more reliable way to calibrate f.

3.4.2 Line-Profile Shape as an Observational Proxy

We search for correlations with scale factor and line-profile shape using both the rms and mean spectrum (see Figures 3.5 and 3.6, respectively), where we have used only the shape of the Hβ broad emission line by itself (i.e., we have isolated the broad emission from the narrow emission component). Line widths and line-profile shapes used for our extended sample are listed in Table 3.5.

We find marginal evidence (2.2σ) for a correlation between $\log_{10}(f_{rms,\sigma})$ and line-profile shape, when using the rms spectrum ($\beta = 1.50^{+0.67}_{-0.71}$). When using the mean spectrum, however, the correlation falls short of being considered marginal evidence and is quantified by 1.9σ (see the left-most panels of Figure 3.5 and 3.6, respectively). We do not find any evidence for a correlation with the virial coefficient when a FWHM line width is used, in either the rms or mean spectrum (see the right-most panels of Figures 3.5 and 3.6).

Although stronger evidence is needed to recommend the widespread use of this relationship, this result is promising; further investigations with increased sample size in our dynamic modeling may help elucidate the correlation we have found.

Table 3.5. Line Widths and Line Profile Shapes of Extended Sample

Galaxy	Rms FWHM	Rms σ_{line}	Rms $\log_{10}(FWHM/\sigma)$	Mean FWHM	Mean σ_{line}	Mean $\log_{10}(FWHM/\sigma)$
Arp 151 (P11)	$2458 \pm 82^{(a)}$	$1295 \pm 37^{(a)}$	0.28 ± 0.02	$3076 \pm 39^{(a)}$	$1726 \pm 17^{(a)}$	0.25 ± 0.007
Mrk 1310 (P11)	$1823 \pm 157^{(a)}$	$921 \pm 135^{(a)}$	0.30 ± 0.07	$2425 \pm 19^{(a)}$	$1229 \pm 12^{(a)}$	0.29 ± 0.005
NGC 5548 (P11)	$12539 \pm 1927^{(a)}$	$3900 \pm 266^{(a)}$	$0.51^{+0.08}_{-0.07}$	$12402 \pm 111^{(a)}$	$4354 \pm 25^{(a)}$	0.45 ± 0.004
NGC 6814 (P11)	$2945 \pm 283^{(a)}$	$1697 \pm 224^{(a)}$	0.24 ± 0.07	$3129 \pm 14^{(a)}$	$1744 \pm 12^{(a)}$	0.25 ± 0.003
SBS 1116+583A (P11)	...	...	...	$3135 \pm 36^{(a)}$	$1460 \pm 23^{(a)}$	0.33 ± 0.01
Mrk 335 (G17)	$1853 \pm 79^{(b)}$	$1239 \pm 78^{(b)}$	0.17 ± 0.03	$2018 \pm 1^{(b)}$	$1354 \pm 34^{(b)}$	0.17 ± 0.01
Mrk 1501 (G17)	$3476 \pm 214^{(b)}$	$1401 \pm 48^{(b)}$	0.40 ± 0.03	$3780 \pm 25^{(b)}$	$1486 \pm 48^{(b)}$	0.41 ± 0.01
3C 120 (G17)	$2035 \pm 97^{(b)}$	$1218 \pm 47^{(b)}$	0.22 ± 0.03	$2893 \pm 22^{(b)}$	$1175 \pm 26^{(b)}$	0.39 ± 0.01
PG 2130+099 (G17)	$1409 \pm 143^{(b)}$	$1459 \pm 93^{(b)}$	-0.02 ± 0.05	$2107 \pm 32^{(b)}$	$1321 \pm 11^{(b)}$	0.20 ± 0.01
Mrk 50 (W18)	$3355 \pm 128^{(c)}$	$2020 \pm 103^{(c)}$	0.22 ± 0.03	$4101 \pm 56^{(c)}$	$2024 \pm 31^{(c)}$	0.31 ± 0.01
Mrk 141 (W18)	...	...	...	$5129 \pm 45^{(c)}$	$2280 \pm 21^{(c)}$	0.35 ± 0.01
Mrk 279 (W18)	$3306 \pm 338^{(c)}$	$1778 \pm 71^{(c)}$	0.27 ± 0.05	$4099 \pm 43^{(c)}$	$1821 \pm 13^{(c)}$	0.35 ± 0.01
Mrk 1511 (W18)	$3236 \pm 65^{(c)}$	$1506 \pm 42^{(c)}$	$0.33^{+0.02}_{-0.01}$	$4154 \pm 28^{(c)}$	$1828 \pm 12^{(c)}$	0.36 ± 0.004
NGC 4593 (W18)	$3597 \pm 72^{(c)}$	$1601 \pm 40^{(c)}$	0.35 ± 0.01	$4264 \pm 41^{(c)}$	$1925 \pm 38^{(c)}$	0.35 ± 0.01
Zw 229-015 (W18)	$1789 \pm 93^{(c)}$	$1609 \pm 109^{(c)}$	0.05 ± 0.04	$3705 \pm 203^{(c)}$	$1747 \pm 56^{(c)}$	0.33 ± 0.03
PG 1310-108 (W18)	...	...	...	$3422 \pm 21^{(c)}$	$1823 \pm 20^{(c)}$	0.27 ± 0.01
NGC 5548 (W20)	$10861 \pm 739^{(d)}$	$4115 \pm 513^{(d)}$	$0.42^{+0.06}_{-0.07}$	$9612 \pm 427^{(d)}$	$3983 \pm 150^{(d)}$	$0.38^{+0.02}_{-0.03}$
NGC 3783 (B21)	$4278 \pm 676^{(e)}$	$1619 \pm 137^{(e)}$	$0.42^{+0.08}_{-0.07}$	$4486 \pm 35^{(e)}$	$1825 \pm 19^{(e)}$	0.39 ± 0.01
PG 2209+184 (V22)	$3247 \pm 88^{(f)}$	$1353 \pm 64^{(f)}$	0.38 ± 0.02	$4045 \pm 34^{(f)}$	$1573 \pm 40^{(f)}$	0.41 ± 0.01
MCG +04-22-042(V22)	$2120 \pm 39^{(f)}$	$977 \pm 29^{(f)}$	$0.34^{+0.01}_{-0.02}$	$2658 \pm 57^{(f)}$	$1141 \pm 39^{(f)}$	0.37 ± 0.02
Mrk 1392 (V22)	$3690 \pm 138^{(f)}$	$1501 \pm 38^{(f)}$	0.39 ± 0.02	$4267 \pm 25^{(f)}$	$1635 \pm 13^{(f)}$	0.417 ± 0.004
RBS 1303 (V22)	$1738 \pm 113^{(f)}$	$1292 \pm 156^{(f)}$	0.13 ± 0.06	$2286 \pm 21^{(f)}$	$1243 \pm 26^{(f)}$	0.26 ± 0.01
RBS 1917 (V22)	$1653 \pm 287^{(f)}$	$851 \pm 154^{(f)}$	$0.14^{+0.07}_{-0.09}$	$2399 \pm 11^{(f)}$	$1180 \pm 50^{(f)}$	0.31 ± 0.02
Mrk 841 (V22)	$7452 \pm 660^{(f)}$	$2278 \pm 96^{(f)}$	0.51 ± 0.04	$7073 \pm 311^{(f)}$	$2139 \pm 55^{(f)}$	0.52 ± 0.02
RXJ 2044.0+2833 (V22)	$2047 \pm 72^{(f)}$	$870 \pm 50^{(f)}$	0.37 ± 0.03	$2196 \pm 31^{(f)}$	$989 \pm 32^{(f)}$	$0.35^{+0.01}_{-0.02}$
NPM1G+27.0587 (V22)	$2893 \pm 177^{(f)}$	$1735 \pm 136^{(f)}$	$0.22^{+0.04}_{-0.05}$	$3501 \pm 28^{(f)}$	$1683 \pm 42^{(f)}$	0.32 ± 0.01
Mrk 1048 (V22)	$4042 \pm 406^{(f)}$	$1726 \pm 76^{(f)}$	0.37 ± 0.05	$4830 \pm 80^{(f)}$	$1840 \pm 58^{(f)}$	0.42 ± 0.02
NGC 4151 (B22)	$4711 \pm 750^{(g)}$	$2680 \pm 64^{(g)}$	$0.25^{+0.08}_{-0.06}$	$7382 \pm 279^{(g)}$	$2724 \pm 17^{(g)}$	0.43 ± 0.02

Note. — References for line widths are as follows: (a) Park et al. (2012b), (b) This work — the measurements used in previous CARAMEL studies originated from Grier et al. (2012), which did not remove the narrow line contribution. Thus, we remeasured using the data and spectral decompositions used by G17, in order to ensure these line width measurements were consistent with the rest of the sample, i.e. with the narrow line contribution removed. (c) Barth et al. (2015b), (d) Pei et al. (2017b), (e) Bentz et al. (2021), (f) U et al. (2022), (g) Bentz et al. (2006).

Table 3.6. Linear regression results for line profile shape vs. scale factor

Line Profile Shape		$\log_{10} f_\sigma$	$\log_{10} f_{FWHM}$
$\log_{10}\left(\frac{FWHM}{\sigma}\right)_{mean}$	α	-0.001 ± 0.32	$0.01^{+0.31}_{-0.32}$
	β	$1.76^{+0.94}_{-0.93}$	$-0.28^{+0.93}_{-0.92}$
	σ_{int}	$0.28^{+0.08}_{-0.06}$	$0.28^{+0.08}_{-0.06}$
$\log_{10}\left(\frac{FWHM}{\sigma}\right)_{rms}$	α	$0.25^{+0.21}_{-0.20}$	$0.39^{+0.22}_{-0.21}$
	β	$1.50^{+0.67}_{-0.71}$	$-0.95^{+0.69}_{-0.73}$
	σ_{int}	$0.24^{+0.09}_{-0.08}$	$0.26^{+0.09}_{-0.07}$

Note. — Linear regression results for line profile shape vs. scale factor. The parameters α and β represent the constant and slope of the regression, respectively, while σ_{int} represents the standard deviation of the intrinsic scatter. The corresponding relationship is therefore given by $\log_{10}(f) = \alpha + \beta \log_{10}(FWHM/\sigma) + \mathcal{N}(0, \sigma_{int})$.

3.5 The Role of BLR Geometry and Kinematics on Line-Profile Shape

From the correlations found in our work, we focus on the correlation found with $\log_{10}(FWHM/\sigma)$, which has significant potential to improve the way the virial coefficient is calibrated. The relationship has an intrinsic scatter of similar magnitude to that of the local M_{BH}–σ_* relation (see Table 3.6), which suggests another intrinsic relation of AGNs, and further validates the idea of using the line-profile shape of broad emission lines as a tracer for the inner regions of AGNs (Collin et al., 2006a). In an attempt to gain a better understanding, we employ CARAMEL models to test how BLR geometry and kinematics affects line-profile shape.

In particular, we aim to understand the line profiles with $\log_{10}(FWHM/\sigma)_{mean} \approx 0.1$–$0.2$. While line profiles with $\log_{10}(FWHM/\sigma) = 0.37$ are best described by a Gaussian and are due to rotational Doppler broadening, Lorentz profiles (e.g., $\log_{10}(FWHM/\sigma) < 0.37$) are thought to be a result of turbulent and/or inflow/outflow motions (Kollatschny & Zetzl,

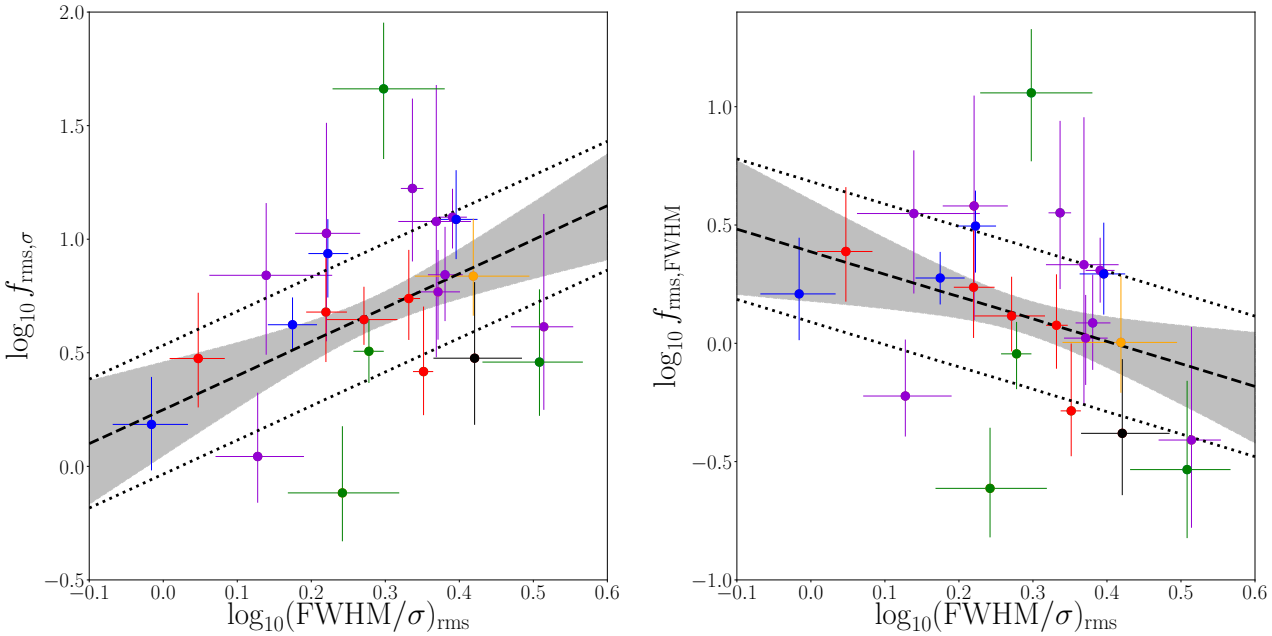

Figure 3.5 Correlations between rms line-profile shape and scale factor determined using line dispersion (left) and FWHM (right). The dashed black lines and gray shaded regions give the median and 68% confidence intervals of the linear regression. Dotted lines are offset above and below the dashed line by the median value of the intrinsic scatter. Purple points are for the AGNs from V22, red points are from W18, green points are from P14, blue points are from G17, the black point is from W20, and the two orange points are from B21 and B22.

2013). In the following subsections, we investigate the effect of BLR size, disk thickness, inflow/outflow motion, and turbulent motion on Hβ broad line-profile shapes.

3.5.1 BLR Size

We begin by testing the effect of BLR size, since the extended wings in a Lorentz profile are due to high-velocity gas near the black hole. Thus, assuming Keplerian orbits, we expect narrower line-profile shapes to correspond to smaller BLR radii. We manipulate the CARAMEL model parameters associated with BLR radius, μ and F, while keeping all other parameters constant. The values chosen for other relevant geometry and kinematics are as follows: $\theta_i = 20°$, $\theta_o = 20°$, $\beta = 1.0$, $\log_{10}(\mathrm{M}_{BH}/M_\odot) = 7.5$, $f_{flow} = 0.5$, $f_{ellip} = 1.0$, $\theta_e = 90°$, $\sigma_{turb} = 0.001$. We choose the parameters to reflect particles with bound circular

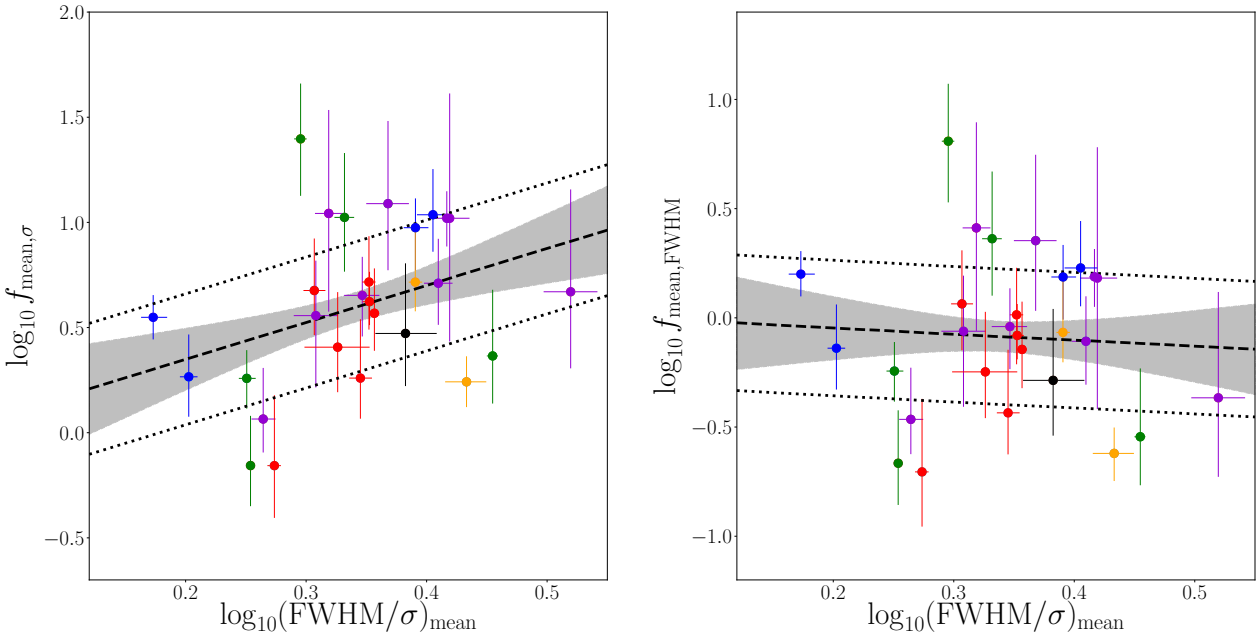

Figure 3.6 Correlations between mean line-profile shape and scale factor determined using line dispersion (left) and FWHM (right). The dashed black lines and gray shaded regions give the median and 68% confidence intervals of the linear regression. Dotted lines are offset above and below the dashed line by the median value of the intrinsic scatter. Purple points are for the AGNs from V22, red points are from W18, green points are from P14, blue points are from G17, the black point is from W20, and the two orange points are from B21 and B22.

orbits (no inflow/outflow motion) and minimal contribution from macroturbulent velocities.

As shown in Figure 3.7, we find a smaller BLR size produces a smaller value of $\log_{10}(FWHM/\sigma)$, as expected. However, we do not find any line-profile shapes in the region of special interest, $\log_{10}(FWHM/\sigma)_{mean} \approx 0.1$–$0.2$, which suggests that bound circular orbits cannot produce these particular broad-line-profile shapes. Given the result that smaller BLR sizes produce smaller values of $\log_{10}(FWHM/\sigma)$, and our ultimate goal of investigating what BLR geometry and kinematics produce smaller line-profile shapes, the remaining of our CARAMEL model tests will focus solely on BLR sizes with mean radius, $\mu = 1$ and minimum radius within the range $F = 0$–0.3.

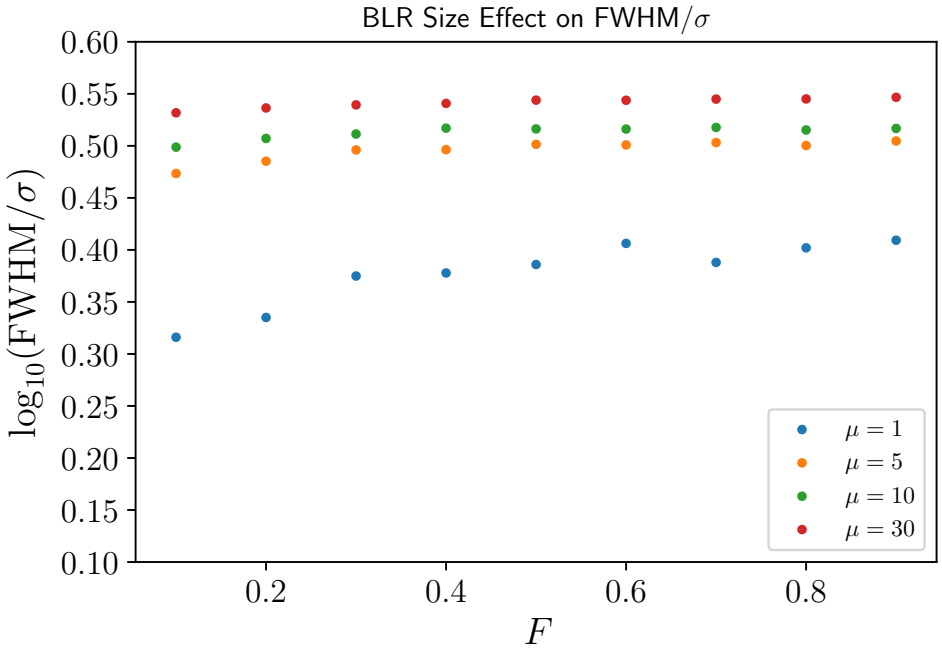

Figure 3.7 We investigate the role of BLR radius in line profile shape using CARAMEL models by varying the parameters μ and F, and holding all other model parameters constant. As described in the text, the parameter μ defines the mean BLR radius and the parameter F defines the minimum radius in units of μ. Different mean BLR radii, μ, are depicted in different colors: 1 light-day is shown in blue, 5 light-days is shown in orange, 10 light-days is shown in green, and 30 light-days is shown in red. As expected, smaller values of $\log_{10}(FWHM/\sigma)_{mean}$ on the y-axis, are seen with decreasing μ. Additionally, within the four different mean radii, μ, a slight decrease is seen for a decrease in minimum radius, as depicted by decreasing values of F shown on the x-axis.

3.5.2 BLR Disk Thickness

Next we test whether BLR disk thickness plays a role in determining the Hβ broad-line-profile shape. This idea stems from Pringle (1981), who found that the geometric height of an accretion disk is proportional to the ratio of turbulent velocity to rotational velocity of the disk. And although this notion applies to accretion disks, disk-outflow models which suggest that the BLR and the obscuring torus are closely connected, possibly forming one continuous structure that feeds/flows from the central accretion disk (e.g., Emmering et al., 1992; Konigl & Kartje, 1994; Kartje & Königl, 1996; Kishimoto et al., 2011; Koshida, 2015),

qualify the application to a BLR disk. Thus, as suggested by Kollatschny & Zetzl (2011), BLR lines with smaller values of $\log_{10}(FWHM/\sigma)$ must have more of a spherical structure.

Using our CARAMEL models, we vary θ_o and F, and keep all other parameters set to the following values: $\theta_i = 25°$, $\beta = 1.0$, $\mu = 1$, $\log_{10}(\mathrm{M}_{BH}/M_\odot) = 7.5$, $f_{flow} = 0.5$, $f_{ellip} = 1.0$, $\theta_e = 90°$, $\sigma_{turb} = 0.001$. Again, this configuration was selected in order to reflect particles on bound circular orbits. As expected, larger opening angles θ_o (i.e., thicker BLR disks) produce broad lines with smaller values of $\log_{10}(FWHM/\sigma)_{mean}$ (see Figure 3.8). The spherical BLR disk represented by $\theta_o = 45°$ even begins to have a line-profile shape defined by $\log_{10}(\mathrm{FWHM}/\sigma) \approx 0.2$, with bound circular orbits (without inflow/outflow and/or turbulent motion).

3.5.3 Inflow/Outflow Motion

For this test we vary f_{ellip} (the fraction of particles with elliptical orbits) while keeping all other parameters held constant. The values selected for all other parameters are as follows: $\theta_i = 25°$, $\beta = 1.0$, $\mu = 1$, $\log_{10}(\mathrm{M}_{BH}/M_\odot) = 7.5$, $\theta_e = 45°$, $\sigma_{turb} = 0.001$. We use a value of $f_{flow} = 0.1$ for inflow motion, and a value of $f_{flow} = 0.9$ for outflow motion. Additionally, we also use two separate disk thickness parameters for our test, $\theta_o = 15°$ and $\theta_o = 45°$. We remind the reader that $\theta_e = 45°$ and f_{ellip} represent particles on highly elliptical bound orbits (with $1 - f_{ellip}$ on inflowing/outflowing orbits, as determined by the value of f_{flow}). Therefore, a greater value of f_{ellip} represents a greater fraction of particles on elliptical orbits, rather than radially inflowing/outflowing orbits.

We find that inflowing/outflowing kinematics are able to produce broad-line profiles with smaller values of $\log_{10}(FWHM/\sigma)_{mean}$, i.e., $\log_{10}(FWHM/\sigma) \approx 0.1$–$0.2$. In some cases, even values corresponding to $\log_{10}(FWHM/\sigma) < 0.1$ are produced (see Figures 3.9 and 3.10). These results also validate our previous finding in which flatter structures (e.g., $\theta_o = 15°$) produce broad lines with larger values of $\log_{10}(FWHM/\sigma)_{mean}$, compared to

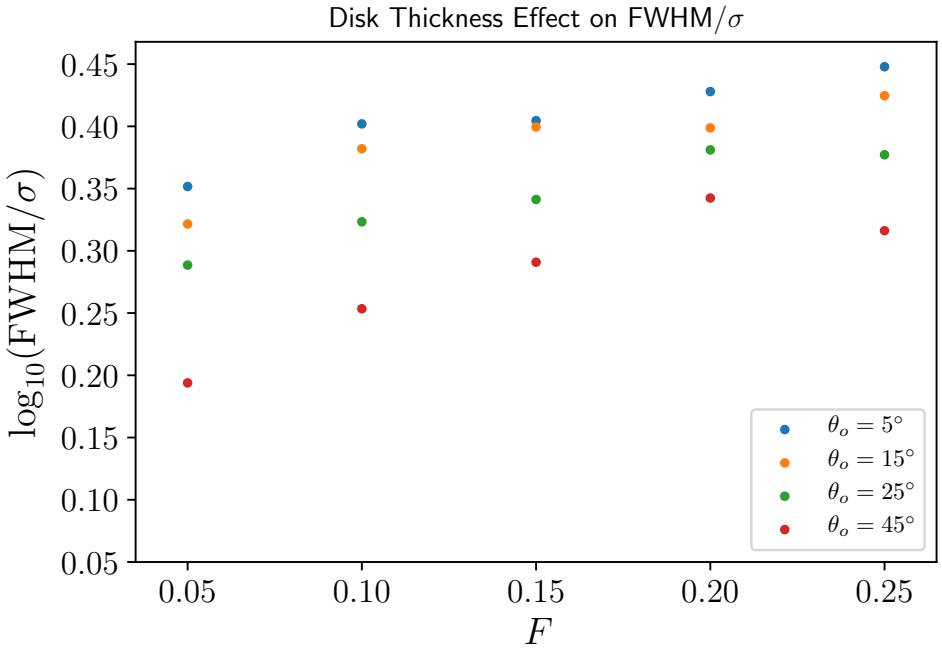

Figure 3.8 We investigate the role of BLR disk thickness in line profile shape using CARAMEL toy models by varying the parameter θ_o and minimum radius F, while holding all other model parameters constant. A mean radius of $\mu = 1$ light-day is used, while minimum radius as defined by F is varied using values $F = 0 - 0.3$, as depicted by the x-axis. Different BLR disk thickness/opening angles, θ_o, are depicted in different colors: $\theta_o = 5°$ is shown in blue, $\theta_o = 15°$ is shown in orange, $\theta_o = 25°$ is shown in green, $\theta_o = 45°$ is shown in red. An opening angle of $\theta_o = 45°$, shown in red, corresponds to a spherical structure and produces broad lines with smaller values of $\log_{10}(FWHM/\sigma)_{mean}$, as expected.

more spherical structures (e.g., $\theta_o = 45°$), which produce broad lines with smaller values of $\log_{10}(FWHM/\sigma)_{mean}$. We also see that $\log_{10}(FWHM/\sigma)$ decreases, with increasing values of f_{ellip}. A value of $f_{ellip} = 0.4$ corresponds to 40% of particles on elliptical orbits, with the remaining 60% on inflowing/outflowing orbits near escape velocity. While a value of $f_{ellip} = 0.9$ corresponds to 90% of particles on elliptical orbits, with the remaining 10% on inflowing/outflowing orbits. This suggests that a combination of inflow/outflow motion and highly elliptical orbits produces broad lines with smaller values of $\log_{10}(FWHM/\sigma)_{mean}$, rather than pure inflow/outflow motion.

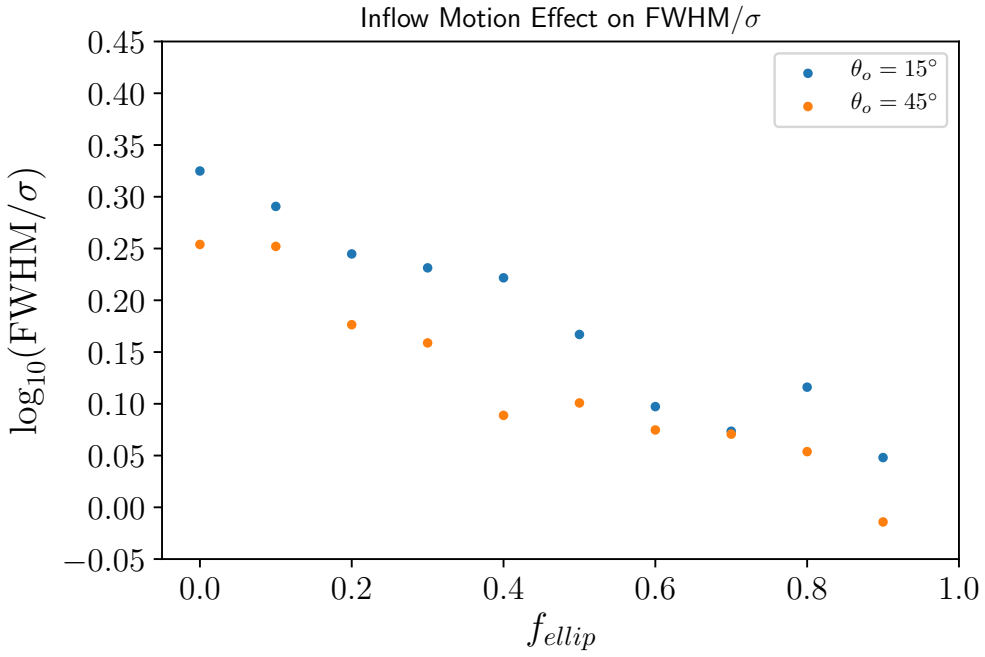

Figure 3.9 Inflow effects on line profile shape. Two different BLR disk thickness/opening angles, θ_o are used. A thick disk with $\theta_o = 15°$ is shown in blue and a spherical structure with $\theta_o = 45°$ is shown in orange. The x-axis, f_{ellip}, represents the fraction of particles on elliptical orbits. Thus an increasing value of f_{ellip} represents a greater percentage of particles on elliptical orbits, rather than on radially inflowing orbits. We see that line profiles with smaller values of $\log_{10}(FWHM/\sigma)_{mean}$ are produced with most of the particles on elliptical orbits with some inflow motion. Additionally, our results reconfirm our finding with thick diskness, a more spherical BLR produces broad lines with smaller values of $\log_{10}(FWHM/\sigma)_{mean}$, and confirm that inflowing BLR motion is able to produce the line profile shapes we are particularly interested in, e.g. $\log_{10}(FWHM/\sigma) < 0.2$.

3.5.4 Turbulent Motion

In addition to inflow/outflow motion, turbulence has also been suggested to cause the extended wings found in a Lorentz profile (Kollatschny & Zetzl, 2013). We test the effect of turbulent motion on line-profile shape using the CARAMEL model parameter σ_{turb}, which allows for macroturbulent velocities. Since the random macroturbulent velocity that is added to the line-of-sight velocity of the particles, depends on both σ_{turb} and $|v_{circ}|$, we test with two different values of $\log_{10}(M_{BH}/M_{\odot})$, as a larger black hole mass would result in greater magnitudes of circular velocity, and thus larger random macroturbulent velocities. Hence,

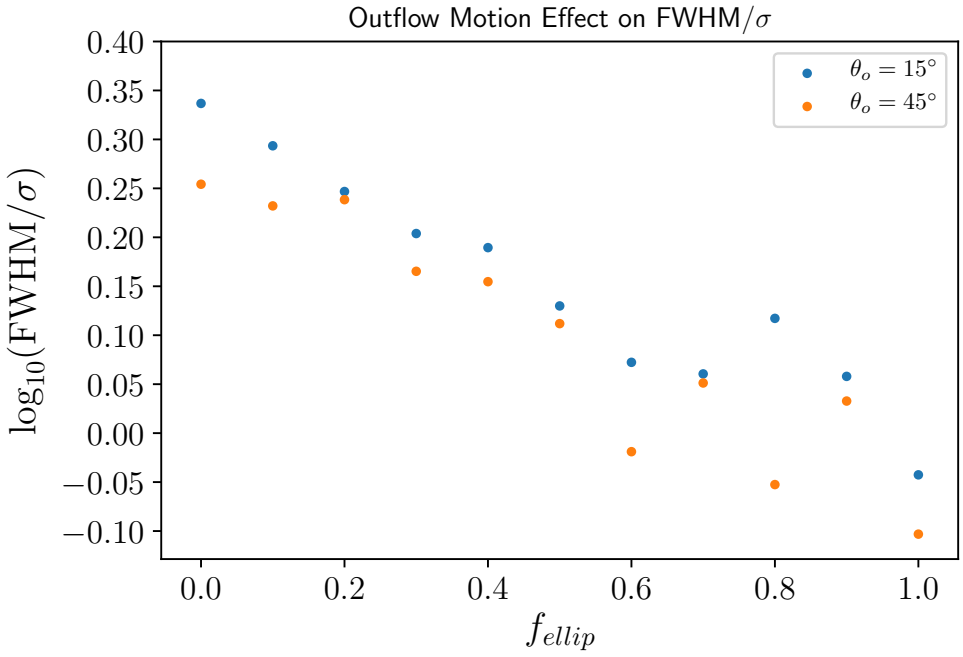

Figure 3.10 Outflow effects on line profile shape. Two different BLR disk thickness/opening angles, θ_o are used. A thick disk with $\theta_o = 15°$ is shown in blue and a spherical structure with $\theta_o = 45°$ is shown in orange. The x-axis, f_{ellip}, represents the fraction of particles on elliptical orbits. Thus an increasing value of f_{ellip} represents a greater percentage of particles on elliptical orbits, rather than on radially outflowing orbits. We see that line profiles with smaller values of $\log_{10}(FWHM/\sigma)_{mean}$ are produced with most of the particles on elliptical orbits with some outflow motion. Additionally, our results reconfirm our finding with thick diskness, a more spherical BLR produces broad lines with smaller values of $\log_{10}(FWHM/\sigma)_{mean}$, and confirm that outflowing BLR motion is able to produce the line profile shapes we are particularly interested in, e.g. $\log_{10}(FWHM/\sigma) < 0.2$.

we expect a more massive black hole, with greater turbulent motion, to have broad lines with smaller values of $\log_{10}(FWHM/\sigma)_{mean}$.

For both scenarios, $\log_{10}(\mathrm{M}_{BH}/M_{\odot}) = 7.0$ and $\log_{10}(\mathrm{M}_{BH}/M_{\odot}) = 8.5$, we set particles on mostly bound outflowing orbits ($\theta_e = 45°$ and $f_{flow} = 0.9$) while varying the σ_{turb} parameter within the limits of its prior, 0.001-0.1. As expected, we find the more massive black hole, $\log_{10}(\mathrm{M}_{BH}/M_{\odot}) = 8.5$, produces broad lines with smaller values of $\log_{10}(FWHM/\sigma)_{mean}$, with increasing macroturbulent contributions (see Figure 3.11).

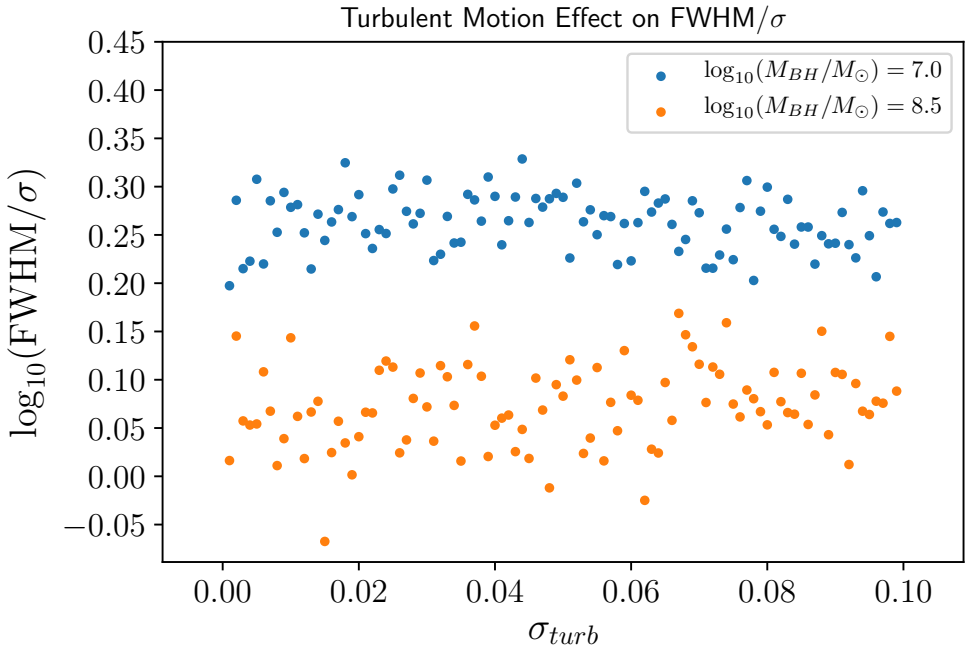

Figure 3.11 We investigate the role of turbulent motion in line profile shape using CARAMEL toy models by varying the parameter σ_{turb}, and holding all other model parameters constant. Since macroturbulent velocities depend on both σ_{turb} and $|v_{circ}| \propto \log_{10}(\mathrm{M}_{BH}/M_\odot)$, we test the effects of turbulent motion using two different black hole masses. The blue points correspond to $\log_{10}(\mathrm{M}_{BH}/M_\odot) = 7.0$ and the orange points correspond to $\log_{10}(\mathrm{M}_{BH}/M_\odot) = 8.5$. As expected, we see the more massive black hole, which represents greater turbulent motion, produces broad lines with smaller values of $\log_{10}(FWHM/\sigma)_{mean}$.

3.6 Conclusions

We use the direct modeling results of a sample of 28 AGNs — nine from LAMP 2016 (V22), seven from LAMP 2011 (W18), four from AGN10 (G17), five from LAMP 2008 (P14), one from AGNSTORM (W20), one from B21, and one from B22. The CARAMEL results of these 28 AGNs provide insight into BLR geometry and kinematics, and constrain M_{BH} measurements without implementing the scale factor f used in reverberation mapping estimates. The cross-correlation time lags and line widths reported by each subsample's respective reverberation mapping paper are employed to determine individual scale factors for each source. Using the extended sample described above, we search for existing correlations

between scale factor and other AGN/BLR parameters/observables. Our main results are as follows.

1. We find 3.4σ evidence for a correlation between $\log_{10}(f_{mean,\sigma})$ and black hole mass.

2. We find 2.8σ marginal evidence for a correlation between $\log_{10}(f_{rms,\sigma})$ and black hole mass.

3. We find 2.1σ marginal evidence for an anti-correlation between $\log_{10}(f_{mean,FWHM})$ and BLR disk thickness.

4. We find 2.4σ marginal evidence for an anti-correlation between $\log_{10}(f_{rms,FWHM})$ and BLR disk thickness.

5. We find 2.6σ marginal evidence for an anti-correlation between $\log_{10}(f_{mean,FWHM})$ and BLR inclination angle.

6. We find 2.4σ marginal evidence for an anti-correlation between $\log_{10}(f_{rms,\sigma})$ and BLR inclination angle.

7. We find 2.0σ marginal evidence for an anti-correlation between $\log_{10}(f_{mean,\sigma})$ and BLR inclination angle.

8. We find 2.2σ marginal evidence for a correlation between line profile shape measured from the rms spectrum, $\log_{10}(FWHM/\sigma)_{rms}$, and $\log_{10}(f_{rms,\sigma})$.

9. We investigate how BLR properties may effect measured line profile shape using CARAMEL models, and find that smaller BLR size, spherical geometries, inflow/outflow motion, and turbulent motion produce broad lines with smaller values of $\log_{10}(FWHM/\sigma)_{mean}$.

10. We conclude that these geometric & kinematic effects cause a larger observed sigma line width (and cuspier FWHM/σ) at fixed M_{BH}, requiring a smaller virial factor, f,

for black hole mass estimators.

The sources modeled by V22 have increased the number of AGNs with dynamical modelling of the BLR by nearly 50%, and led to the discovery of a correlation with the scale factor and line-profile shape. The correlation with line-profile shape may provide an observational proxy for the virial coefficient in the future, however, further CARAMEL studies and a larger sample are needed to confirm the statistical significance of the correlation.

Acknowledgements

We thank the anonymous referee for their helpful comments and suggestions, which significantly improved this manuscript. L.V., P.R.W., and T.T. acknowledge support from the NSF through grant AST-1907208, "Collaborative Research: Establishing the Foundations of Black Hole Mass Measurements of AGN across Cosmic Time."

Research at UC Irvine has been supported by NSF grants AST-1907290. V.U acknowledges funding support from the University of California Riverside's Chancellor's Postdoctoral Fellowship and NASA Astrophysics Data Analysis Program Grant #80NSSC20K0450. T.T. acknowledges support by the Packard Foundation through a Packard research fellowship. V.N.B. gratefully acknowledges assistance from NSF Research at Undergraduate Institutions (RUI) grants AST-1312296 and AST-1909297. Note that findings and conclusions do not necessarily represent views of the NSF. D.C.L.'s group at San Diego State University gratefully acknowledges support from the NSF through grants AST-1210311 and AST-2010001.

M.C.B. gratefully acknowledges support from the NSF through grant AST-2009230. G.C. acknowledges NSF support under grant AST-1817233. J.H.W. acknowledges funding from the Basic Science Research Program through the National Research Foundation of Korean Government (NRF-2021R1A2C3008486). A.V.F.'s group at U.C. Berkeley is grateful for support from the TABASGO Foundation, the Christopher R. Redlich Fund, the Miller In-

stitute for Basic Research in Science (in which he was a Miller Senior Fellow), and many individual donors. We acknowledge the generous support of Marc J. Staley, whose fellowship partly funded B.E.S. whilst contributing to the work presented here in as a graduate student.

This research has made use of the NASA/IPAC Extragalactic Database (NED), which is operated by the Jet Propulsion Laboratory, California Institute of Technology, under contract with the National Aeronautics and Space Administration.

3.7 Appendix

3.7.1 CARAMEL code modifications

The minor modifications made to the original CARAMEL code, after its use by W18, G17, P14, W20, B21, and B22, (and prior to the use by V22) are outlined in the Appendix of Williams & Treu (2022). Here we summarize the content found in Williams & Treu (2022).

The original CARAMEL model used by W18, G17, P14, W20, B21, and B22 first draws the particles' radii from a shifted gamma distribution as described in the text. Then the particles are placed on the positive x-axis and each particle is rotated around the z-axis, by an angle drawn from a uniform distribution between 0 and 2π. The particles are then rotated about the y-axis, by an angle drawn from the following distribution: $\arccos\left(\cos\theta_o + (1 - \cos\theta_o) \times U^{\gamma}\right)$, where θ_o determines the opening angle (disk thickness) of the BLR and U is a uniform distribution defined between 0 and 1. Additionally, in this original version of the code, γ is allowed to range from 1 to 5. Upon this second rotation, the particles are rotated twice more — once about the z-axis by an angle drawn from a uniform distribution between 0 and 2π (which creates the thick disk), and once more about the y-axis by an angle defined by $\pi - \theta_i$.

Prior to the CARAMEL modeling of the LAMP 2016 sample, our team discovered that the second rotation about the z-axis redacted the effect of γ and modified the CARAMEL code

to allow for the effects of γ. The modified version of CARAMEL used by V22 varies from the placement of particles from the shifted gamma distribution. Rather than place all particles on the positive x-axis as described above, particles are placed on both positive and negative sides of the x-axis. Then the particles are only rotated a total of three times, rather than four. The first rotation is about the y-axis, rather than the z-axis, and is defined by an angle drawn from the following distribution: $\arcsin\left(\sin\theta_o \times U^{1/\gamma}\right)$, which creates a double wedge in the xz plane. After the first rotation, the particles are then rotated about the z-axis by an angle drawn from a uniform distribution between 0 and 2π (which creates a thick disk). Then, the particles are rotated by one final rotation about the y-axis by an angle defined by $\pi - \theta_i$.

After the changes made in geometric construction, we noticed that most of the effects of γ occur within the ranges $\gamma = 1$–2, and changed the priors on the parameter accordingly.

CHAPTER 4

Empirical models of the Hβ broad emission line gas density field

This chapter has been accepted for publication as Villafaña, L., Treu, T., Colleyn, L., et al.; "Empirical models of the Hβ broad emission line gas density field," ApJ, 966, 106 (2024), and is reproduced here with minor formatting adjustments

4.1 Introduction

While the Standard Model of Active Galactic Nuclei (AGN) provides a well-developed framework that explains the different AGN features observed (Antonucci, 1993; Urry & Padovani, 1995; Urry, 2003), details of the different components, such as the structure and dynamics, still remain uncertain (for a review, see Netzer, 2015). Understanding the structure and behavior of gas near the vicinity of the central engine is of great interest, as such insight may help us better understand the role AGN play in galaxy evolution (Booth & Schaye, 2009; Fabian, 2012; Somerville & Davé, 2015; Dubois et al., 2016). Given that the broad emission line region (BLR) is the closest structure, of order of $\sim$ light-days for low luminosity AGNs (Kaspi et al., 2000), to the central black hole, the BLR has been the focus of a wide range of AGN astrophysics studies.

From a theoretical standpoint, several scenarios of the BLR gas have been proposed, ranging from discrete clouds (Krolik, 1988; Rees et al., 1989; Baldwin et al., 1995), to bloated stars

(Scoville & Norman, 1988) and comets (Maiolino et al., 2010), to perhaps the most recently favored, disk winds (Emmering et al., 1992; Murray et al., 1995; Elvis et al., 2002) (for a review, see Peterson, 2006, and references therein). From an observational standpoint, the BLR cannot be spatially resolved and most information known about the BLR involves resolving the BLR in time using the technique of reverberation mapping (but see, however, Gravity Collaboration et al., 2018, 2020, 2021, for recent breakthroughs through the use of interferometry).

Reverberation mapping campaigns involve intensive photometric and spectroscopic observations over the course of several months, in order to observe variations in the ionizing continuum reverberate as variations in the broad emission line fluxes at a later time, τ (Blandford & McKee 1982; Peterson 1993; Peterson et al. 2004 and for a more recent review, see Cackett et al. 2021). This technique has proven very valuable in calibrating over 70 AGN black hole masses (see, Bentz & Katz, 2015a, for details regarding their online AGN black hole mass database).

In principle, one can map how changes in the continuum translate to changes in the broad emission line fluxes as a function of line-of-sight (LOS) velocity and time delay, i.e the transfer function, to learn more about the structure and kinematics of the BLR (Peterson, 1993), although interpretation is not straightforward and requires additional modeling (Horne, 1994; Cackett & Horne, 2006). As an alternative approach, our team pioneered the method of forward modeling reverberation mapping data sets using the Code for AGN Reverberation and Modeling of Emission Lines (CARAMEL). The BLR Reverberation-mapping Analysis In AGNs with Nested Sampling (BRAINS) code by Li et al. (2013) also follows a similar forward modeling approach, and the Broad Emission Line Mapping Code (BELMAC) by Rosborough et al. (2023) may be modified in the near future to include forward modeling capabilities.

Using high-quality reverberation mapping data sets, we have modeled the BLR *emission*

for over 28 AGN (Pancoast et al., 2014; Grier et al., 2017; Williams et al., 2018, 2020; Villafaña et al., 2022; Bentz et al., 2021, 2022, 2023a,b). While this original version of the code sufficiently models various aspects of BLR geometry and kinematics, e.g., disk inclination, disk thickness, inflow/outflow behavior, the BLR is modeled as a collection of point particles near a central ionizing source which instantaneously re-emit absorbed power. For this reason, CARAMEL only models the emissivity distribution, rather than the actual underlying gas distribution, and we interpret the BLR model as a Monte Carlo representation of the emissivity field. We will refer to this original version of the code, which models the BLR emissivity field, as CARAMEL-LIGHT throughout the rest of the paper.

Williams & Treu (2022, hereafter W22) modified CARAMEL-LIGHT to include a simple power law that connects the observed BLR emission to the underlying gas distribution, in a version of the code we now call CARAMEL-GAS. In this way, CARAMEL-GAS models the BLR as a Monte Carlo representation of the gas density field, rather than the emissivity field. A representation of the gas density field would prove to be an advantage for fitting multiple emission lines at once, e.g., Hα and Hβ or C3 and C4. With the current version of the code, however, emission lines must be modeled individually and can only be compared a posteriori (Williams et al., 2020; Williams & Treu, 2022). Future development to incorporate the ability to model multiple emission lines requires additional testing and understanding of the capabilities of CARAMEL-GAS — which is the focus of this paper.

The resulting gas density field produced by CARAMEL-GAS can be interpreted through the lens of different theoretical scenarios, such as BLR clouds or a continuous disk wind structure. While we believe more recent developments in the theory may be pointing towards the latter (Waters et al., 2016; Mangham et al., 2017; Waters & Li, 2019), we will often refer to the BLR as "clouds" throughout this paper, for the sake of our argument as we consider all possible interpretations. Therefore, we want to emphasize that our use of this terminology does *not* mean the BLR cloud model is our preferred interpretation. In particular, we would

like the reader to keep in mind that CARAMEL-GAS models the BLR gas as a Monte Carlo representation of the gas density field, and although we may often refer to the BLR as discrete clouds, this is only one possible interpretation which we include for completeness.

Our work builds upon the initial development and testing stage of CARAMEL-GAS, in which W22 found the emissivity power law index, α — the new model parameter that relates observed emission to the gas distribution — pushing up against its prior of -2 to 0, suggesting a preference for positive values. W22 speculated whether the assumption of point particles, which are used to represent the gas density field, with equal emitting size contributed to these results. Using the interpretation of discrete clouds and pressure law models (Rees et al., 1989), W22 proposed including an additional radial power law index, α_{size}, that allows for varying size(s) of the BLR structure/clouds as a function of radial distance from the central black hole. In this paper, we use a sample of ten AGN to further validate the CARAMEL-GAS code and test a new general form of the radial power law index, which includes both an emissivity power law index and a size power law index for the BLR structure/clouds.

We outline our sample selection in Section 4.2 and briefly summarize CARAMEL-LIGHT, the first implementation of CARAMEL-GAS, and the additional modifications applied to CARAMEL-GAS for this work in Section 4.3. We present our results and discuss possible interpretations of a positive power law index, α, in Section 4.4, and conclude in Section 4.5.

4.2 Sample Selection

Due to the computational power required for any CARAMEL modeling, we choose to limit the number of AGN to model using CARAMEL-GAS. While a total of at least 28 AGN have been modeled using CARAMEL-LIGHT (see Villafaña et al., 2022, for a recent list), we use only those observed during the Lick AGN Monitoring Project (LAMP) campaigns — LAMP 2008 (Bentz et al., 2009; Walsh et al., 2009), LAMP 2011 (Barth et al., 2011a, 2015a), and LAMP2016 (U et al., 2022) — due to homogeneous data reduction and analyses.

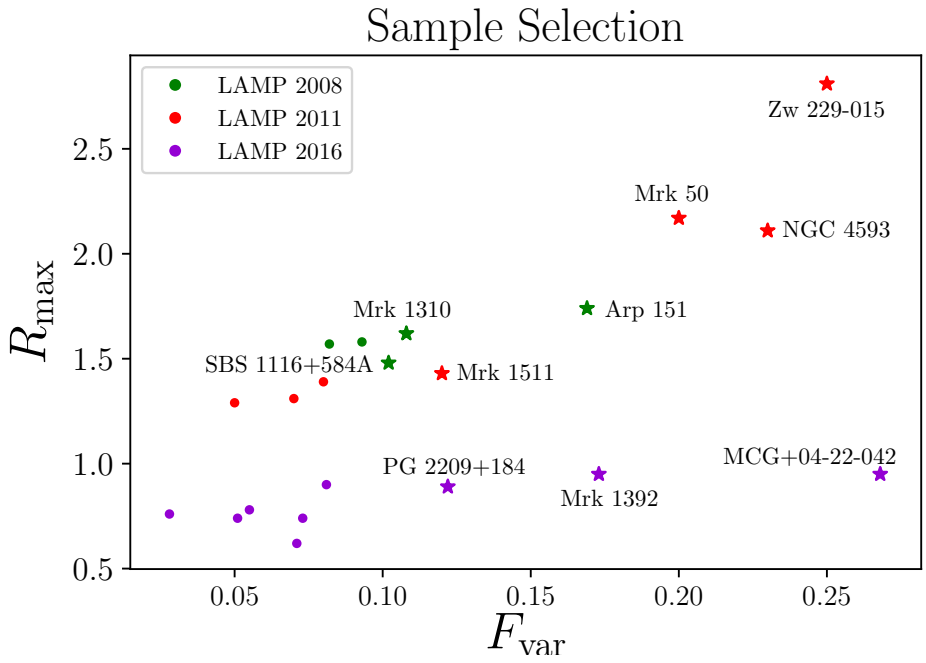

Figure 4.1 We select our sample from data collected during the three observation campaigns: LAMP 2008 (shown in green), LAMP2011 (shown in red), and LAMP 2016 (shown in purple). We compare the Hβ variability statistics R_{max} and F_{var} to select our sample. The AGN shown in the plot above represent only the 21 LAMP AGN that have successful CARAMEL-LIGHT modeling. More AGN were observed during each campaign, but we do not include those with insufficient data quality for CARAMEL modeling. Our selection criteria requires $F_{var} \geq 0.1$ and $R_{max} \geq 0.4$. In total, we select 10 AGN for CARAMEL-GAS modeling, which are depicted with a star marker above.

In order to determine the sample of AGN to model using CARAMEL-GAS, we use two Hβ variability statistics that are standard in reverberation mapping analyses, F_{var} and R_{max}. The variability statistic R_{max} refers to the ratio of maximum to minimum flux, and the noise-corrected fractional variation, F_{var} is computed as:

$$F_{var} = \frac{\sqrt{\sigma^2 - \delta^2}}{\langle F \rangle} \tag{4.1}$$

where σ^2 is the variance of the fluxes, δ^2 is their mean square uncertainty, and $\langle F \rangle$ is the mean flux.

We compile the variability statistics from the original reverberation mapping analyses of our sample and tabulate them in Table 4.1. To focus on objects having high-quality reverberation mapping data, we select targets from LAMP campaigns that exhibited fractional variability amplitude $F_{var} \geq 0.1$ and ratio of maximum to minimum flux $R_{max} \geq 0.4$ in the integrated Hβ light curves (see Figure 4.1). While the quality of reverberation mapping data additionally depends on light curve cadence, duration, and S/N, these variability criteria effectively reject the LAMP datasets with lower variability amplitudes that are not suitable for velocity-resolved line profile modeling. We note that Mrk 50 (LAMP 2011), NGC 4593 (LAMP 2011), and Arp 151 (LAMP 2008) were previously modeled with CARAMEL-GAS during the initial development and testing done by W22. However, we include these three AGN in our sample since one of our goals is to test a more generalized radial power law index, α, and these three AGN were modeled during the CARAMEL-GAS development phase using the original parameter α, which did not include a radial power law index for the reflecting surface area(s) of the BLR structure/clouds (please see Section 4.3 for a further discussion).

For our selected sample, we use the spectral decompositions originally used for CARAMEL-LIGHT and model the same wavelength ranges (see Table 4.2) for each AGN. For details regarding the spectral decompositions of the reverberation mapping data sets, we refer the reader to the original CARAMEL-LIGHT work of a given AGN, which can also be found in Table 4.2. The spectra used for the original CARAMEL-LIGHT modeling have flux or magnitude units. As we will discuss later in Section 4.3.5, CARAMEL-LIGHT does not fit absolute fluxes and instead includes a scaling factor to match the continuum and emission line strengths. In CARAMEL-GAS, we fit the absolute fluxes by scaling the continuum light curves and emission lines to luminosity units using the luminosity distances found in Table 4.2. Conversion of spectral units required for CARAMEL-GAS modeling will be further discussed in Section 4.3.

Table 4.1. LAMP AGN Hβ Variability Statistics

Campaign & corresponding CARAMEL-LIGHT	Galaxy	Redshift	F_{var}	R_{max}	Selected?
Lick AGN Monitoring Project (LAMP 2008; Pancoast et al., 2014, hereafter P14)	Arp 151	0.02109	0.169 [a]	1.74 ±0.04 [a]	Yes*
	Mrk 1310	0.01941	0.108 [a]	1.62 ± 0.04 [a]	Yes
	NGC 5548	0.01718	0.082 [a]	1.57 ±0.35 [a]	No
	NGC 6814	0.00521	0.093 [a]	1.58 ±0.11 [a]	No
	SBS 1116+583A	0.02787	0.102 [a]	1.48±0.06 [a]	Yes
Lick AGN Monitoring Project (LAMP 2011; Williams et al., 2018, hereafter W18)	Mrk 141	0.04170	0.080[b]	1.39±0.03[b]	No
	Mrk 1511	0.03390	0.120[b]	1.42±0.03 [b]	Yes*
	Mrk 279	0.03050	0.070 [b]	1.31±0.01 [b]	No
	Mrk 50	0.02340	0.200 [b]	2.17±0.13 [b]	Yes*
	NGC 4593	0.00900	0.230 [b]	2.11±0.08 [b]	Yes
	PG 1310-108	0.03430	0.050 [b]	1.29 ±0.02 [b]	No
	Zw 229-015	0.02790	0.250 [b]	2.81±0.07 [b]	Yes
Lick AGN Monitoring Project (LAMP 2016; Villafaña et al., 2022, hereafter V22)	MCG +04-22-042	0.03235	0.268 [c]	0.95 [c]	Yes
	Mrk 1048	0.04314	0.071 [c]	0.62 [c]	No
	Mrk 1392	0.03614	0.173 [c]	0.95[c]	Yes
	Mrk 841	0.03642	0.073 [c]	0.74 [c]	No
	NPM1G+27.0587	0.06200	0.051[c]	0.74 [c]	No
	PG 2209+184	0.07000	0.122[c]	0.89 [c]	Yes
	RBS 1303	0.04179	0.081 [c]	0.90[c]	No
	RBS 1917	0.06600	0.028 [c]	0.76[c]	No
	RXJ 2044.0+2833	0.05000	0.055 [c]	0.78 [c]	No

Note. — We select our sample for this work from the sources modeled with CARAMEL-LIGHT from the three different LAMP campaigns — LAMP 2008, LAMP 2011, LAMP 2016. Column 1 specifies the campaign from which the data were collected and the corresponding CARAMEL-LIGHT paper. The galaxy name and redshifts are found in Columns 2 and 3, respectively. Redshifts are from NASA/IPAC Extragalactic Database (NED). The Hβ variability statistics — noise-corrected fractional variation, F_{var} and the ratio of maximum to minimum flux, R_{max} — are found in Columns 4 and 5, respectively. References for the Hβ variability statistics are as follows: (a)Bentz et al. (2009), (b) Barth et al. (2015a), (c) U et al. (2022). We require $F_{var} > 0.1$ and $R_{max} > 0.4$ when selecting our sample. Column 6 shows whether the AGN was selected for our sample or not. Yes* signifies that the AGN selected has previously been modeled using CARAMEL-GAS, during the initial implementation and testing phase (Williams & Treu, 2022).

4.3 The Model

We begin with a brief description of the original CARAMEL-LIGHT model, followed by the modifications implemented by W22 to create CARAMEL-GAS. We then discuss additional modifications made to CARAMEL-GAS in this work and the modeling details for the ten AGN presented here, as well as the model degeneracies we might expect to find with CARAMEL-GAS.

4.3.1 Overview of CARAMEL-LIGHT

For a full overview of CARAMEL-LIGHT, please see Pancoast et al. (2014). In summary, CARAMEL-LIGHT models the BLR *emission* by sampling a distribution of point particles surrounding a central black hole located at the origin. The model assumes the central engine (the black hole) is the ionizing source and that the BLR particles instantaneously reprocess and re-emit the model continuum.In this way, the particles represent a Monte Carlo realization of the emissivity field, rather than the actual BLR gas distribution.

Utilizing a Bayesian framework, CARAMEL-LIGHT uses a diffusive nested sampling code, DNEST4 (Brewer & Foreman-Mackey, 2018), to explore a 27-parameter space and infer the model parameters that best fit the reverberation mapping data set. To account for systematic uncertainty from using a simple model, DNEST4 uses a statistical temperature, T, to weigh the likelihood when calculating the posterior, i.e $\log(posterior) \propto \log(prior) + \log(likelihood)/T$. The use of this likelihood softening parameter, T, corresponds to inflating the error bars by $\sqrt{T}$, and the value of T, is selected post-analysis such that parameters converge in a smooth and unimodal fashion (Bentz et al., 2021).

We note two potential limitations with this simplified model. First, disk-outflow models suggest that the BLR and the obscuring torus may form one continuous structure that feeds/flows from the central accretion disk (e.g., Emmering et al., 1992; Konigl & Kartje, 1994; Kartje & Königl, 1996; Kishimoto et al., 2011; Koshida, 2015). Since we model the

central engine as the ionizing source, our model is incompatible with disk-outflow models and cannot provide information about the accretion disk. Additionally, we assume gravity is the dominant force and do not take into account radiation pressure. This can lead to biased results for sources with high Eddington ratio AGNs. However, LAMP sources have been found to have moderate Eddington ratios in prior studies (Villafaña et al., 2022).

4.3.1.1 Modeling the Emission Line

In principle, any broad emission line can be used for modeling Here we model only the Hβ emission line for our sample of low-redshift galaxies. We note that our team's primary future goal with the development and testing of CARAMEL-GAS is to model multiple emission lines simultaneously, for a given object. In particular, we would like to model the full extent of the BLR at once, using physically motivated emissivity profiles for different emission lines that originate from different BLR radial zones. Current reverberation mapping data sets that cover multiple emission lines include NGC 5548 (De Rosa et al., 2015) and Mrk 817 (Kara et al., 2021). [1] To realize our goal of modeling multiple emission lines simultaneously, however, additional testing of CARAMEL-GAS is required first — which is the focus of this paper.

In addition to data regarding the emission line being modeled, CARAMEL-LIGHT utilizes the V/B band continuum light curve measured from the photometric campaign since it serves as a proxy for the ionizing continuum. CARAMEL-LIGHT uses Gaussian processes to model the continuum light curve, in order to interpolate between data points and evaluate the flux of the ionizing source at any arbitrary time. This allows the emission line, which echoes the variations of the ionizing source, to be modeled at any arbitrary time using the BLR particle distribution determined by the CARAMEL-LIGHT model parameters.

[1]For comparison of NGC 5548 Lyα, Hβ , and C4 CARAMEL-LIGHT BLR models, done a posteriori, see Williams et al. (2020)

The radial distribution of the particles around the central source is described by a shifted gamma distribution, and a change of variables is computed so that the radial distribution is described by the model parameters μ, β, and F. The parameter μ represents the mean value of the shifted gamma distribution, the parameter β represents the standard deviation of the shifted gamma distribution, and the parameter F represents the fraction of μ from the origin where the shifted gamma distribution begins. In addition to these three parameters, the radial distance, r_i, of a particle is also defined by the Schwarzchild radius, which determines the lower limit for particle positions as measured from the central black hole. The effects of the model parameters μ and β on the radial distribution of particles will be further discussed in a following subsection, Section 4.3.6.

Once the particles are placed around the central black hole, according to the shifted gamma distribution and model parameters μ, β and F described above, the particle position determines the time lag of the particle, τ_i, or how long the particle takes to reverberate variations in the continuum. Assuming observed time delays are due to light travel time, as done with traditional reverberation mapping analyses, the value of τ_i simply corresponds to the particle's distance from the origin divided by the speed of light, $\tau_i = r_i/c$. Then, for a given particle i, the line-of-sight velocity determines the wavelength emitted, i.e. how much it is shifted from the rest wavelength of the emission line.

The model then determines the amplitude of the emission line using the amplitude, $C(t-\tau_i)$, of the continuum light curve at a time $t-\tau_i$ and allows for additional rescaling of the emission line amplitude via model parameters ξ, κ, C_{mult}, and C_{add}. The parameter ξ describes the BLR midplane transparency and represents the fraction of particles emitting from the "far" side of the BLR and ranges from 0 to 1. The parameter κ ranges from -0.5 to 0.5 and is related to the relative brightness of each particle. The emission of each particle is weighted by $W = 0.5 + \kappa\cos(\phi)$, where ϕ is the angle between the particle's line of sight to the origin (ionizing source) and the observer's line of sight to the origin. Positive values of

κ represent preferential emission away from the ionizing source and negative values of κ represent preferential emission towards the ionizing source.

To understand the free parameters C_{mult}, and C_{add}, it is important to note that the absolute fluxes of both the continuum and the emission line are not modeled in CARAMEL-LIGHT. Instead, the fluxes are rescaled so that they are in units of order unity. Since the continuum fluxes used in the model are not absolute, the free parameters C_{mult}, and C_{add} are multiplicative and additive factors included to match the overall amplitude (via C_{mult}) and amplitude of variations (via C_{add}) of the data. Combining all these factors, the line emission for a particle i, at time t is calculated in the model using the following equation:

$$L_i(t) = W(\xi, \phi_i, \kappa) C_{mult}[C(t - \tau_i) + C_{add}] \tag{4.2}$$

where $L_i(t)$ is the line emission of particle i at time t, $C(t)$ is the observed continuum at time t, $C(t - \tau_i)$ is the observed continuum that arrives at the particle at time t given its distance and associated time lag τ_i, C_{mult} is the multiplicative factor included to match the overall amplitude of the data, C_{add} is the additive factor included to match the amplitude of variations of the data, and $W(\xi, \phi_i, \kappa)$ is a weighting function determined by the model parameters ξ and κ.

Once the amplitude of the emission line emitted by each particle is determined using Equation 4.2 above, the wavelength of the emission line emitted from each particle is determined by the particle's line-of-sight velocity. The total emission line is then found by summing the contribution from each particle.

Finally, to account for instrumental resolution, we blur the spectrum by $\Delta\lambda_{dis}$ which is calibrated using the [O3] λ5007 line. Since the [O3] line is expected to remain constant for much longer time scales (Peterson et al., 2013), we assume the differences in observed [O3] line widths must be due to small changes in observing and instrumental conditions. For this

reason, we also include the observed [O3] emission line data in our model and calculate the instrumental resolution, $\Delta\lambda_{dis}$ by subtracting the intrinsic [O3] line width, $\Delta\lambda_{true}$, from the observed λ5007 line [O3] line width, $\Delta\lambda_{obs}$, in quadrature:

$$\Delta\lambda_{dis}^2 \approx \Delta\lambda_{obs}^2 - \Delta\lambda_{true}^2 \tag{4.3}$$

Finally, we note that the description we have outlined above assumes that the response of the emission line to variations optical continuum can be approximated as linear around the mean (W22).

4.3.2 Development of CARAMEL-GAS

The goal of CARAMEL-GAS is to model the BLR gas distribution by including a description of how the gas translates to emission. In general, one could calculate emissivity using photoionization codes such as CLOUDY (Ferland et al., 1998). However, in practice, this complexity would increase the computational power required and CARAMEL-LIGHT already takes an average of at least two weeks to run on supercomputers, per object. Instead, we opt for a simple approximation and describe the BLR surface emissivity, power emitted per unit surface area, as a power law in radial distance, r:

$$\tilde{\epsilon}(r) = \tilde{\epsilon}_0(r/r_0)^{\alpha} \tag{4.4}$$

where r represents the BLR radial distance from the central source and $\tilde{\epsilon}(r_0) = \tilde{\epsilon}_0$ is a normalization constant, representing the surface emissivity at a pivot radius r_0 (Robinson, 1995; Goad et al., 2012).

In terms of ionizing flux, Equation 4.4 can be rewritten as:

$$\tilde{\epsilon}(\Phi) = \tilde{\epsilon}_0(\Phi/\Phi_0)^{-\alpha/2} \tag{4.5}$$

To calculate the emission line luminosity of particle i from the emissivity (erg s^{-1} cm^{-2}), we assign an emitting size, $A_{c,i}$ to each particle:

$$L_{line,i}(\lambda) = \tilde{\epsilon}_0(\Phi_i/\Phi_0)^{-\alpha/2} A_{c,i}\delta(\lambda - \lambda_i) \tag{4.6}$$

where Φ_i is the ionizing flux at the position of particle i. We use a Dirac delta function, $\delta(\lambda - \lambda_i)$ to denote the wavelength on the emission line, since the wavelength of the line emission will be determined by the particle's line-of-sight velocity.

Since the ionizing flux is not constant, it can be written as a function of time and the observed continuum, such that:

$$\Phi_i = \Phi_i(t) = L_{ion}(t - \tau_i)/4\pi r_i^2 \tag{4.7}$$

where $L_{ion}(t)$ is the luminosity of the ionizing continuum at time t, $L_{ion}(t - \tau_i)$ is the luminosity of the ionizing continuum that arrives at the particle i at time t given its distance to the ionizing source and associated time delay, τ_i, and r_i is the radial distance from the central black hole of particle i, which is determined by the model parameters μ and β.

Combining Equations 4.6 and 4.7, the observed line emission luminosity can be written as:

$$L_{line}(\lambda, t) = \sum_{i=0}^{N} \tilde{\epsilon}_0 \left[\frac{L_{ion}(t - \tau_i)/4\pi r_i^2}{L_{ion,0}/4\pi r_0^2} \right]^{-\alpha/2} A_{c,i}\delta(\lambda - \lambda_i) \tag{4.8}$$

where N represents the number of BLR particles surrounding the central source, and the total line emission, $L_{line}(\lambda, t)$, is equal to the sum of the particles' individual line emission. The

wavelength, λ, re-emitted by particle i is determined by the particle's line-of-sight velocity and the wavelength of the emission line being modeled. The variable r_i is the radial distance from the central black hole of particle i, which is determined by the model parameters μ and β, first introduced in Equation 4.7, and the variable r_0 is the pivot radius first introduced in Equation 4.4.

In the initial framework and testing of CARAMEL-GAS done by W22, we assume all the particles are the same size and define $\epsilon_0 = \tilde{\epsilon}_0 A_c$. We note that we are simply summarizing the initial framework of CARAMEL-GAS here and will be modifying this assumption in Section 4.3.4 for our sample of 10 AGN.

Equation 4.8 simplifies to:

$$L_{line}(\lambda, t) = \epsilon_0 \sum_{i=0}^{N} \left[\frac{L_{ion}(t - \tau_i)}{L_{ion,0}} \right]^{-\alpha/2} \left[\frac{r_i}{r_0} \right]^{\alpha} \delta(\lambda - \lambda_i) \tag{4.9}$$

As with CARAMEL-LIGHT, we assume that the BLR response can be approximated as linear around the mean, and keep the additive offset, C_{add} to allow the model to match the amplitude of variations in the data. We also use the observed V/B continuum, $L_{obs}(t)$, as a proxy for the ionizing continuum, $L_{ion}(t)$. The emission of each particle is also weighted in the same manner as CARAMEL-LIGHT using the weighting factor $W(\xi, \phi_i, \kappa)$ so that the line emission at a given wavelength and time t corresponds to:

$$L_{line}(\lambda, t) = \epsilon_0 \sum_{i=0}^{N} \left[\frac{L_{obs}(t - \tau_i) + C_{add}}{L_{obs,0} + C_{add}} \right] \left[\frac{r_i}{r_0} \right]^{\alpha} \times W(\xi, \phi_i, \kappa) \delta(\lambda - \lambda_i) \tag{4.10}$$

where $L_{obs,0}$ is the mean V/B band continuum luminosity observed, and $L_{obs}(t - \tau_i)$ is the observed V/B continuum luminosity that arrives at a particle at time t given its distance, and associated time lag τ_i. The power emitted per unit surface area scales with radial distance from the black hole, r_i, and is determined by the CARAMEL-GAS model parameter, α, which

was first introduced in Equation 4.4.

To minimize covariance, we set the pivot radius, r_0 to the BLR size determined from cross-correlation measurements and the observed luminosity, $L_{obs,0}$, to the mean continuum luminosity of the campaign. We note that we have removed the multiplicative parameter, C_{mult}, in the scaling of the line emission since the data used for CARAMEL-GAS is given in luminosity units, rather than the arbitrary fluxes used for CARAMEL-LIGHT modeling.

In summary, the total line emission luminosity is found by summing the contribution of all the particles (Equation 4.10), which we have assumed have the same size, and the wavelength of the emission is determined by the particle's line-of-sight velocity. Similar to CARAMEL-LIGHT, we include the observed [O3] λ5007 emission line in our model to calculate instrumental resolution and blur the simulated emission line profile by Δ_{dis} (as shown in Equation 4.3).

The rest of the CARAMEL geometry and kinematic parameters remain the same, only C_{mult} has been removed, and ϵ_0 and α have been added. Thus CARAMEL-GAS explores a 28 parameter space, rather than 27 as done in CARAMEL-LIGHT. Here the parameter ϵ_0 represents the emissivity power-law normalization and the parameter α represents the emissivity power-law index originally introduced in Equation 4.4.

In addition to the slight change in parameter space, another key difference between the two versions of CARAMEL presented here is that the absolute continuum and spectral fluxes are not modeled in CARAMEL-LIGHT, and instead, the fluxes are rescaled so they are in units of order unity. In CARAMEL-GAS, we fit the absolute flux scale of the observed emission lines by ensuring the input continuum light curves and emission lines are in luminosity units (see Section 4.3.5 for further details).

4.3.3 Relevant CARAMEL model parameters

As mentioned above, both versions of CARAMEL have over 25 parameters. In addition to the parameters described above in weighting the broad emission line flux via the transparency of the BLR mid-plane, ξ, and an illumination function, κ, there are other model parameters that provide insight into the geometry and kinematics of the BLR that we would like to highlight here.

A key parameter with any CARAMEL work is the black hole mass constraint given by the model parameter, $\log(M_{bh}/M_{\odot})$. The geometry of the BLR is then given by the inclination angle of the BLR disk, θ_i, and the opening angle (disk thickness), θ_o. In regards to BLR kinematics, we determine the fraction of particles with elliptical orbits via the model parameter f_{ellip}, and $1 - f_{ellip}$ represents the fraction of particles in either inflowing/outflowing orbits. The parameter f_{flow} ranges from 0 to 1 and determines whether the remaining $1 - f_{ellip}$ particles are inflowing/outflowing, with values $f_{flow} < 0.5$ indicating inflow and values $f_{flow} > 0.5$ indicating outflow.

For the purposes of this work, we do not focus on the geometric and kinematic properties of the BLR as they have all been fully studied in their original CARAMEL-LIGHT studies. For a full review of the BLR geometry and kinematics of each AGN presented in this work, please see their respective CARAMEL-LIGHT paper found in Table 4.1. Here, we are more interested in understanding the BLR gas distribution and further validating the CARAMEL-GAS code. In the following subsection, we describe the minor changes made to CARAMEL-GAS in this work and the testing we will focus on.

4.3.4 Modifications to CARAMEL-GAS

We note that in our current stages of development, one could in principle re-parameterize CARAMEL-GAS results to produce CARAMEL-LIGHT results. However, we would like to emphasize that our team's ultimate goal in developing CARAMEL-GAS is to model multiple

emission lines simultaneously. Since CARAMEL-LIGHT models the BLR as a Monte Carlo representation of the emissivity field, modeling the BLR of two emission lines does not provide insight to the underlying gas distribution that produces the emission lines. To fit multiple emission lines arising from the same species, i.e. Hα and Hβ, the code must be able to model the BLR as a Monte Carlo representation of the gas density field, which requires additional assumptions about the BLR gas emissivity properties. In this paper, we seek to further test the power law (Equation 4.4) implemented in the first version of CARAMEL-GAS, as a step toward modeling the BLR gas distribution with multiple BLR emission lines.

In our initial development and testing of CARAMEL-GAS, we defined a uniform prior for the parameter α, set between values of -2 and 0 (W22). This informed prior was based on the photoionization calculations Goad et al. (2012) computed using CLOUDY models for simple slabs of gas, and found $\alpha \sim -1$ for the Hβ emission line. Additionally, we assumed that the BLR particles are all the same size and defined $\epsilon_0 = \tilde{\epsilon}_0 A_c$.

However, of the four emission lines (from three AGN) W22 modeled, CARAMEL-GAS was unable to constrain the parameter α for one, and the rest of the three were found to push up against their prior, i.e. preferred less negative solutions. As suggested by W22, pressure models often describe the sizes of BLR clouds as a power law in radial distance from the ionizing source, $A_c(r) \propto r^{\alpha_{size}}$, with $\alpha_{size} \sim 0$ to 1.5. (Rees et al., 1989) If we remove our previous assumption in which all BLR particles are the same size, we can consider a more general power law, $\epsilon(r) \propto r^{\alpha}$, such that $\alpha = \alpha_{em} + \alpha_{size}$.

In this work, we build on the initial development and testing of CARAMEL-GAS and allow for a more general power-law index, α, which we now refer to as the radial power law index. In this way, the radial power law index, α, now represents both the emissivity power law index, α_{em}, and the size power law index of the BLR gas structure/clouds, α_{size}.

To determine the line emission at time t with this new generalized radial power law index,

$\alpha = \alpha_{em} + \alpha_{size}$, we go back to Equation 4.8. Rather than assume the particles all have the same size, we assume particles have an emitting size that changes with radius, r, described by a power-law function in radius, such that:

$$A_c(r) = A_{c,0}(r/r_0)^{\alpha_{size}} \tag{4.11}$$

where r represents the BLR's radial distance from the central source and $A_{c,0} = A_c(r_0)$ is a normalization constant that corresponds to the emitting size of particles at the pivot radius r_0.

We note that in the optically thick limit, all absorption and reprocessing of ionized photons will occur at the cloud's surface so that the emitting size, $A_c(r)$, corresponds to the clouds' surface area. In the optically thin limit, however, we expect the relevant emitting size, $A_c(r)$, to be better described by the cloud's volume. In the intermediate, and more realistic case, we expect the relevant emitting size, $A_c(r)$, to scale in an intermediate way between surface area and volume. Our power law described in Equation 4.11 holds true for all three scenarios described, as it provides a general description of how the BLR cloud emitting sizes change with radial distance from the ionizing source, regardless of whether the emitting size is best described by a surface area, volume, or some intermediate of the two.

We revisit Equation 4.8 and update the **size** of each individual particle, $A_{c,i}$, so that it is described by the power-law function in radial distance, $A_{c,i} = A_c(r_i) = A_{c,0}(r_i/r_0)^{\alpha_{size}}$. Equation 4.8 now becomes:

$$L_{line}(\lambda, t) = \sum_{i=0}^{N} \tilde{\epsilon}_0 \left[\frac{L_{ion}(t-\tau_i)/4\pi r_i^2}{L_{ion,0}/4\pi r_0^2} \right]^{-\alpha_{em/2}} \times A_{c,0} \left(\frac{r_i}{r_0} \right)^{\alpha_{size}} \delta(\lambda - \lambda_i) \tag{4.12}$$

where the parameter α_{em} represents the power law index for the emissivity power law function introduced in Equation 4.4, and α_{size} represents the radial power law index for the effective

size(s) of the BLR structure/clouds introduced in Equation 4.11.

Since we no longer assume the BLR particles that represent the gas density field have the same size, we define $\epsilon_0 = \tilde{\epsilon}_0 A_c(r_0) = \tilde{\epsilon}_0 A_{c,0}$ and simplify Equation 4.12. Doing so allows us to write the line emission at time t as:

$$L_{line}(\lambda, t) = \epsilon_0 \sum_{i=0}^{N} \left[\frac{L_{ion}(t - \tau_i)}{L_{ion,0}} \right]^{-\alpha_{em}/2} \left[\frac{r_i}{r_0} \right]^{\alpha_{em}+\alpha_{size}} \times \delta(\lambda - \lambda_i) \tag{4.13}$$

where again, the parameter α_{em} represents the emissivity power law index and the parameter α_{size} represents the size power law index of the BLR structure/clouds.

Assuming that the BLR responds linearly to variations in the continuum and using the additive offset, C_{add}, as well as the CARAMEL weighting factor $W(\xi, \phi_i, \kappa)$, the total emission line observed from all the model particles can be expressed as:

$$L_{line}(\lambda, t) = \epsilon_0 \sum_{i=0}^{N} \left[\frac{L_{obs}(t - \tau_i) + C_{add}}{L_{obs,0} + C_{add}} \right] \left[\frac{r_i}{r_0} \right]^{\alpha} \times W(\xi, \phi_i, \kappa) \delta(\lambda - \lambda_i) \tag{4.14}$$

Equation 4.14 is similar to Equation 4.10 where $L_{obs,0}$ is the mean V/B band continuum luminosity observed, and $L_{obs}(t - \tau_i)$ is the observed V/B continuum luminosity that arrives at a particle at time t given its distance, and associated time lag τ_i. Here, however, the radial power law index parameter, $\alpha = \alpha_{em} + \alpha_{size}$, takes a more generalized form and represents both the emissivity power law index, α_{em}, introduced in Equation 4.4, and the BLR size power law index, α_{size}, introduced in Equation 4.11.

Since we have changed the meaning of the model parameter α, we must also change the parameter's prior. For the contribution from the emissivity power law index, α_{em}, we utilize our previous uniform prior with values between -2 to 0, as we expect negative values from photoionization models (Goad et al., 2012). For the contribution from the size power law index, α_{size}, we use a uniform prior with values between 0 to 1.5 based on pressure law models

(Rees et al., 1989). Combining the contributions of both components for the generalized radial power law index, $\alpha = \alpha_{em} + \alpha_{size}$, we determine a new uniform prior for α with values between -2 to 1.5.

In summary, we have modified CARAMEL-GAS from its initial development to allow the BLR structure to have an effective emitting size that may vary with radial distance from the ionizing source. Since we are expanding both the meaning and prior of the parameter α, we have included the AGN modeled by W22 in the initial development and testing of CARAMEL-GAS, as briefly mentioned in Section 4.2 above.

4.3.5 Modeling Details

As previously mentioned, CARAMEL-LIGHT uses normalized continuum and spectral fluxes that are rescaled to units of order unity, while CARAMEL-GAS fits the absolute luminosity scale and thus requires continuum and emission line data to be in proper luminosity units.

In Table 4.2, we outline the photometric band used for the continuum light curve of each AGN and whether the data used was measured in flux density units, f_λ (10^{-15} erg cm^{-2} s^{-1} Å^{-1}) or magnitudes. For those measured in magnitudes (i.e. those from the LAMP 2008 campaign), we first convert to flux density units using a B-band zero-point flux of 632×10^{-11} erg cm^{-2} s $^{-1}$ Å^{-1} (Bessell et al., 1998). Once the continuum and Hβ light curves are both in their respective flux density units, we convert to luminosity units using the luminosity distance calculated by adopting a Planck cosmology: $H_0 = 67.8\ km\ s^{-1}\ Mpc^{-1}$, $\Omega_m = 0.308$, and $\Omega_{vac} = 0.692$ (Planck Collaboration et al., 2016). We choose to adopt this particular cosmology to remain consistent with previous CARAMEL-LIGHT work. The corresponding luminosity distances used for each AGN are found in column 4 of Table 4.2.

Table 4.2. AGN CARAMEL-GAS Modeling Properties

Campaign	Galaxy	Photometry	D_L (Mpc)	Hβ Wavelength (Å)	Intrinsic [O3] Width (Å)	R_0 (lt.-day)	T
LAMP 2008 (P14)	Arp 151	B^*	94.8	[4893.4, 5037.4]	1.562±0.071	$4.08^{(a)}$	65
	Mrk 1310	B^*	87.1	[4909, 5007]	0.0852 ± 0.071	$3.74^{(a)}$	50
	SBS 1116+583A	B^*	125.8	[4931, 5061]	1.4 ± 0.3	$2.38^{(a)}$	30
LAMP 2011 (W18)	Mrk 1511	V	153.8	[4920, 5129]	1.7±1.5	$5.44^{(b)}$	200
	Mrk 50	V	106.7	[4900, 5049]	1.7±1.5	$8.66^{(b)}$	130
	NGC 4593	V	40.1	[4840, 4958]	1.8 ±0.1	$3.52^{(c)}$	175
	Zw 229-015	V	126.0	[4890, 5048]	2.12±0.1	$5.9^{(c)}$	50
LAMP 2016 (V22)	MCG +04-22-042	V	150.7	[4945, 5115]	2.08 ± 1.5	$13.7^{(d)}$	70
	Mrk 1392	V	164.2	[4845, 5180]	2.08 ± 1.5	$27.6^{(d)}$	270
	PG 2209+184	V	325.8	[5080, 5356]	2.08 ± 1.5	$14.6^{(d)}$	70

Note. — Column 1 specifies the campaign from which data were collected and the corresponding CARAMEL-LIGHT modeling. The name of the galaxy is found in column 2 and Column 3 specifies the photometric band used for the continuum light curve. Those denoted with * were measured using magnitudes, and the rest were measured in flux density units f_λ in 10^{-15} erg cm^{-2} s^{-1} Å^{-1}. For the continuum light curves given in units of magnitude, light curves were first converted to flux density units before being converted into luminosity units (see Section 4.4). We use the luminosity distances tabulated in Column 4 to convert continuum and Hβ light curves from flux density units to luminosity units. Luminosity distances were calculated by adopting $H_0 = 67.8\ km\ s^{-1}\ Mpc^{-1}$, $\Omega_m = 0.308$, and $\Omega_{vac} = 0.692$ (Planck Collaboration et al., 2016), in order to remain consistent with previous CARAMEL-LIGHT work. Column 5 represents the wavelength range modeled (in the observed frame), which were chosen to match the window selections used in the AGN's original CARAMEL-LIGHT modeling. Column 6 is the intrinsic [O3] λ5007 line width used, also selected to match the original values used for CARAMEL-LIGHT modeling. Column 7 is the pivot radius determined by the cross-correlation time lag measurement, τ_{cent} (in the observed frame) with references as follows: (a)Bentz et al. (2009), (b)Williams & Treu (2022), (c)Williams et al. (2018), and (d) U et al. (2022). Finally, column 8 is the statistical temperature used to account for systematic uncertainty from using a simple model (see 4.3 for discussion).

In addition to testing the generalized radial power law index that represents both the BLR emissivity and the emitting size distribution of the BLR structure, $\alpha = \alpha_{em}+\alpha_{size}$, discussed above, we also want to further validate CARAMEL-GAS results by directly comparing our results to the published CARAMEL-LIGHT results. In order to provide a fair comparison, we use the same Hβ wavelength range and intrinsic [O3] λ5007 line widths that were used in the initial CARAMEL-LIGHT modeling for our selected sample of ten AGN (see columns 5 & 6 in Table 4.2). We note that the values of the intrinsic [O3] λ5007 line widths used in the initial CARAMEL-LIGHT modeling were determined by converting the FWHM of the line widths presented in Whittle (1992) in units of km s $^{-1}$ to the line dispersion in Å, assuming the Gaussian conversion of 2.35. For objects without a comparison line width by Whittle (1992), we used the median value of the objects in the corresponding campaign (e.g., LAMP 2008, LAMP 2011, LAMP 2016) and a large uncertainty corresponding to $\sim$ 215 km s $^{-1}$.

To minimize covariance, we set the pivot radius, r_0, used to calculate the total emission line observed from the model particles (see Equation 4.14) to the BLR size determined from cross-correlation measurements, as described in Section 4.3.2. We tabulate the values used for each AGN, along with the corresponding reference in Table 4.2. Finally, we include the statistical temperature used to account for systematic uncertainty for using a simple model in column 8.

4.3.6 Expected Degeneracies

In this section, we discuss some model degeneracies we expect to find in CARAMEL-GAS. First and foremost, we have added an α_{size} component to a more generalized α parameter in this work. Given this general form, the two parameters α_{em} and α_{size} are completely degenerate and cannot be distinguished by our model and data. This degeneracy was first noted by W22, who provided an example of interpreting a value of $\alpha = 0$, given a generalized radial power law index, $\alpha = \alpha_{em}+\alpha_{size}$. In such a scenario, our model cannot distinguish between two possible solutions: $(\alpha_{em}, \alpha_{size}) = (-1, 1)$ and $(\alpha_{em}, \alpha_{size}) = (0, 0)$. The first solution would

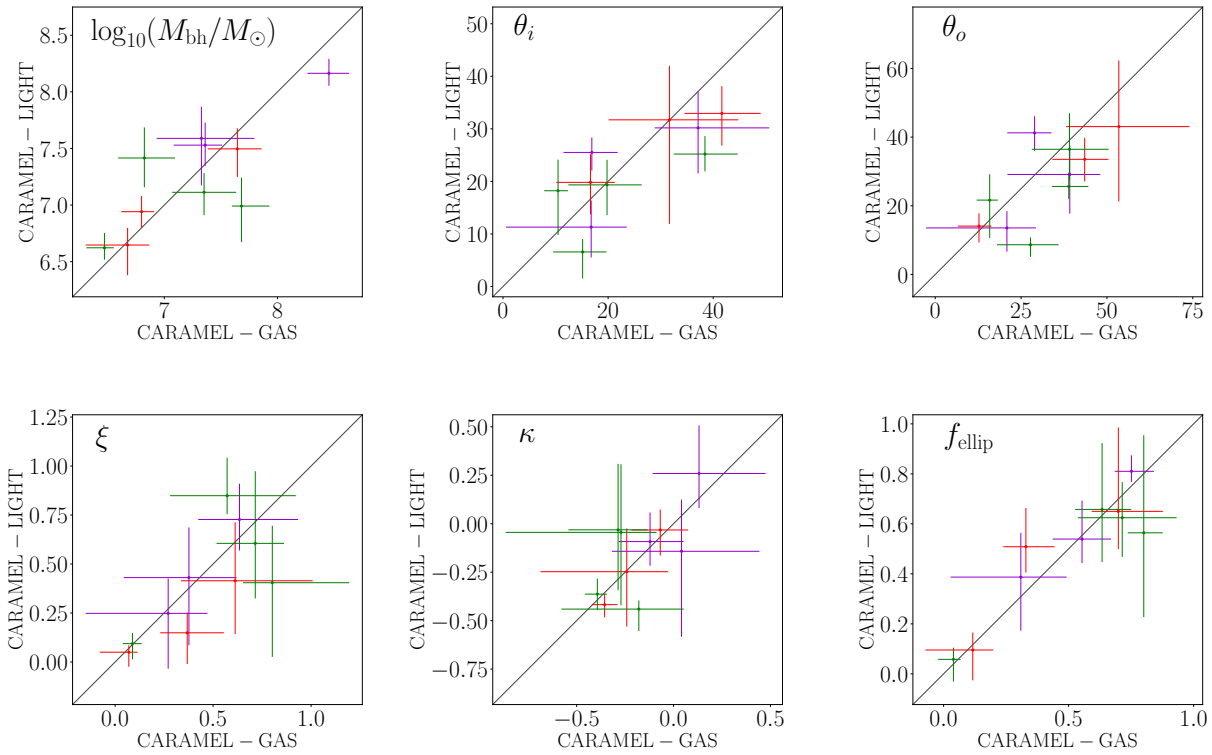

Figure 4.2 We compare the model parameters determined using both the original version of CARAMEL, CARAMEL-LIGHT, and the results found in this work using CARAMEL-GAS. We chose six of the twenty-six parameters the codes have in common to compare. On the x-axis of each plot, we depict the CARAMEL-GAS results found in this work, and on the y-axis of each plot, we show the previously published results found using CARAMEL-LIGHT. From left to right: The uppermost panel shows results for black hole mass, $\log(M_{bh}/M_{\odot})$, inclination angle, θ_i, and opening angle (disk thickness), θ_o. The lowermost panel shows: midplane transparency, ξ, the illumination factor, κ, and the fraction of particles on elliptical orbits, f_{ellip}. The colored dots and error bars show the median and 1D 68% confidence interval of the 2D posterior PDFs for each AGN. The solid black line represents an exact match in results. Purple points are for the AGN from LAMP 2016, red points are from LAMP 2011, and green points are from LAMP 2008. Overall we see that our CARAMEL-GAS and CARAMEL-LIGHT results are in good agreement.

imply: (i) emissivity decreases with increasing radial distance from the ionizing source, in agreement with photoionization models and the work of Goad et al. (2012), and (ii) increasing effective emitting size(s) of the BLR structure/clouds, with radial distance from the ionizing source. The latter, however, would imply that neither emissivity nor the effective emitting size(s) of the BLR structure/clouds, change with radial distance. In order to completely

rule out one scenario over the other, a greater level of certainty in our understanding of the physics and behavior of the BLR gas is required. We will continue this point of discussion in Section 4.4 below.

In addition to the degeneracy between the emissivity power law index, α_{em}, and the size power law index, α_{size}, we also expect a degeneracy between the parameter α and the CARAMEL-GAS parameters that describe the radial distribution of particles (μ, β) discussed in Section 4.3. Here we remind the reader that the parameter β represents the standard deviation of the shifted gamma distribution that describes the radial distribution of particles around the central black hole. Therefore, greater values of β correspond to radial profiles that drop off rapidly with radius. The parameter μ represents the mean value of the shifted gamma distribution, such that greater values of μ translate to radial profiles with larger radii.

Since CARAMEL-GAS models the gas distribution using the Hβ emission observed, the model requires information on how to map the emission to the underlying gas producing the emission, i.e. the simple power law we have chosen (see Equation 4.14). Given an emission line profile, the model can either choose to increase emission at larger radii and have a smaller radius or decrease emission at larger radii and have a larger radius, in order to match the data. For this reason, we expect there to be a degeneracy between the parameters α and μ, as well as the parameters α and β. We will continue our discussion on this expected degeneracy in Section 4.4.3.3.

4.4 Results

In this section, we validate CARAMEL-GAS by comparing our results to those found using CARAMEL-LIGHT and present our results for a more generalized radial power law index, $\alpha = \alpha_{em}+\alpha_{size}$, and possible interpretations.

4.4.1 CARAMEL-GAS Validation

In general, we do not expect CARAMEL-LIGHT and CARAMEL-GAS to produce identical values, but we do expect model parameters to be in good agreement with one another. As discussed by W22, there are some parameters that are related to the radial distribution of the gas density field that one might expect to change. With a sample of three AGN, W22 showed that these parameters indeed show a slight change, but none were deemed significant.

Here, we evaluate six model parameters: $\log(M_{bh}/M_{\odot})$, θ_i, θ_o, ξ, κ, and f_{ellip}, that are not related to the radial distribution of the gas density field (see Section 4.3 for description of model parameters). Using the model posteriors from the published CARAMEL-LIGHT results, we compare the median and 68% confidence intervals for the parameters listed above, with our CARAMEL-GAS results in Figure 4.2. Overall, we see the model parameters are in general agreement with one another and conclude the modifications to CARAMEL-GAS produces reliable results. Additionally, the agreement between model parameters also allows us to highlight that despite the simplicity of CARAMEL-LIGHT, in which absolute fluxes are not modeled, the model still results in reliable BLR geometry and kinematics, so long as the results are understood to represent the BLR emissivity field and not the underlying BLR gas density field.

Although our validation has further confirmed the results of CARAMEL-GAS, we would like to re-iterate a point made previously by W22: CARAMEL-GAS is not a replacement for CARAMEL-LIGHT. For future work, if black hole mass estimates and insights into the geometry and kinematics of the BLR emissivity **are** the primary science goals, we still recommend using CARAMEL-LIGHT, since CARAMEL-GAS is still in the early development stages and requires additional assumptions to interpret its results.

4.4.2 Radial Power Law Index

Now that we have validated the results between CARAMEL-GAS and CARAMEL-LIGHT for our sample of ten AGN, we can proceed to discuss our results for testing a generalized radial power law index, $\alpha = \alpha_{em}+\alpha_{size}$.

We present the resulting posterior distribution functions for the radial power law index, $\alpha = \alpha_{em}+\alpha_{size}$, for the ten AGN modeled in this work in Figure 4.3. For readability purposes, we display the results by grouping the AGN with their respective observation campaign, i.e. LAMP 2008, LAMP 2011, or LAMP 2016. We also tabulate these results in Table 4.3 and report the median value and 68% confidence interval. Looking at the posteriors in Figure 4.3, we find the best converged results for the LAMP 2016 campaign and note that the models for Mrk 1310 and SBS 1116+584A (LAMP 2008) were unable to constrain the α parameter.

4.4.3 Possible Interpretations

In general, we find our models prefer positive values for $\alpha = \alpha_{em}+\alpha_{size}$. As expected, with the modifications we have made to CARAMEL-GAS in this work, we are not able to distinguish between the radial emissivity power law index, α_{em}, and the radial size power law index, α_{size}, as previously discussed in Section 4.3.6. However, we can still speculate the different possible interpretations and physical scenarios in which a positive radial power law index, $\alpha = \alpha_{em}+\alpha_{size} > 0$, would be favored.

4.4.3.1 BLR Structure/Cloud Size Distribution

Based on photoionization models, we might expect BLR emissivity to decrease with radial distance from the ionizing source and thus a negative emissivity power law index, α_{em}. Under this assumption, we can deduce that a value of $\alpha_{em} \sim -1$ or $\alpha_{em} \sim -2$ is expected, and CLOUDY models suggest $\alpha_{em} \sim -1$ for Hβ slabs of gas (Goad et al., 2012).

If we assume $\alpha_{em} \sim -2$, then our CARAMEL-GAS models, which favor a positive $\alpha = \alpha_{em}+$

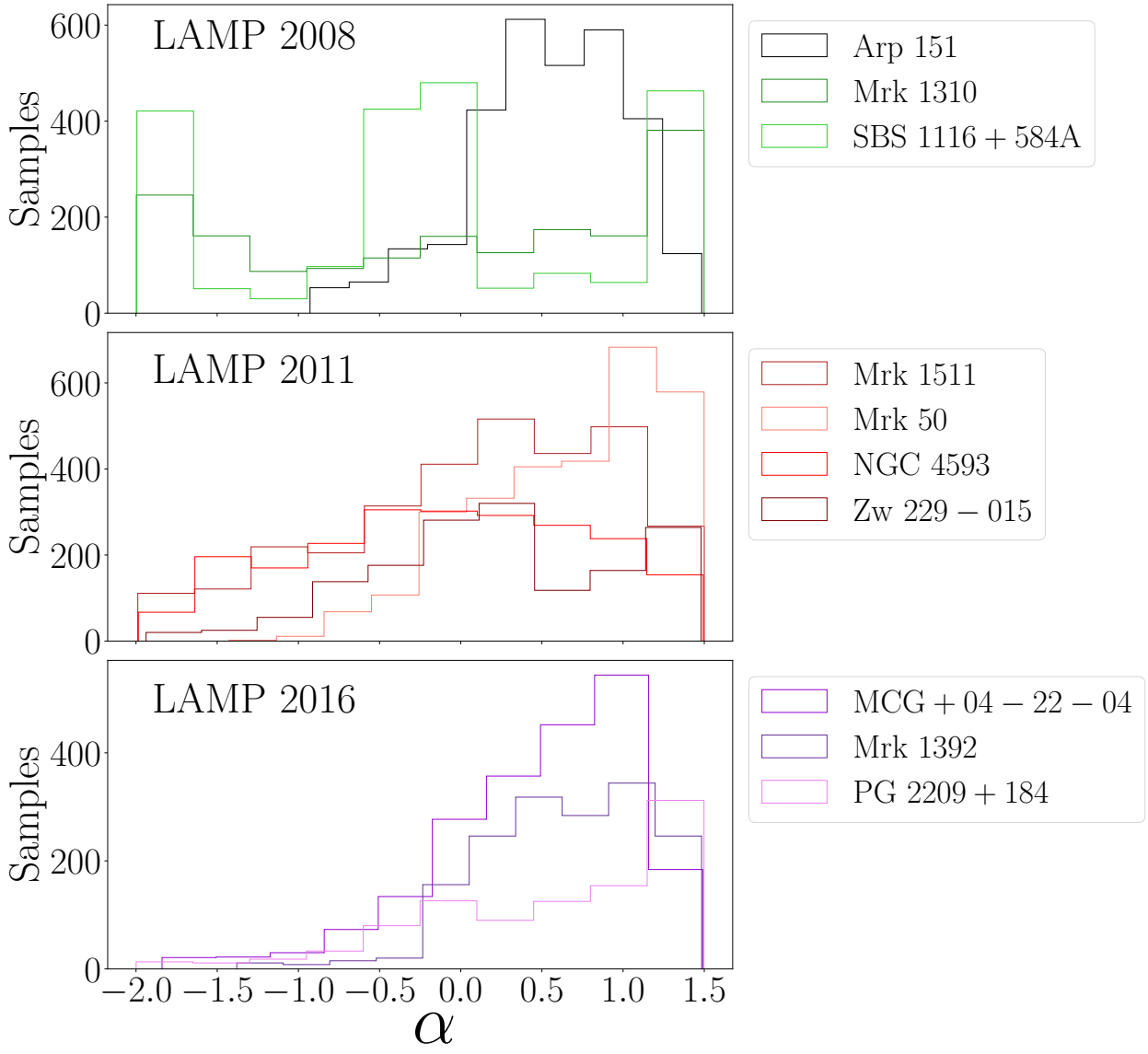

Figure 4.3 The posterior distribution functions of the generalized radial power-law index parameter, $\alpha = \alpha_{em} + \alpha_{size}$, are shown above. The results are split up by campaign. The top panel shown in green represent AGN in our sample that were observed during the LAMP 2008 campaign, the middle panel shown in red represent AGN in our sample that were observed during the LAMP 2011 campaign, and the bottom panel shown in purple represent AGN in our sample that were observed during the LAMP 2016 campaign.

Table 4.3. Radial Power Law Index, α

Campaign	Galaxy	α
LAMP 2008 (P14)	Arp 151	$0.57^{+0.46}_{-0.45}$
	Mrk 1310	$0.08^{+1.67}_{-1.19}$
	SBS 1116+583A	$-0.21^{+1.59}_{-1.44}$
LAMP 2011 (W18)	Mrk 1511	$0.21^{+1.06}_{-0.75}$
	Mrk 50	$0.81^{+0.79}_{-0.45}$
	NGC 4593	$-0.09^{+0.99}_{-0.94}$
	Zw 229-015	$0.18^{+0.73}_{-1.00}$
LAMP 2016 (V22)	MCG +04-22-042	$0.61^{+0.72}_{-0.46}$
	Mrk 1392	0.66 ± 0.54
	PG 2209+184	$0.73^{+0.99}_{-0.63}$

Note. — The best fit for the generalized radial power law index, $\alpha = \alpha_{em} + \alpha_{size}$, which represents both a radial emissivity power law index and a radial size power law index. Column 1 specifies the corresponding campaign and original published CARAMEL-LIGHT work of the AGN found in Column 2. Column 3 shows the median value of the model fit and 68% confidence interval.

$\alpha_{size} > 0$, imply $\alpha_{size} \geq 2$. In such a case, we might imagine the BLR is composed of discrete clouds that increase in effective emitting size as a function of radial distance squared and get increasingly larger the further away from the black hole. In the more likely case, as suggested by photoionization calculations, in which $\alpha_{em} \sim -1$, our models imply $\alpha_{size} \geq 1$, and the BLR clouds only slightly increase in effective emitting size with increasing radial distance, in a linear manner.

If we accept that our CARAMEL-GAS Monte Carlo representation of the gas density field implies a picture of BLR clouds with increasing emitting sizes as a function of radial distance, the question of a physical description follows. One possible description we propose is that a decrease in radiation pressure with radial distance leads to a decrease in the density of the BLR gas, and consequently an increase in size with increasing radial distance from the ionizing source, such that the emitting size(s) of the BLR structure/clouds increase with radial distance. Alternatively, we suggest tidal forces as another possible explanation. Since tidal forces will be greater at a closer proximity to the central black hole, this could lead to

fragmentation of the BLR structure/clouds closer to the inner edges of the BLR disk. This would cause the clouds at further radial distances to appear to have larger sizes since they have not experienced as much fragmentation. Finally, we propose that the clouds at smaller radial distances might be sheared by differential rotation, in which case clouds at larger radial distances that do not experience shearing appear to have greater effective emitting sizes.

4.4.3.2 BLR Emissivity Distribution

Since we cannot distinguish between α_{size} and α_{em} in our model, we cannot completely rule out the interpretation in which our results of a positive $\alpha = \alpha_{em}+\alpha_{size} > 0$ actually correspond to positive values of α_{em}. In this scenario, we assume that the Monte Carlo representation of the gas density field is not a description of discrete clouds, but rather a dynamic wind-like structure, such that $\alpha_{size} = 0$.

If $\alpha_{size} = 0$, then positive values of $\alpha = \alpha_{em}+\alpha_{size}$ imply $\alpha_{em} > 0$, such that BLR emission is concentrated at the edges, or increases with radial distance from the ionizing source. This scenario could be possible if parts of the BLR closer to the plane of the accretion disk are optically thick, perhaps due to a bowl-shape geometry, such as the one suggested by Goad et al. (2012). In this picture, the inner regions of the bowl are less reflective and emissivity thus increases at greater radial distances. Additionally, in the case of an optically thick BLR, we might expect larger covering factors closer to the ionizing source, so that greater fractions of the continuum are absorbed by the BLR, as seen from the central engine. In this scenario, the covering factor decreases with radial distance from the central source, allowing for more emission at larger radial distances. Another physical description that could lead to emission at the edges of the BLR, is self-shadowing within the BLR disk at inner radii by gas at larger radii, similar to that suggested for the accretion disk by Wang et al. (2012).

4.4.3.3 Better Theoretical Input Needed

The discussion in Sections 4.4.3.1 and 4.4.3.2 show that in order to constrain the underlying BLR gas distribution from reverberation mapping data, **our** models need a more informative picture of how BLR emission maps to gas density. Qualitatively, this is intuitive and expected. We are now in the position to quantify these degeneracies and formulate more specific requirements from theoretical models.

Returning to the expected degeneracies between the model parameters α and β, and the model parameters α and μ first discussed in Section 4.3.6, we look at the 2d posterior plots of α and β (Figure 4.4) and α and μ (Figure 4.9) for Mrk 50. The 2D posterior plots for the rest of our sample can be found in the Appendix.

As seen in the lower left corner of Figure 4.4, we see covariance between the model parameters α and β, such that positive values of α are correlated with greater values of β, and negative values of α are correlated with smaller values of β. Since increasing values of β correspond to radial profiles that drop off rapidly, the model can either choose to have rapid radial drop-offs (smaller BLR radii) that are offset by positive values of α (placing emission at the outer edges), or smaller values of β (larger BLR radii) accompanied with negative values α, so that emission decreases with radius, given the larger BLR radius.

Similarly, looking at the lower left corner of Figure 4.9, the covariance between the model parameters α and μ exists, such that positive values of α are correlated with smaller values of μ, and negative values of α are correlated with larger values of μ. Since increasing values of μ correspond to radial profiles with larger radii, the model can either choose to have a larger BLR radius that is accompanied by negative values of α, (decreased emission with radius), or smaller values of μ (smaller BLR radii) that are offset with positive values α, so that emission increases with radius, given the smaller BLR radius.

In both cases, the model is either choosing between (i) a larger BLR radius (as described

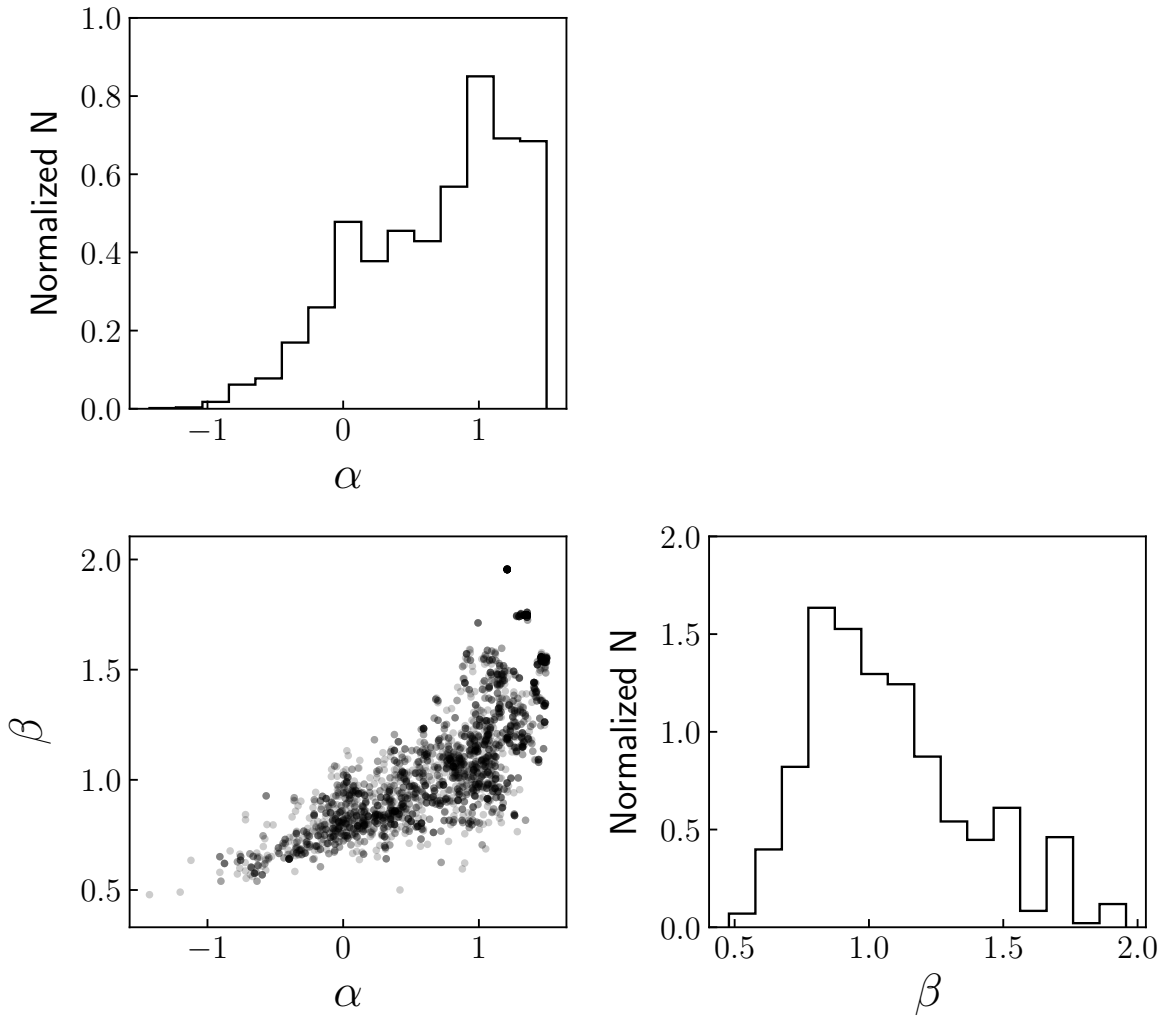

Figure 4.4 Selected posterior plots for Mrk 50 from the LAMP 2011 sample. **Bottom Left:** The 2D posterior plot between model parameters α and β, with α on the x-axis and β on the y-axis. The 2D posterior plot shows covariance between the model parameters, such that positive values of α are correlated with greater values of β, and negative values of α are correlated with smaller values of β. Since increasing values of β correspond to radial profiles that drop off rapidly, the model can either choose to have rapid radial drop offs that are offset by positive values of α, i.e. placing emission at the outer edges, or smaller values of β (i.e. larger BLR radius) accompanied with negative values of α so that emission decreases with radius, given the larger BLR radius.**Top Left:** 1D posterior plot of the parameter α. **Bottom Right:** 1D posterior plot of the parameter β.

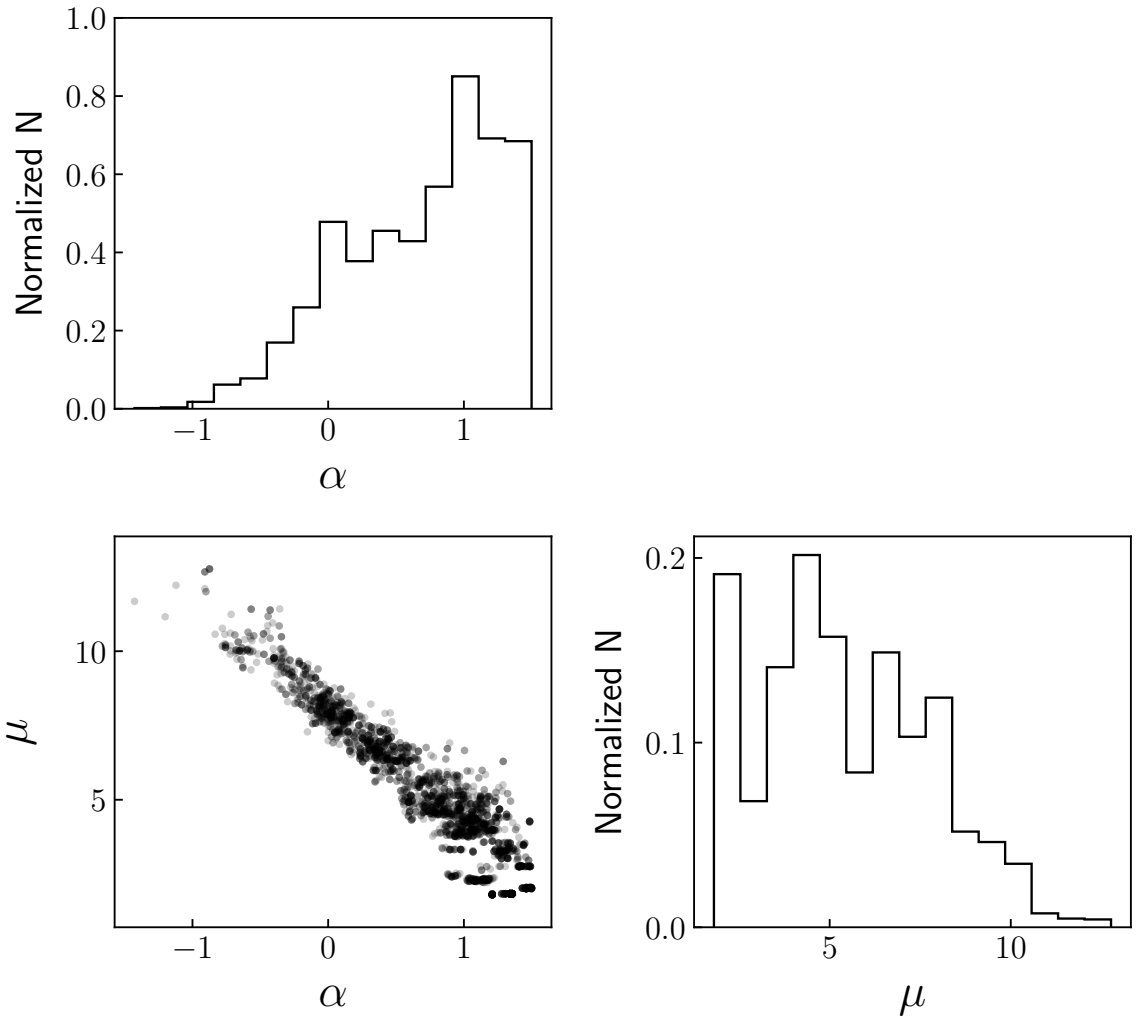

Figure 4.5 Selected posterior plots for Mrk 50 from the LAMP 2011 sample. **Bottom Left:** The 2D posterior plot between model parameters α and μ, with α on the x-axis and μ on the y-axis. The 2D posterior plot shows covariance between the model parameters, such that positive values of α are correlated with smaller values of μ, and negative values of α are correlated with larger values of μ. Since increasing values of μ correspond to radial profiles with larger radii, the model can either choose to have a larger BLR radius that is accompanied by negative values of α, i.e. decreased emission with radius, or smaller values of μ (i.e. smaller BLR radius) that are offset with positive values α so that emission increases with radius, given the smaller BLR radius.**Top Left:** 1D posterior plot of the parameter α. **Bottom Right:** 1D posterior plot of the parameter μ.

by smaller values of β or larger values of μ) with decreasing emission as a function of radius ($\alpha < 0$) or (ii) a smaller BLR radius (as described by larger values of β or smaller values of μ) with increasing emission as a function of radius ($\alpha > 0$). The latter could be due to either emission at the outer edges of the BLR structure due to geometric effects ($\alpha_{em} > 0$) or larger cloud sizes ($\alpha_{size} > 0$) as previously discussed. For this reason, we conclude that our models need more physically motivated priors before we can proceed with empirical modeling of the BLR gas distribution.

4.5 Conclusion

In this work, we expanded on the initial development of CARAMEL-GAS, which models the BLR gas density field using reverberation mapping data. The first version of the code used a simple power law to describe the emissivity of the gas, and early tests indicated models might prefer values greater than zero. Here we introduced a more general power law, $\alpha = \alpha_{em} + \alpha_{size}$, which also considers the effective emitting size(s) of the BLR structure/clouds, via α_{size}. Using a sample of ten AGN observed during three different LAMP campaigns, and previously modeled with CARAMEL-LIGHT, we tested the general power law index, $\alpha = \alpha_{em} + \alpha_{size}$, and compared our geometry and kinematic model results with those determined by CARAMEL-LIGHT.

Overall, we find CARAMEL-LIGHT and CARAMEL-GAS results are in general agreement, adding to the body of evidence supporting that black hole masses and other key parameters derived from this method are robust. We continue to recommend the use of the original version of the code, CARAMEL-LIGHT, for estimating black hole mass and studying the structure and kinematics of the BLR emissivity.

We find positive values of a generalized radial power law index ($\alpha_{em} + \alpha_{size} > 0$) are preferred, and provide the following interpretations: (i) if we assume $\alpha_{em} < 0$, then $\alpha_{size} > 0$, which implies the effective emitting size(s) of the BLR structure/clouds must increase as a function

of radial distance from the central black hole, perhaps due to increasing tidal forces or shearing from differential rotation at inner radii, or even a decrease in radiation pressure at larger radii. (ii) Alternatively, if we assume $\alpha_{size} = 0$, then $\alpha_{em} > 0$ implies emission is concentrated at the edges, perhaps due to a BLR disk that is optically thick at inner radii. In this scenario, we suggest larger cover factors closer to the ionizing source, a bowl-shaped geometry with inner regions that are less reflective, or even self-shadowing of the inner BLR disk by the outer BLR disk.

We believe empirical modeling of the BLR gas distribution requires further insight into which of these two scenarios described above is physically motivated and preferred, in order to provide CARAMEL-GAS with more informative prior knowledge.

Acknowledgements

We thank the anonymous referee for their helpful comments and suggestions, which significantly improved this manuscript. L.V. and T.T. gratefully acknowledge support from the NSF through grant AST-1907208, "Collaborative Research: Establishing the Foundations of Black Hole Mass Measurements of AGN across Cosmic Time." V.N.B gratefully acknowledges assistance from the NSF through grant AST-1909297. Note that findings and conclusions do not necessarily represent views of the NSF.

V.U acknowledges partial funding support from NASA Astrophysics Data Analysis Program (ADAP) grants #80NSSC20K0450 and #80NSSC23K0750, and STScI grants #HST-AR-17063.005-A, #HST-GO-17285.001-A, and #JWST-GO-01717.001-A.

4.6 Appendix

In the paper we discuss the expected degeneracy between the model parameters α, β, and μ, and highlight the 2D posterior plots of Mrk 50 from the LAMP 2011 sample. Here we

provide the 2D posterior plots for the rest of the AGN in our sample. We exclude Mrk 1310 and SBS 1116+583A from the LAMP 2008 sample, however, since the models were unable to constrain the α parameter.

4.6.1 Arp 151 (LAMP 2008)

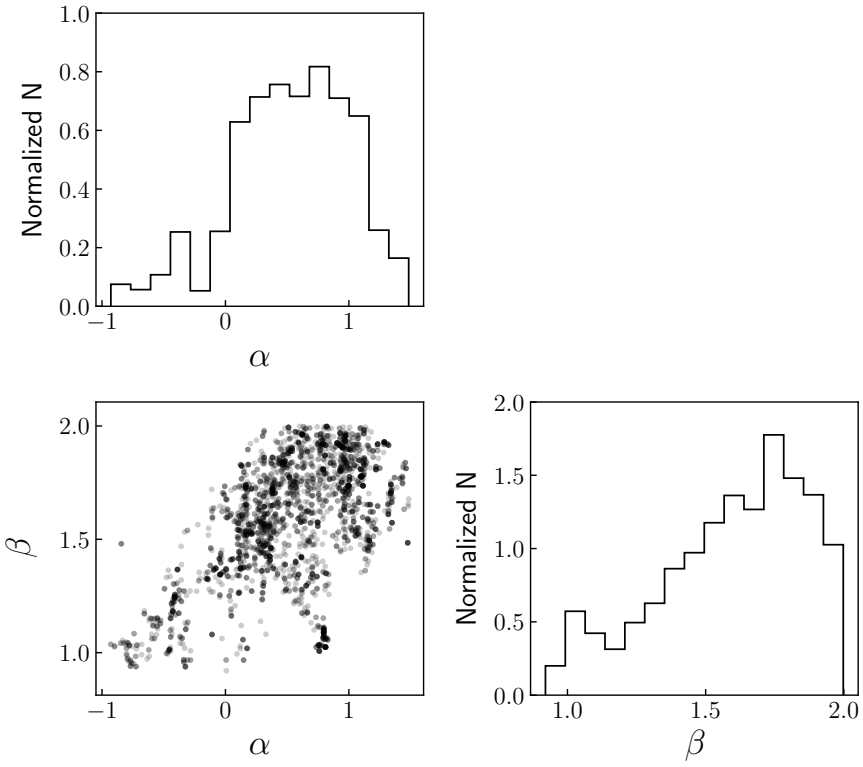

Figure 4.6 Selected posterior plots for Arp 151 from the LAMP 2008 sample. **Bottom Left:** The 2D posterior plot between model parameters α and β, with α on the x-axis and β on the y-axis. The 2D posterior plot shows covariance between the model parameters, such that positive values of α are correlated with greater values of β, and negative values of α are correlated with smaller values of β. Since increasing values of β correspond to radial profiles that drop off rapidly, the model can either choose to have rapid radial drop-offs that are offset by positive values of α, i.e. placing emission at the outer edges, or smaller values of β (i.e. larger BLR radius) accompanied with negative values of α so that emission decreases with radius, given the larger BLR radius. **Top Left:** 1D posterior plot of the parameter α. **Bottom Right:** 1D posterior plot of the parameter β.

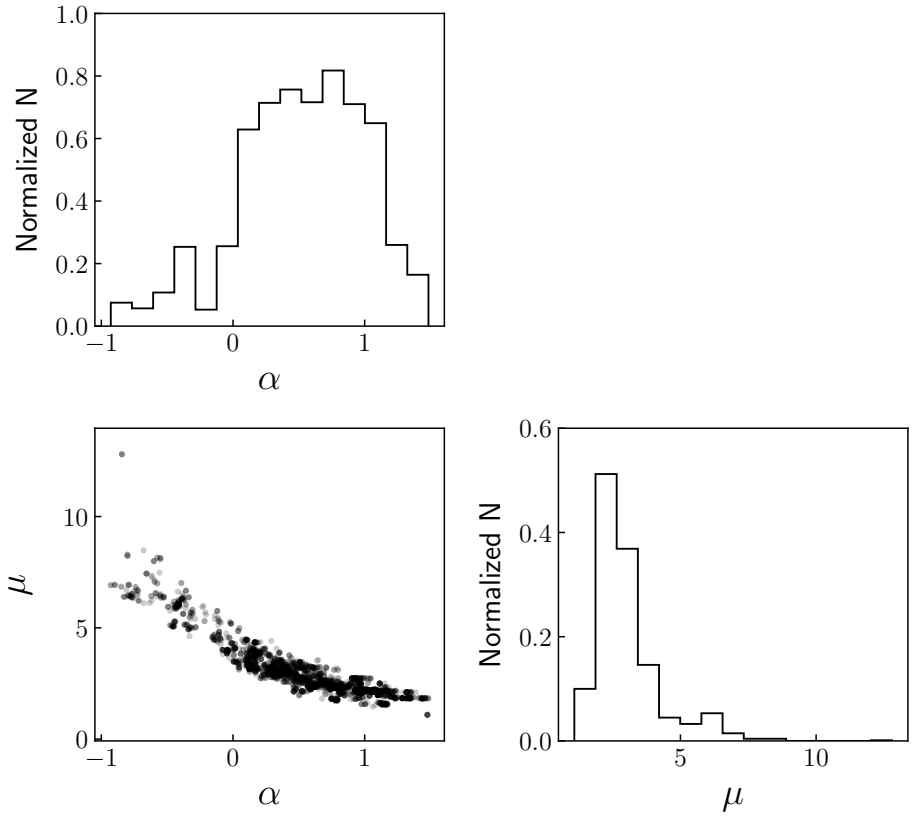

Figure 4.7 Selected posterior plots for Arp 151 from the LAMP 2008 sample. **Bottom Left:** The 2D posterior plot between model parameters α and μ, with α on the x-axis and μ on the y-axis. The 2D posterior plot shows covariance between the model parameters, such that positive values of α are correlated with smaller values of μ, and negative values of α are correlated with larger values of μ. Since increasing values of μ correspond to radial profiles with larger radii, the model can either choose to have a larger BLR radius that is accompanied by negative values of α, i.e. decreased emission with radius, or smaller values of μ (i.e. smaller BLR radius) that are offset with positive values α so that emission increases with radius, given the smaller BLR radius.**Top Left:** 1D posterior plot of the parameter α. **Bottom Right:** 1D posterior plot of the parameter μ.

4.6.2 Mrk 1511 (LAMP 2011)

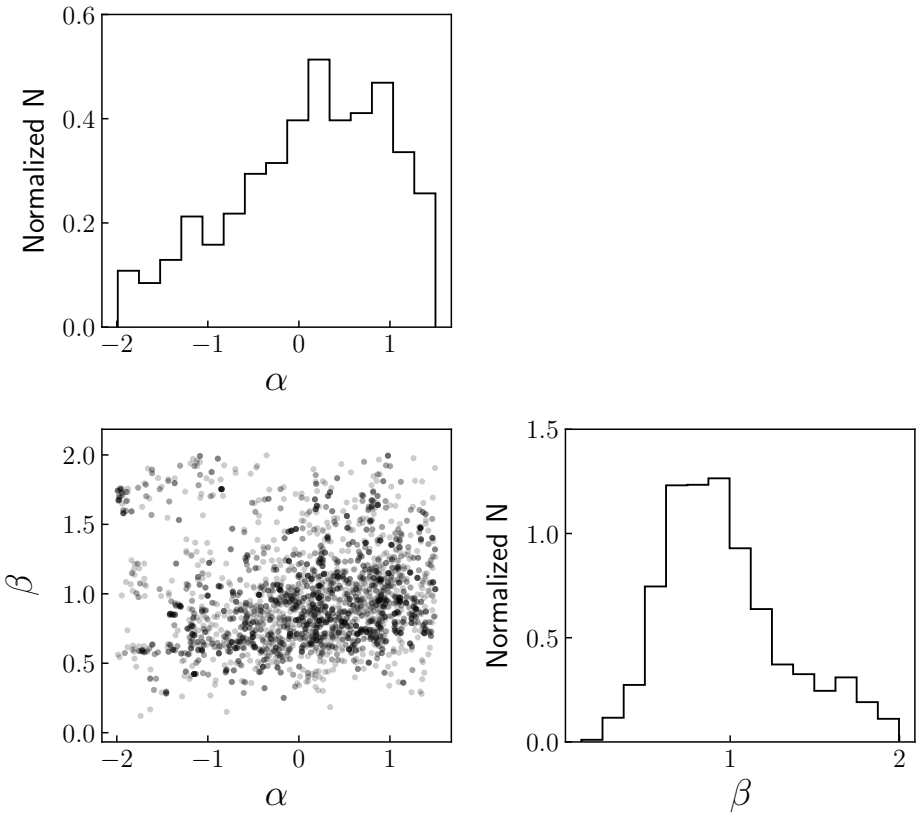

Figure 4.8 Selected posterior plots for Mrk 1511 from the LAMP 2011 sample. **Bottom Left:** The 2D posterior plot between model parameters α and β, with α on the x-axis and β on the y-axis. The 2D posterior plot shows covariance between the model parameters, such that positive values of α are correlated with greater values of β, and negative values of α are correlated with smaller values of β. Since increasing values of β correspond to radial profiles that drop off rapidly, the model can either choose to have rapid radial drop-offs that are offset by positive values of α, i.e. placing emission at the outer edges, or smaller values of β (i.e. larger BLR radius) accompanied with negative values of α so that emission decreases with radius, given the larger BLR radius. **Top Left:** 1D posterior plot of the parameter α. **Bottom Right:** 1D posterior plot of the parameter β.

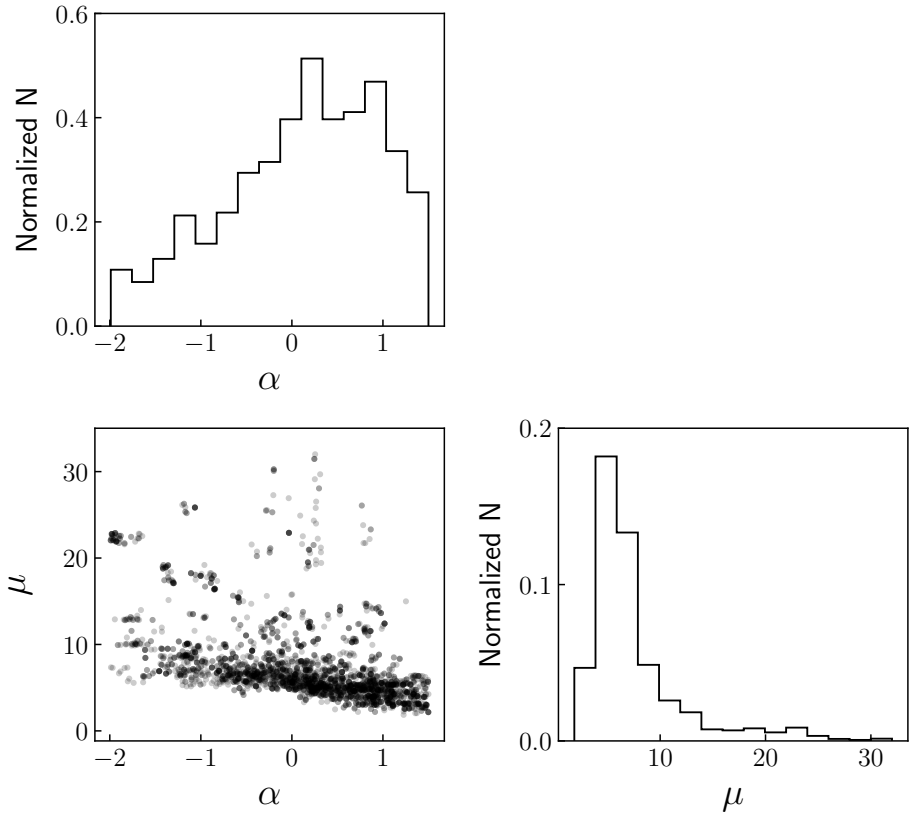

Figure 4.9 Selected posterior plots for Mrk 1511 from the LAMP 2011 sample. **Bottom Left:** The 2D posterior plot between model parameters α and μ, with α on the x-axis and μ on the y-axis. The 2D posterior plot shows covariance between the model parameters, such that positive values of α are correlated with smaller values of μ, and negative values of α are correlated with larger values of μ. Since increasing values of μ correspond to radial profiles with larger radii, the model can either choose to have a larger BLR radius that is accompanied by negative values of α, i.e. decreased emission with radius, or smaller values of μ (i.e. smaller BLR radius) that are offset with positive values α so that emission increases with radius, given the smaller BLR radius.**Top Left:** 1D posterior plot of the parameter α. **Bottom Right:** 1D posterior plot of the parameter μ.

4.6.3 NGC 4593 (LAMP 2011)

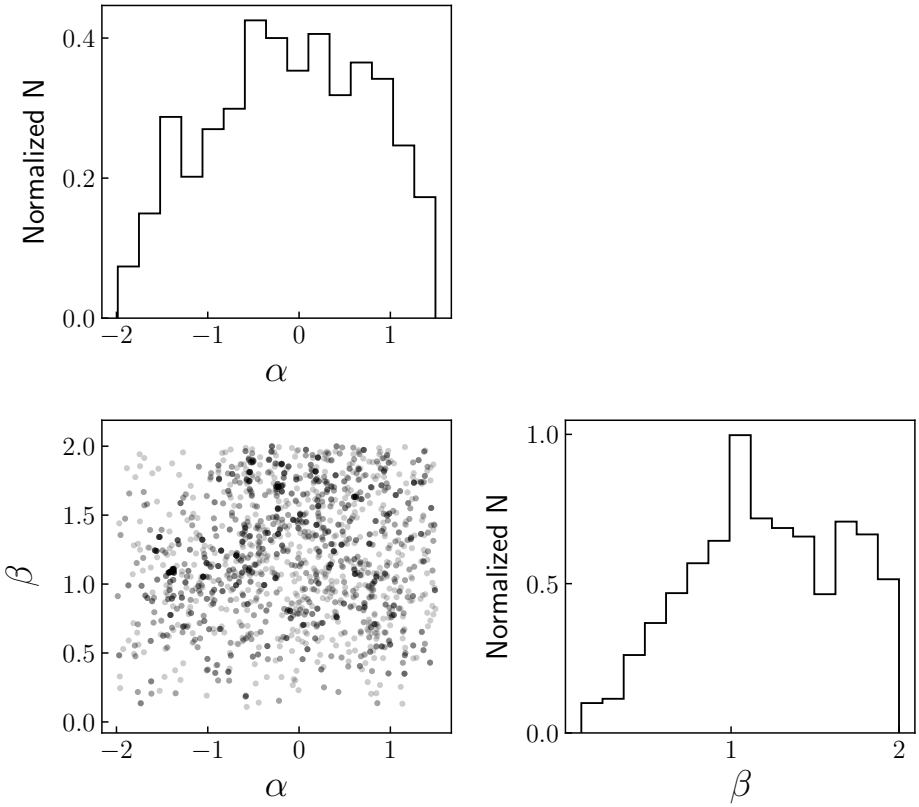

Figure 4.10 Selected posterior plots for NGC 4593 from the LAMP 2011 sample. **Bottom Left:** The 2D posterior plot between model parameters α and β, with α on the x-axis and β on the y-axis. The 2D posterior plot shows covariance between the model parameters, such that positive values of α are correlated with greater values of β, and negative values of α are correlated with smaller values of β. Since increasing values of β correspond to radial profiles that drop off rapidly, the model can either choose to have rapid radial drop-offs that are offset by positive values of α, i.e. placing emission at the outer edges, or smaller values of β (i.e. larger BLR radius) accompanied with negative values of α so that emission decreases with radius, given the larger BLR radius. **Top Left:** 1D posterior plot of the parameter α. **Bottom Right:** 1D posterior plot of the parameter β.

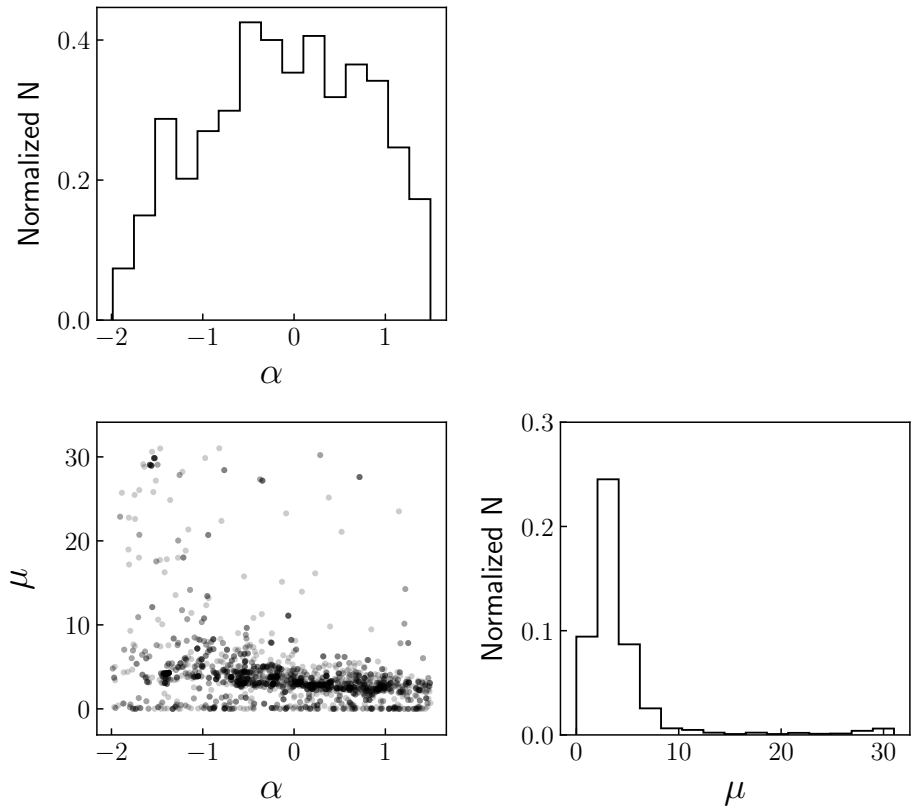

Figure 4.11 Selected posterior plots for NGC 4593 from the LAMP 2011 sample. **Bottom Left:** The 2D posterior plot between model parameters α and μ, with α on the x-axis and μ on the y-axis. The 2D posterior plot shows covariance between the model parameters, such that positive values of α are correlated with smaller values of μ, and negative values of α are correlated with larger values of μ. Since increasing values of μ correspond to radial profiles with larger radii, the model can either choose to have a larger BLR radius that is accompanied by negative values of α, i.e. decreased emission with radius, or smaller values of μ (i.e. smaller BLR radius) that are offset with positive values α so that emission increases with radius, given the smaller BLR radius.**Top Left:** 1D posterior plot of the parameter α. **Bottom Right:** 1D posterior plot of the parameter μ.

4.6.4 Zw 229-015 (LAMP 2011)

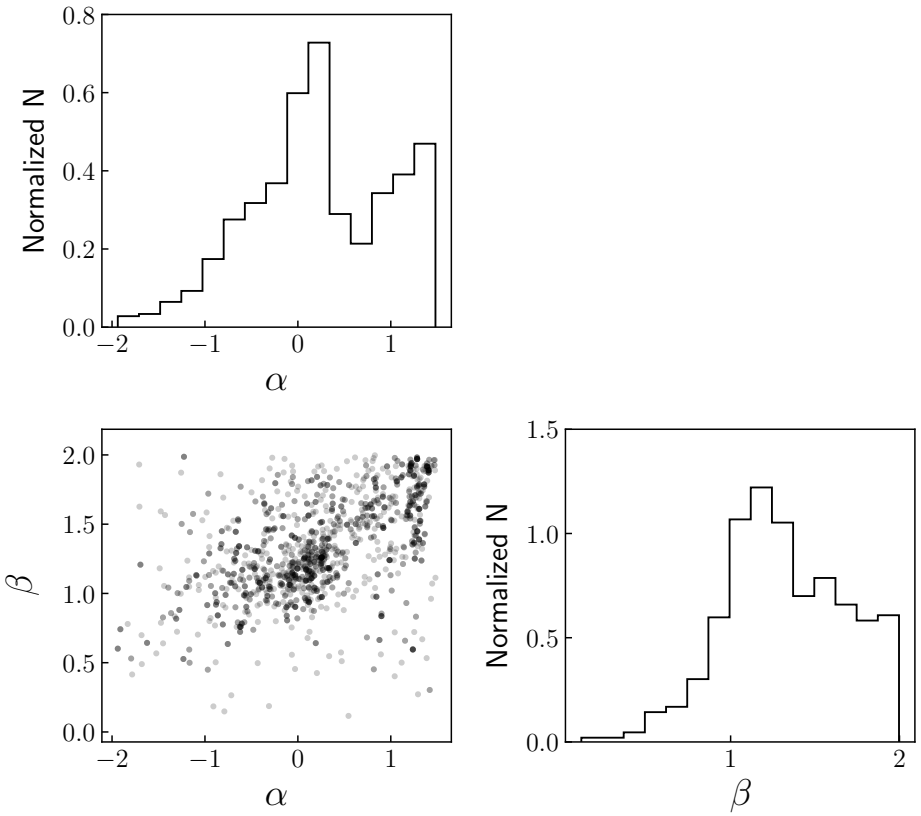

Figure 4.12 Selected posterior plots for Zw 229-015 from the LAMP 2011 sample. **Bottom Left:** The 2D posterior plot between model parameters α and β, with α on the x-axis and β on the y-axis. The 2D posterior plot shows covariance between the model parameters, such that positive values of α are correlated with greater values of β, and negative values of α are correlated with smaller values of β. Since increasing values of β correspond to radial profiles that drop off rapidly, the model can either choose to have rapid radial drop-offs that are offset by positive values of α, i.e. placing emission at the outer edges, or smaller values of β (i.e. larger BLR radius) accompanied with negative values of α so that emission decreases with radius, given the larger BLR radius. **Top Left:** 1D posterior plot of the parameter α. **Bottom Right:** 1D posterior plot of the parameter β.

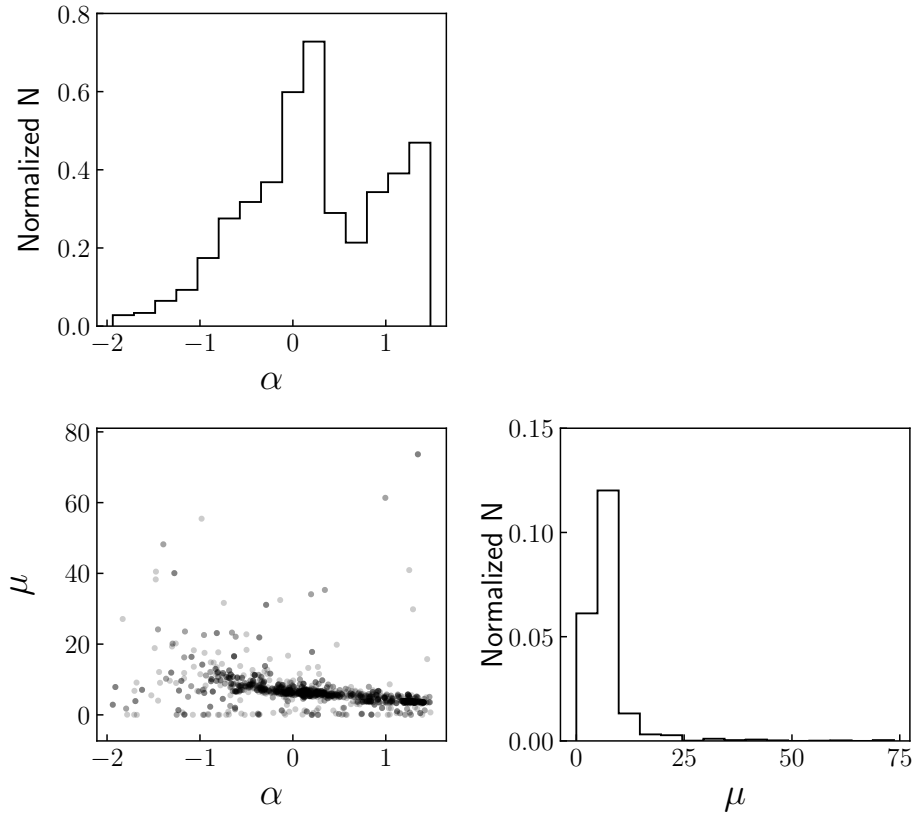

Figure 4.13 Selected posterior plots for Zw 229-015 from the LAMP 2011 sample. **Bottom Left:** The 2D posterior plot between model parameters α and μ, with α on the x-axis and μ on the y-axis. The 2D posterior plot shows covariance between the model parameters, such that positive values of α are correlated with smaller values of μ, and negative values of α are correlated with larger values of μ. Since increasing values of μ correspond to radial profiles with larger radii, the model can either choose to have a larger BLR radius that is accompanied by negative values of α, i.e. decreased emission with radius, or smaller values of μ (i.e. smaller BLR radius) that are offset with positive values α so that emission increases with radius, given the smaller BLR radius.**Top Left:** 1D posterior plot of the parameter α. **Bottom Right:** 1D posterior plot of the parameter μ.

4.6.5 MCG +04-22-042 (LAMP 2016)

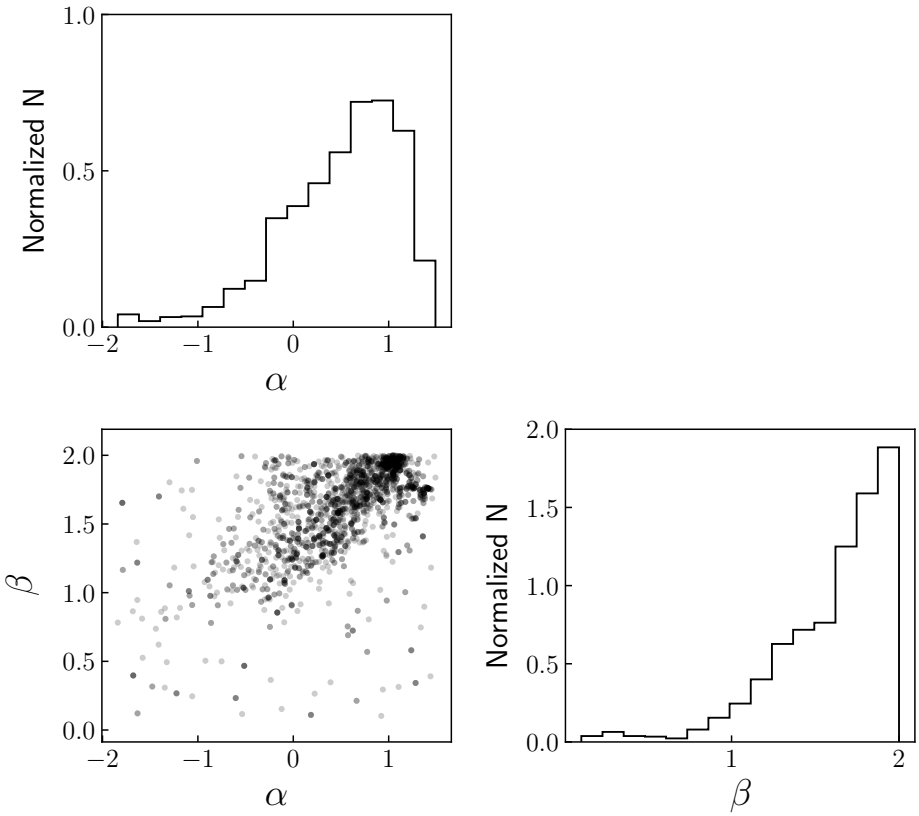

Figure 4.14 Selected posterior plots for MCG +04-22-042 from the LAMP 2016 sample. **Bottom Left:** The 2D posterior plot between model parameters α and β, with α on the x-axis and β on the y-axis. The 2D posterior plot shows covariance between the model parameters, such that positive values of α are correlated with greater values of β, and negative values of α are correlated with smaller values of β. Since increasing values of β correspond to radial profiles that drop off rapidly, the model can either choose to have rapid radial drop-offs that are offset by positive values of α, i.e. placing emission at the outer edges, or smaller values of β (i.e. larger BLR radius) accompanied with negative values of α so that emission decreases with radius, given the larger BLR radius. **Top Left:** 1D posterior plot of the parameter α. **Bottom Right:** 1D posterior plot of the parameter β.

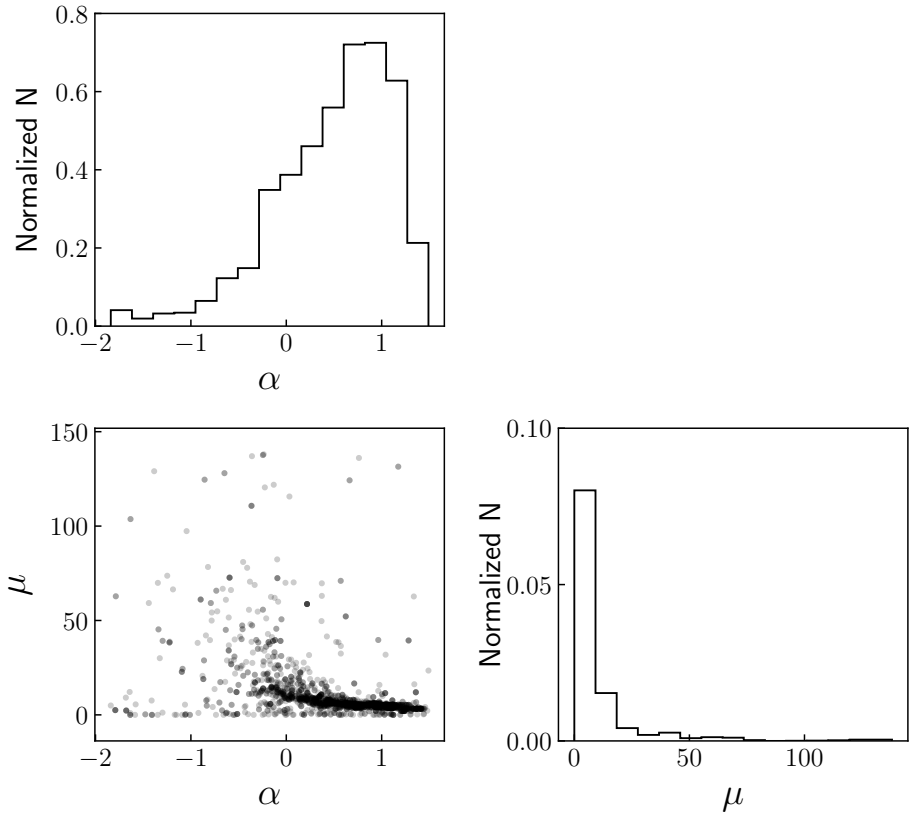

Figure 4.15 Selected posterior plots for MCG +04-22-042 from the LAMP 2016 sample. **Bottom Left:** The 2D posterior plot between model parameters α and μ, with α on the x-axis and μ on the y-axis. The 2D posterior plot shows covariance between the model parameters, such that positive values of α are correlated with smaller values of μ, and negative values of α are correlated with larger values of μ. Since increasing values of μ correspond to radial profiles with larger radii, the model can either choose to have a larger BLR radius that is accompanied by negative values of α, i.e. decreased emission with radius, or smaller values of μ (i.e. smaller BLR radius) that are offset with positive values α so that emission increases with radius, given the smaller BLR radius.**Top Left:** 1D posterior plot of the parameter α. **Bottom Right:** 1D posterior plot of the parameter μ.

4.6.6 Mrk 1392 (LAMP 2016)

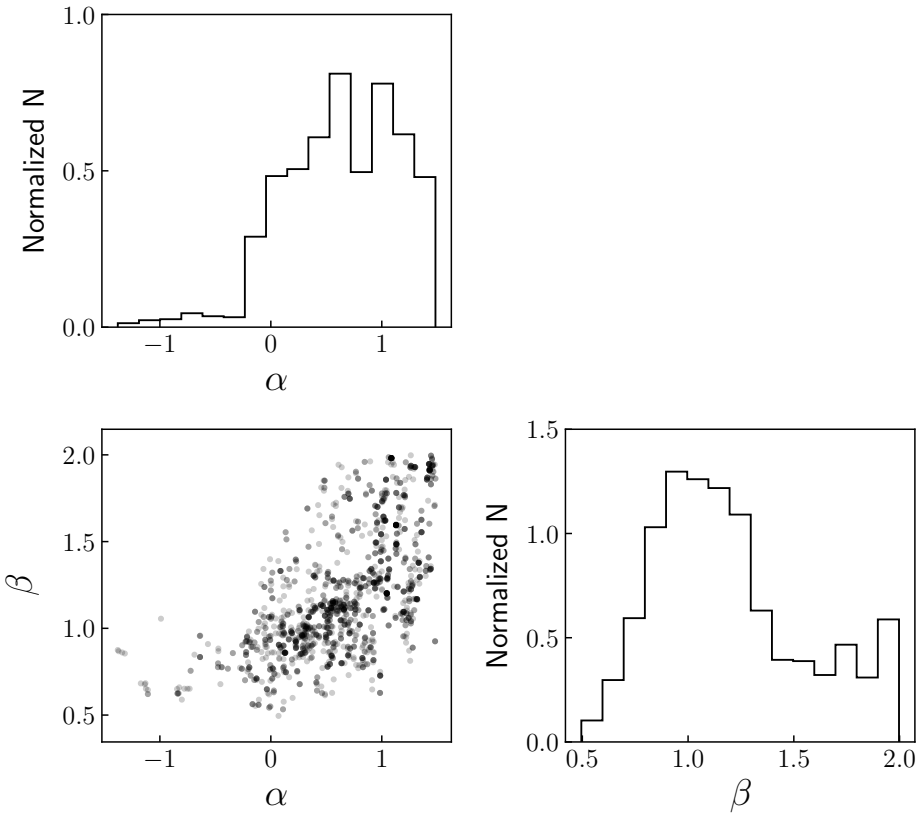

Figure 4.16 Selected posterior plots for Mrk 1392 from the LAMP 2016 sample. **Bottom Left:** The 2D posterior plot between model parameters α and β, with α on the x-axis and β on the y-axis. The 2D posterior plot shows covariance between the model parameters, such that positive values of α are correlated with greater values of β, and negative values of α are correlated with smaller values of β. Since increasing values of β correspond to radial profiles that drop off rapidly, the model can either choose to have rapid radial drop-offs that are offset by positive values of α, i.e. placing emission at the outer edges, or smaller values of β (i.e. larger BLR radius) accompanied with negative values of α so that emission decreases with radius, given the larger BLR radius. **Top Left:** 1D posterior plot of the parameter α. **Bottom Right:** 1D posterior plot of the parameter β.

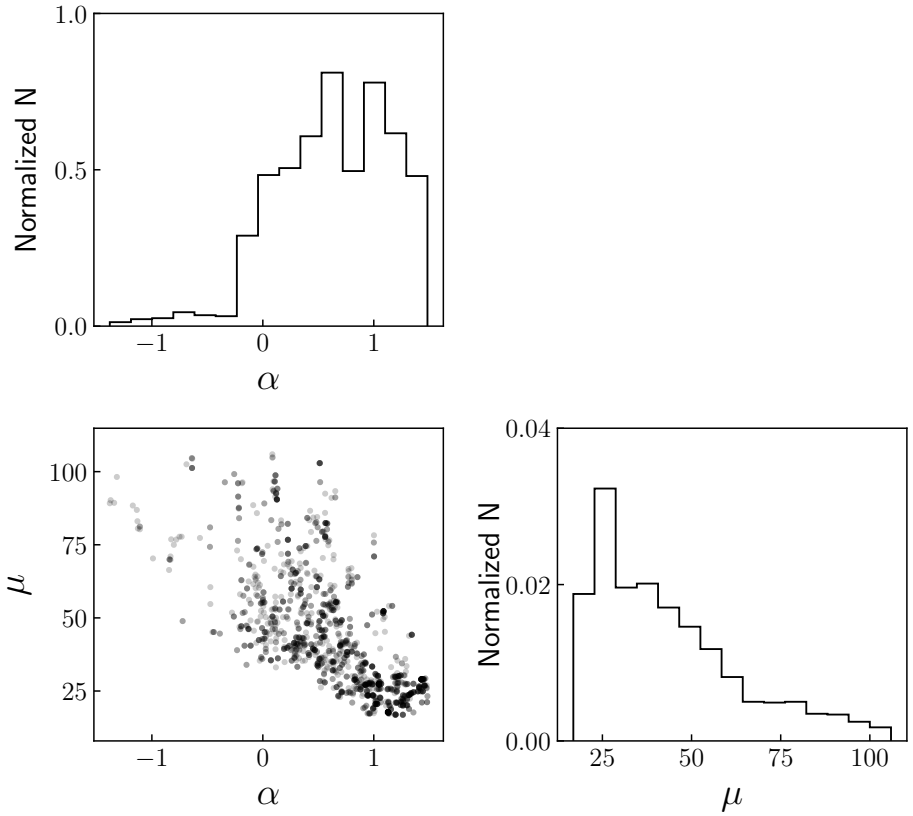

Figure 4.17 Selected posterior plots for Mrk 1392 from the LAMP 2016 sample. **Bottom Left:** The 2D posterior plot between model parameters α and μ, with α on the x-axis and μ on the y-axis. The 2D posterior plot shows covariance between the model parameters, such that positive values of α are correlated with smaller values of μ, and negative values of α are correlated with larger values of μ. Since increasing values of μ correspond to radial profiles with larger radii, the model can either choose to have a larger BLR radius that is accompanied by negative values of α, i.e. decreased emission with radius, or smaller values of μ (i.e. smaller BLR radius) that are offset with positive values α so that emission increases with radius, given the smaller BLR radius.**Top Left:** 1D posterior plot of the parameter α. **Bottom Right:** 1D posterior plot of the parameter μ.

4.6.7 PG 2209+184 (LAMP 2016)

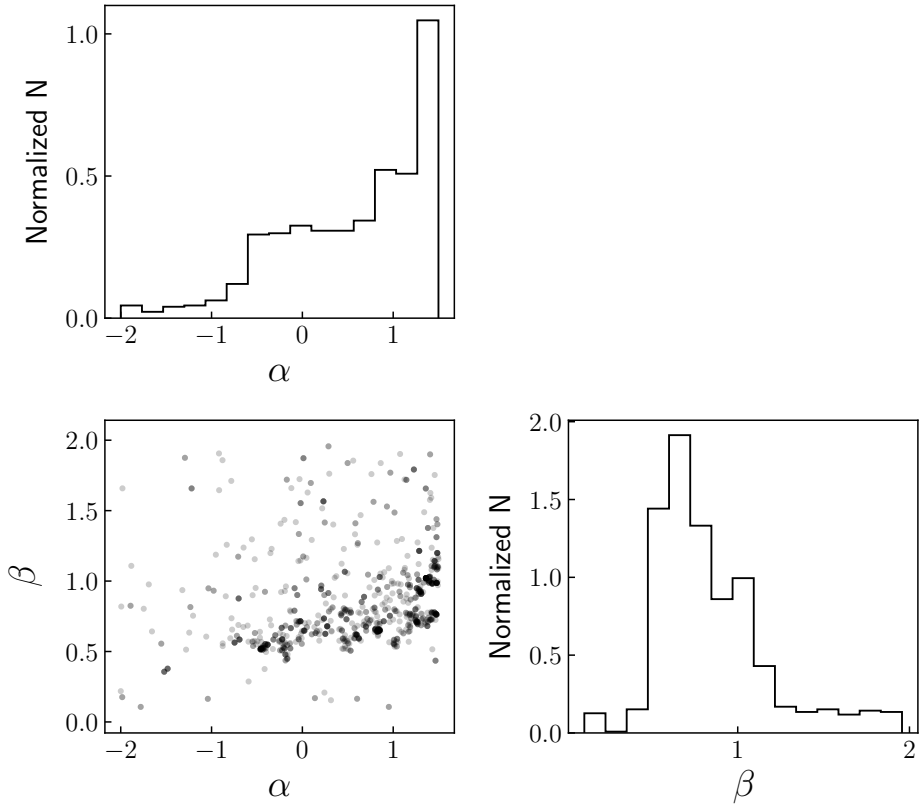

Figure 4.18 Selected posterior plots for PG 2209+184 from the LAMP 2016 sample. **Bottom Left:** The 2D posterior plot between model parameters α and β, with α on the x-axis and β on the y-axis. The 2D posterior plot shows covariance between the model parameters, such that positive values of α are correlated with greater values of β, and negative values of α are correlated with smaller values of β. Since increasing values of β correspond to radial profiles that drop off rapidly, the model can either choose to have rapid radial drop-offs that are offset by positive values of α, i.e. placing emission at the outer edges, or smaller values of β (i.e. larger BLR radius) accompanied with negative values of α so that emission decreases with radius, given the larger BLR radius. **Top Left:** 1D posterior plot of the parameter α. **Bottom Right:** 1D posterior plot of the parameter β.

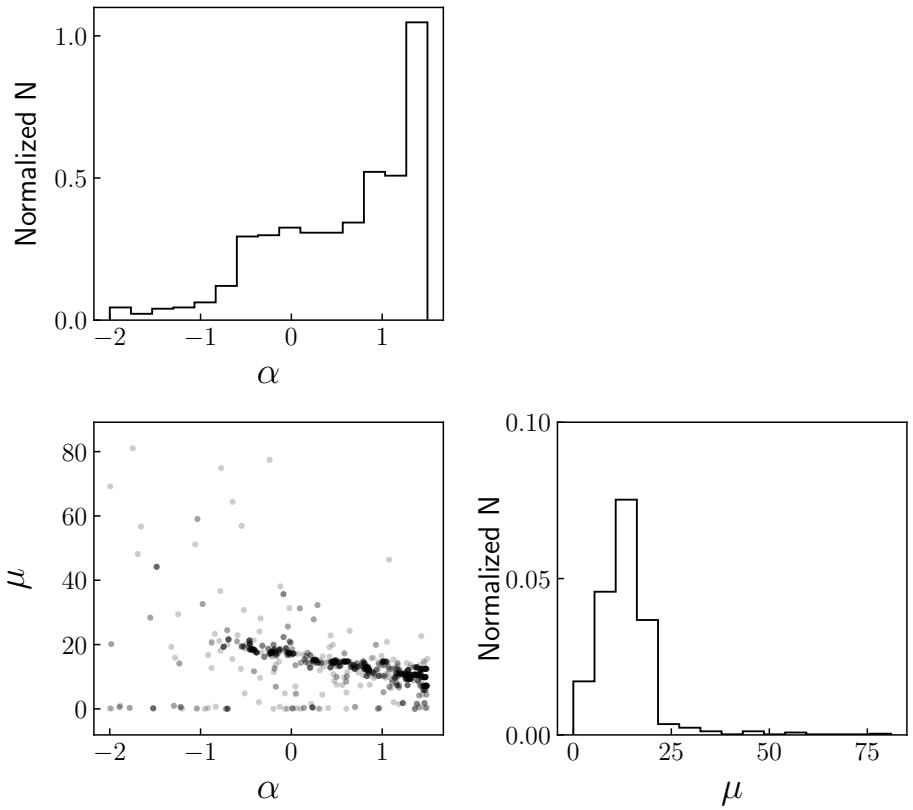

Figure 4.19 Selected posterior plots for PG 2209+184 from the LAMP 2016 sample. **Bottom Left:** The 2D posterior plot between model parameters α and μ, with α on the x-axis and μ on the y-axis. The 2D posterior plot shows covariance between the model parameters, such that positive values of α are correlated with smaller values of μ, and negative values of α are correlated with larger values of μ. Since increasing values of μ correspond to radial profiles with larger radii, the model can either choose to have a larger BLR radius that is accompanied by negative values of α, i.e. decreased emission with radius, or smaller values of μ (i.e. smaller BLR radius) that are offset with positive values α so that emission increases with radius, given the smaller BLR radius.**Top Left:** 1D posterior plot of the parameter α. **Bottom Right:** 1D posterior plot of the parameter μ.

CHAPTER 5

Conclusions

In this dissertation, I characterized the structure and kinematics of the Hβ broad emission line region (BLR) to better understand the central regions of Active Galactic Nuclei (AGN) and searched for a way to improve how black hole (BH) mass measurements are calibrated across cosmic time.

In Chapter 2, I applied forward modeling techniques to a sample of nine AGNs from the Lick AGN Monoriting Project (LAMP) 2016 reverberation mapping campaign to constrain the geometry and dynamics of the Hβ-emitting BLR. I increased the number of dynamically modeled sources by nearly 50% and combined my results with previous studies (Pancoast et al., 2014; Grier et al., 2017; Williams et al., 2018, 2020; Bentz et al., 2021) to investigate the existence of any trends in BLR structure and kinematics. Overall, I found the Hβ-emitting BLR of the LAMP 2016 sources to be best described by a thick disk observed at low to moderate inclination angles. Additionally, I did not find any luminosity-dependent trends in the Hβ-emitting BLR geometry and kinematics, suggesting AGNs have diverse BLR structures and kinematics, consistent with transient AGN/BLR conditions over timescales of order months to years. However, it is important to note that the sample is still small and may not represent the AGN population as a whole.

In Chapter 3, I used the direct modeling results of a sample of 28 AGNs — nine from LAMP 2016 (Villafaña et al., 2022, presented in Chapter 2), seven from LAMP 2011 (Williams et al., 2018), four from AGN10 (Grier et al., 2017), five from LAMP 2008 (Pancoast et al., 2014), one

from AGNSTORM (Williams et al., 2020), one from Bentz et al. (2021), and one from Bentz et al. (2022). I used the CARAMEL M_{BH} measurements to determine individual scale factors, f, for each source and searched for existing correlations between the scale factor and other AGN/BLR parameters and observables. I discovered marginal evidence for a correlation between the scale factor, f, and line-profile shape (FWHM/σ). This correlation may provide an observational proxy for the virial coefficient, f, in the future. However, further CARAMEL studies and a larger sample are needed to confirm the statistical significance of the correlation.

Finally, I expanded on the initial development of CARAMEL-GAS, which strives to use reverberation mapping data to model the BLR gas density field. The first version of the CARAMEL-GAS code used a simple power law to describe the emissivity of the gas, and early tests indicated that models might prefer values greater than zero (Williams & Treu, 2022). In Chapter 4, I introduced a more general power law, $\alpha = \alpha_{em} + \alpha_{size}$, which also considers the effective emitting size(s) of the BLR structure/clouds via α_{size}. Using a sample of ten AGN observed during three different LAMP campaigns and previously modeled with CARAMEL, I tested the general power law index, $\alpha = \alpha_{em} + \alpha_{size}$. I found that positive values of a generalized radial power law index ($\alpha_{em} + \alpha_{size} > 0$) were preferred. If we assume $\alpha_{em} < 0$, then $\alpha_{size} > 0$, which implies the effective emitting size(s) of the BLR structure/clouds must increase as a function of radial distance from the central black hole, perhaps due to increasing tidal forces or shearing from differential rotation at inner radii, or even a decrease in radiation pressure at larger radii. Alternatively, if we assume $\alpha_{size} = 0$, then $\alpha_{em} > 0$ implies emission is concentrated at the edges, perhaps due to an optically thick BLR disk at inner radii. This scenario could be caused by larger covering factors closer to the ionizing source, a bowl-shaped geometry with inner regions that are less reflective, or even self-shadowing of the inner BLR disk by the outer BLR disk.

Ultimately, stronger theoretical assumptions are needed to break the degeneracies inherent to the interpretation of reverberation mapping data in terms of underlying gas properties and to

provide further insight into which of the two scenarios described above is physically motivated and preferred. Thus, the path forward for the testing and development of CARAMEL-GAS is contingent on theoretical progress in the field of BLR astrophysics research.

However, the path forward for Chapters 2 and 3 is straightforward and requires building a larger sample of AGN with dynamical BLR modeling. A larger sample will allow me to continue to investigate both (i) whether BLR geometry and kinematics are diverse (consistent with transient conditions) and (ii) the correlation I have found between the virial coefficient, f, and the Hβ line profile shape, (FWHM/σ). Continuing my efforts to characterize the structure and kinematics of the BLR may help us better understand the central regions of AGNs and their role in galaxy evolution (e.g., gas transport and heating/cooling). The latter can potentially improve how black hole masses are calibrated across cosmic time, which is most relevant for studies of the evolution of the BH scaling relations and galaxy evolution studies in the era of JWST.

Bibliography

Agudo, I., Gómez, J. L., Casadio, C., Cawthorne, T. V., & Roca-Sogorb, M. 2012, , 752, 92

Agudo, I., Gómez, J. L., Casadio, C., Cawthorne, T. V., & Roca-Sogorb, M. 2012, The Astrophysical Journal, 752, 92

Aird, J., Coil, A. L., Georgakakis, A., et al. 2015, Monthly Notices of the Royal Astronomical Society, 451, 1892

Antonucci, R. 1993, , 31, 473

Baldwin, J., Ferland, G., Korista, K., & Verner, D. 1995, , 455, L119

Barth, A. J., Nguyen, M. L., Malkan, M. A., et al. 2011a, , 732, 121

Barth, A. J., Pancoast, A., Thorman, S. J., et al. 2011b, , 743, L4

Barth, A. J., Bennert, V. N., Canalizo, G., et al. 2015a, , 217, 26

—. 2015b, , 217, 26

Batiste, M., Bentz, M. C., Raimundo, S. I., Vestergaard, M., & Onken, C. A. 2017, , 838, L10

Bennert, V. N., Treu, T., Woo, J.-H., et al. 2010, , 708, 1507

Bentz, M. C., & Katz, S. 2015a, , 127, 67

—. 2015b, , 127, 67

Bentz, M. C., Markham, M., Rosborough, S., et al. 2023a, , 959, 25

Bentz, M. C., Onken, C. A., Street, R., & Valluri, M. 2023b, , 944, 29

Bentz, M. C., Street, R., Onken, C. A., & Valluri, M. 2021, , 906, 50

Bentz, M. C., Williams, P. R., Street, R., et al. 2021, A Detailed View of the Broad Line Region in NGC 3783 from Velocity-Resolved Reverberation Mapping, arXiv:2108.00482 [astro-ph.GA]

Bentz, M. C., Williams, P. R., & Treu, T. 2022, , 934, 168

Bentz, M. C., Denney, K. D., Cackett, E. M., et al. 2006, , 651, 775

Bentz, M. C., Walsh, J. L., Barth, A. J., et al. 2009, , 705, 199

Bessell, M. S., Castelli, F., & Plez, B. 1998, , 333, 231

Blandford, R. D., & McKee, C. F. 1982, , 255, 419

Booth, C. M., & Schaye, J. 2009, , 398, 53

Boroson, T., Brown, T., Hjelstrom, A., et al. 2014, in Society of Photo-Optical Instrumentation Engineers (SPIE) Conference Series, Vol. 9149, Observatory Operations: Strategies, Processes, and Systems V, ed. A. B. Peck, C. R. Benn, & R. L. Seaman, 91491E

Boyle, B., & Terlevich, R. J. 1998, Monthly Notices of the Royal Astronomical Society, 293, L49

Brewer, B. J., & Foreman-Mackey, D. 2018, Journal of Statistical Software, 86, 1–33

Brewer, B. J., Treu, T., Pancoast, A., et al. 2011, , 733, L33

Brown, T. M., Baliber, N., Bianco, F. B., et al. 2013, , 125, 1031

Cackett, E. M., Bentz, M. C., & Kara, E. 2021, iScience, 24, 102557

Cackett, E. M., & Horne, K. 2006, , 365, 1180

Cattaneo, A., Faber, S. M., Binney, J., et al. 2009, Nature, 460, 213–219

Collin, S., Kawaguchi, T., Peterson, B. M., & Vestergaard, M. 2006a, , 456, 75

—. 2006b, , 456, 75

Croton, D. J. 2006, Monthly Notices of the Royal Astronomical Society, 369, 1808–1812

De Rosa, G., Peterson, B. M., Ely, J., et al. 2015, , 806, 128

De Rosa, G., Fausnaugh, M. M., Grier, C. J., et al. 2018, , 866, 133

Denney, K. D., Peterson, B. M., Pogge, R. W., et al. 2009, , 704, L80

—. 2010, , 721, 715

Ding, X., Silverman, J., Treu, T., et al. 2020a, The Astrophysical Journal, 888, 37

—. 2020b, The Astrophysical Journal, 888, 37

Du, P., Hu, C., Lu, K.-X., et al. 2015, , 806, 22

Du, P., Lu, K.-X., Hu, C., et al. 2016, , 820, 27

Du, P., Brotherton, M. S., Wang, K., et al. 2018, , 869, 142

Dubois, Y., Peirani, S., Pichon, C., et al. 2016, , 463, 3948

Elvis, M., Marengo, M., & Karovska, M. 2002, , 567, L107

Emmering, R. T., Blandford, R. D., & Shlosman, I. 1992, , 385, 460

Fabian, A. C. 2012, , 50, 455

Feng, H.-C., Liu, H. T., Bai, J. M., et al. 2021, , 912, 92

Ferland, G. J., Korista, K. T., Verner, D. A., et al. 1998, , 110, 761

Ferrarese, L., & Ford, H. 2005, , 116, 523

Ferrarese, L., & Merritt, D. 2000a, , 539, L9

—. 2000b, , 539, L9

Filippenko, A. V., Li, W. D., Treffers, R. R., & Modjaz, M. 2001, in Astronomical Society of the Pacific Conference Series, Vol. 246, IAU Colloq. 183: Small Telescope Astronomy on Global Scales, ed. B. Paczynski, W.-P. Chen, & C. Lemme, 121

Gebhardt, K., Bender, R., Bower, G., et al. 2000a, , 539, L13

—. 2000b, , 539, L13

Goad, M. R., Korista, K. T., & Ruff, A. J. 2012, , 426, 3086

Graham, A. W., Onken, C. A., Athanassoula, E., & Combes, F. 2011, , 412, 2211

Gravity Collaboration, Sturm, E., Dexter, J., et al. 2018, , 563, 657

Gravity Collaboration, Amorim, A., Bauböck, M., et al. 2020, , 643, A154

—. 2021, , 648, A117

Grier, C. J., Pancoast, A., Barth, A. J., et al. 2017, , 849, 146

Grier, C. J., Peterson, B. M., Pogge, R. W., et al. 2012, , 755, 60

Grier, C. J., Martini, P., Watson, L. C., et al. 2013, , 773, 90

Hirschmann, M., Khochfar, S., Burkert, A., et al. 2010, Monthly Notices of the Royal Astronomical Society, 407, 1016–1032

Horne, K. 1994, in Astronomical Society of the Pacific Conference Series, Vol. 69, Reverberation Mapping of the Broad-Line Region in Active Galactic Nuclei, ed. P. M. Gondhalekar, K. Horne, & B. M. Peterson, 23

Horne, K., Peterson, B. M., Collier, S. J., & Netzer, H. 2004, , 116, 465

Jahnke, K., & Macciò, A. V. 2011, , 734, 92

Jahnke, K., Bongiorno, A., Brusa, M., et al. 2009, , 706, L215

Jorstad, S. G., Marscher, A. P., Lister, M. L., et al. 2005, , 130, 1418

Kara, E., Mehdipour, M., Kriss, G. A., et al. 2021, , 922, 151

Kartje, J. F., & Königl, A. 1996, Vistas in Astronomy, 40, 133

Kaspi, S., Smith, P. S., Netzer, H., et al. 2000, , 533, 631

Kelly, B. C. 2007, , 665, 1489

Kishimoto, M., Hönig, S. F., Antonucci, R., et al. 2011, , 536, A78

Kollatschny, W., & Zetzl, M. 2011, Baltic Astronomy, 20, 400

—. 2013, , 549, A100

Konigl, A., & Kartje, J. F. 1994, , 434, 446

Kormendy, J., & Ho, L. C. 2013a, , 51, 511

—. 2013b, , 51, 511

Kormendy, J., & Richstone, D. 1995, , 33, 581

Koshida, S. 2015, in TORUS2015: The AGN Unification Scheme After 30 Years, ed. P. Gandhi & S. F. Hoenig

Krolik, J. H. 1988, , 325, 148

Li, S.-S., Yang, S., Yang, Z.-X., et al. 2021, , 920, 9

Li, Y.-R., Wang, J.-M., Ho, L. C., Du, P., & Bai, J.-M. 2013, , 779, 110

Madau, P., & Dickinson, M. 2014, Annual Review of Astronomy and Astrophysics, 52, 415

Magorrian, J., Tremaine, S., Richstone, D., et al. 1998, , 115, 2285

Maiolino, R., Risaliti, G., Salvati, M., et al. 2010, , 517, A47

Maiolino, R., Scholtz, J., Curtis-Lake, E., et al. 2023, JADES. The diverse population of infant Black Holes at 4<z<11: merging, tiny, poor, but mighty, arXiv:2308.01230 [astro-ph.GA]

Mangham, S. W., Knigge, C., Matthews, J. H., et al. 2017, Monthly Notices of the Royal Astronomical Society, 471, 4788

Marconi, A., & Hunt, L. K. 2003, , 589, L21

Mezcua, M., Pacucci, F., Suh, H., Siudek, M., & Natarajan, P. 2024, arXiv e-prints, arXiv:2404.05793

Mo, H., van den Bosch, F. C., & White, S. 2010, Galaxy Formation and Evolution

Murray, N., Chiang, J., Grossman, S. A., & Voit, G. M. 1995, , 451, 498

Netzer, H. 2015, , 53, 365

Onken, C. A., Ferrarese, L., Merritt, D., et al. 2004, , 615, 645

Pacucci, F., & Loeb, A. 2024, , 964, 154

Pancoast, A., Brewer, B. J., & Treu, T. 2011, , 730, 139

Pancoast, A., Brewer, B. J., Treu, T., et al. 2014, , 445, 3073

Pancoast, A., Barth, A. J., Horne, K., et al. 2018, , 856, 108

Park, D., Kelly, B. C., Woo, J.-H., & Treu, T. 2012a, , 203, 6

Park, D., Woo, J.-H., Bennert, V. N., et al. 2015, The Astrophysical Journal, 799, 164

Park, D., Woo, J.-H., Treu, T., et al. 2012b, , 747, 30

Pei, L., Fausnaugh, M. M., Barth, A. J., et al. 2017a, , 837, 131

—. 2017b, , 837, 131

Peng, C. Y. 2007, , 671, 1098

Peng, C. Y., Impey, C. D., Ho, L. C., Barton, E. J., & Rix, H.-W. 2006a, , 640, 114

Peng, C. Y., Impey, C. D., Rix, H.-W., et al. 2006b, , 649, 616

Peterson, B. M. 1993, , 105, 247

—. 2006, in Physics of Active Galactic Nuclei at all Scales, ed. D. Alloin, Vol. 693, 77

Peterson, B. M., Ferrarese, L., Gilbert, K. M., et al. 2004, , 613, 682

Peterson, B. M., Denney, K. D., De Rosa, G., et al. 2013, , 779, 109

Planck Collaboration, Ade, P. A. R., Aghanim, N., et al. 2016, , 594, A13

Pringle, J. E. 1981, , 19, 137

Raimundo, S. I., Vestergaard, M., Goad, M. R., et al. 2020, , 493, 1227

Rees, M. J., Netzer, H., & Ferland, G. J. 1989, , 347, 640

Robinson, A. 1995, , 272, 647

Rosborough, S., Robinson, A., & Almeyda, T. 2023, in American Astronomical Society Meeting Abstracts, Vol. 55, American Astronomical Society Meeting Abstracts, 137.02D

Salviander, S., Shields, G. A., Gebhardt, K., & Bonning, E. W. 2007, The Astrophysical Journal, 662, 131

Schawinski, K. 2012, Black Hole – Galaxy Co-evolution, arXiv:1206.2661 [astro-ph.CO]

Schulze, A., & Wisotzki, L. 2011, , 535, A87

Scoville, N., & Norman, C. 1988, , 332, 163

Sexton, R. O., Canalizo, G., Hiner, K. D., et al. 2019, The Astrophysical Journal, 878, 101

Shen, Y. 2013, Bulletin of the Astronomical Society of India, 41, 61

Shields, G. A., & Salviander, S. 2009, in Astronomical Society of the Pacific Conference Series, Vol. 419, Galaxy Evolution: Emerging Insights and Future Challenges, ed. S. Jogee, I. Marinova, L. Hao, & G. A. Blanc, 392

Silk, J., Di Cintio, A., & Dvorkin, I. 2014, in Proceedings of the International School of Physics 'Enrico Fermi' Course 186 'New Horizons for Observational Cosmology' Vol. 186, Vol. 186, 137

Silk, J., & Rees, M. J. 1998, , 331, L1

Silverman, J. D., Treu, T., Ding, X., et al. 2019, The Astrophysical Journal Letters, 887, L5

Skielboe, A., Pancoast, A., Treu, T., et al. 2015, , 454, 144

Somerville, R. S., & Davé, R. 2015, , 53, 51

Steele, I. A., Smith, R. J., Rees, P. C., et al. 2004, in Society of Photo-Optical Instrumentation Engineers (SPIE) Conference Series, Vol. 5489, Ground-based Telescopes, ed. J. Oschmann, Jacobus M., 679

Targett, T. A., Dunlop, J. S., & McLure, R. J. 2012, Monthly Notices of the Royal Astronomical Society, 420, 3621

Treu, T., Malkan, M. A., & Blandford, R. D. 2004, , 615, L97

U, V., Barth, A. J., Vogler, H. A., et al. 2022, The Lick AGN Monitoring Project 2016: Velocity-resolved Hβ Lags in Luminous Seyfert Galaxies

Urry, C. M. 2003, in American Astronomical Society Meeting Abstracts, Vol. 202, American Astronomical Society Meeting Abstracts #202, 22.01

Urry, C. M., & Padovani, P. 1995, , 107, 803

Villafaña, L., Williams, P. R., Treu, T., et al. 2023, , 948, 95

Villafaña, L., Williams, P. R., Treu, T., et al. 2022, The Astrophysical Journal, 930, 52

Walsh, J. L., Minezaki, T., Bentz, M. C., et al. 2009, , 185, 156

Wang, Y., Ferland, G. J., Hu, C., Wang, J.-M., & Du, P. 2012, , 424, 2255

Waters, T., Kashi, A., Proga, D., et al. 2016, The Astrophysical Journal, 827, 53

Waters, T., & Li, H. 2019, arXiv e-prints, arXiv:1912.03382

Whittle, M. 1992, , 79, 49

Williams, P. R., & Treu, T. 2022, , 935, 128

Williams, P. R., Pancoast, A., Treu, T., et al. 2018, , 866, 75

—. 2020, , 902, 74

Woo, J.-H., Schulze, A., Park, D., et al. 2013, , 772, 49

Woo, J.-H., Treu, T., Malkan, M. A., & Blandford, R. D. 2006, , 645, 900

—. 2008, , 681, 925

Woo, J.-H., Yoon, Y., Park, S., Park, D., & Kim, S. C. 2015, , 801, 38

Woo, J.-H., Treu, T., Barth, A. J., et al. 2010, , 716, 269